

Development of Microfluidic Devices with the Use of Nanotechnology to Aid in the Analysis of Biological
Systems Including Membrane Protein Separation, Single Cell Analysis and Genetic Markers

Thesis by
Mark David Goldberg

In Partial Fulfillment of the Requirements for the degree
of
Doctorate of Biology



CALIFORNIA INSTITUTE OF TECHNOLOGY

Pasadena, California

2015

May 27 2015

© 2015
Mark David Goldberg
All Rights Reserved

ACKNOWLEDGEMENTS

Finishing this degree is the fulfillment of a dream, I have wanted to become a doctor I just never realized how difficult the journey to that goal could be. I would not be where I am today if it was not for the kindness of my adviser Axel Scherer, he saw something in me that I did not see, and it was through him that I was given this great opportunity. Axel opened the door to getting a PhD but it was my friends and family that pushed me through it. I want to thank my parents with whom I would not be here today, and I want to give a special thank you to Aditya Rajagopal, Chieh-Feng Chang, Juan Pablo Cardenas, and Xiomara Madero. It was through your continued support, encouragement, and friendship that I was able to finish the process. I know I would have not lasted without any of you and I will forever be grateful for a dream was realized because of your help. I also would be remised if I did not thank the California Institute of Technology, I have learned more here than I could ever imagine. Not only have I become a better scientist while attending, I become more of a complex thinking individual. Who is to say if this is good or bad, thinking of the Robert Frost line “and that has made all the difference,” I can say that this journey was not easy, but it will make all the difference.

ABSTRACT

Computation technology has dramatically changed the world around us; you can hardly find an area where cell phones have not saturated the market, yet there is a significant lack of breakthroughs in the development to integrate the computer with biological environments. This is largely the result of the incompatibility of the materials used in both environments; biological environments and experiments tend to need aqueous environments. To help aid in these development chemists, engineers, physicists and biologists have begun to develop microfluidics to help bridge this divide. Unfortunately, the microfluidic devices required large external support equipment to run the device. This thesis presents a series of several microfluidic methods that can help integrate engineering and biology by exploiting nanotechnology to help push the field of microfluidics back to its intended purpose, small integrated biological and electrical devices. I demonstrate this goal by developing different methods and devices to (1) separate membrane bound proteins with the use of microfluidics, (2) use optical technology to make fiber optic cables into protein sensors, (3) generate new fluidic devices using semiconductor material to manipulate single cells, and (4) develop a new genetic microfluidic based diagnostic assay that works with current PCR methodology to provide faster and cheaper results. All of these methods and systems can be used as components to build a self-contained biomedical device.

TABLE OF CONTENTS

Acknowledgements.....	iii
Abstract	iv
Table of Contents	v
List of Illustrations and/or Tables.....	vi
Nomenclature	xii
Chapter I: Introduction.....	1
Chapter II: A Microfluidic-Base Method for Recovering Enhanced Enzymatic Activity of Membrane Bound Proteins	15
Chapter III: A Microfluidic Approach to Generate a Biomarker Monitoring Device	35
Chapter IV: Generation of Microchannels in Silicon on Insulator Wafers	58
Chapter V: Eletrofluidics	79
Chapter VI: Persistence Length Quantitative Polymerase Chain Reactions Using Quenchiplexing and FRETplexing	95
Chapter VII: Summary	139
Bibliography.....	140

LIST OF FIGURES AND/OR TABLES

<i>Figures</i>	<i>Page</i>
1.1 Self-contained Microfluidic Device	2
1.2 Lab on a Chip	3
1. 1.3 Common Glass Microfluidic Device	5
2. 1.4 High Resolution Printer Transparency	6
3. 1.5 Spincoaters	7
4. 1.6 Mask-aligner	8
5. 1.7 Multilayer fabrication diagram expressing how valves can be generated	
6. in microfluidic devices	8
7. 1.8 UV Exposure of Photoresist	9
8. 1.9 Microfluidic Droplets from an Ink-Jet Printer	10
9. 1.10 PDMS Structure	12
10. 1.11 PDMS Microfluidic Device	12
11. 2.1 Schematic Presentation of the Membrane Isolation Preparation Process.	17
12. 2.2 Microfluidic Chip Preparation	18
13. 2.3 Microfluidic Design and Fabricated Device	19
14. 2.4 Conceptual Function of the Microfluidic Device.	25
15. 2.5 Magnetic Beads in the Reaction Chamber	25
16. 2.6 Laminar Flow out of the Reaction Chamber.	26
17. 2.7 Laminar Flow Diagrams.	28
18. 2.8 Reaction Time Vs Flow Rate.	30
19. 2.9 Activity of the Peroxidase Enzyme.	31
20. 2.10 Activity of Alkaline Phosphatase	32
21. 3.1 Multimode Fiber Interferometer for the BMD Sensor	39
22. 3.2 Design of a BMD Sensor	41
23. 3.3 Optical Field in the Multimode Waveguide	42
24. 3.4 Fiber Preparation	43
25. 3.5 Fluorescent Images of Fluorescein-Labeled Biotin Coated Fibers.	45
26. 3.6a A microfluidic Template	46
27. 3.6b PDMS Mold Fabrication.	47
3.7 Optical Loss of Biotin	49
3.8 Successive Regeneration of Biotin on a Avidin Coated Fiber Optic	
28. Cable	50
3.9 Biomarker Monitoring Device Prototype	53
29. 3.10 BMD Sensory Data.	54
30. 3.11 BMD Sensory Data of Biomarkers Spiked into Whole Porcine Blood.	56
31. 4.1 Outline of the SOI channel fabrication process.	60
32. 4.2 Procedural Outline for SOI fabrication	63
33. 4.3 First Attempts at Generating Channels Inside an SOI Device.	63
34. 4.4 SEM Image of HF Generated Channel and Oxide Between the two	
35. Channels.	64
36. 4.5 SEM Image of Channels Inside SOI Device.	65

37.	4.6 Closer SEM of First Generation SOI Channels.	66
38.	4.7 System for SOI Parameter Optimization	67
39.	4.8 E-beam Writing of Optimization Patterns.	68
40.	4.9 Test Array for E-Beam Optimization	69
41.	4.10 1000 uC/cm ² Dose at 300 Magnification	70
42.	4.11 HF Etch Time and Distance Etched in SOI Wafer.	72
43.	4.12 Diffusion Etch Inside and SOI Device.	73
44.	4.13 Optimized SOI channel	73
45.	4.14 Internal Channel Access Port.	74
46.	4.15 SEM Image of the Inside an SOI Channel	75
47.	4.16 SEM Image of SOI Channel Height	76
48.	4.17 Bowing of Silicon Layer.	77
49.	5.1 Copper Electrodes	82
50.	5.2 Copper Electrode Test System	83
51.	5.3 Closer Image of Copper Device	84
5.4 Chromium Electrodes Patterned with Direct-Write Laser		
System Heidelberg Instruments DWL-66.		86
5.5 Chromium Etched Electrodes		87
5.6 Close-up Image of Chromium Etched Electrodes.		87
5.7 Two Different Views of PDMS Covered Glass Slides		88
5.8 Close-up Image of Glass Slide Cove Port.		88
5.9 Beading Flowing Through an SOI Channel		89
52.	5.10 SOI Wafer Sorting Device	89
53.	5.11 Beads Congregating Between Electrodes	90
5.12 Complex Sample of Different Size Labeled Beads.		91
54.	5.13 Dielectrophoresis Force Equation	91
55.	5.14 Separation of Cells by Size	92
56.	6.1 Iconic PCR graph	97
57.	6.2 Quenchiplexing PCR Procedure.	101
58.	6.3 Example of Quenchiplexing PCR Result.	103
59.	6.4 Example of FRETplexing PCR Result.	104
60.	6.5 Initial PCR Machine Readout for the STI Test Experiment.	109
61.	6.6 Quenchiplexing KRAS 216T at 1x Concentration.	113
62.	6.7 Quenchiplexing K-Ras 216T at 2x Concentration	114
63.	6.8 Quenchiplexing K-Ras 216T at 4x Concentration	114
64.	6.9 Quenchiplexing KRAS 216T at 1x, 2x, and 4x Concentration.	115
65.	6.10 Quenchiplexing KRAS 216A at 1x, 2x, 4x, and 8x Concentration.	116
66.	6.11 Quenchiplexing KRAS 216C at 1x, 2x, 4x, and 8x Concentration.	116
67.	6.12 Improved Quenchiplexing Assay for 216C at 1x Concentration	118
68.	6.13 Improved Quenchiplexing Assay for 216T at 2x Concentration.	119
69.	6.14 Improved Quenchiplexing Assay for 216A at 4x Concentration.	119
70.	6.15 Improved Quenchiplexing Assay for 216C at 1x and 216T at 2x	
71.	Concentration.	122
72.	6.16 Improved Quenchiplexing Assay for 216C at 1x and 216A at 4x	

73. Concentration.	123
74. 6.17 Improved Quenchiplexing Assay for 216T at 2x and 216A at 4x	
75. Concentration.	123
76. 6.18 Improved Quenchiplexing Assay for 216C at 1x, 216T at 2x, and	
77. 216A at 4x Concentration.	124
78. 6.19 FRETplexing Assay for 216T 1x Concentration	128
79. 6.20 FRETplexing Assay for 216T 2x Concentration	128
80. 6.21 FRETplexing Assay for 216T at 1x and 216A at 4x Concentration	131
81. 6.22 FRETplexing Assay for 216T at 1x and 216C at 2x Concentration	132
82. 6.23 FRETplexing Assay for 216A at 4x and 216C at 2x Concentration	132
83. 6.24 FRETplexing Assay for 216T at 1x, 216A at 4x, and 216C at 2x	
84. Concentration	133
85. 6.25 FRETplex emission intensities (delta values) obtained from FIGs.	
86. 6.19-6.24.	134
87. 6.26 Wild Type Concentration Calibration Experiments Using	
88. FRET-Chromophore-Labeled Primers with qPCR.	136
89. 6.27 KRAS Yes No Diagnostic Assay	137
90. <i>Tables</i>	
6.1 Sequence and Primers of STI Initial Test Panel for Quenchiplexing Assay	
91. Development.	108-109
6.2 Experimental Volumes and Concentrations used for the STI Initial	
92. Experimental Test.	110
6.3 Sequences Used for KRAS Mutation Experiments.....	111
6.4 Sequence and Primers of KRAS Test Panel for Quenchiplexing Assay	
93. Development.	112
6.5 Experimental Protocol for KRAS Quenchiplexing Experiment.	113
6.6 Experiment Cocktail for Quenchiplexing Detection of a Single 216C	
94. Mutation	117
6.7 Experiment Cocktail for Quenchiplexing Detection of a Single 216T	
95. Mutation	118
6.8 Experiment Cocktail for Quenchiplexing Detection of a Single 216A	
96. Mutation	118
6.9 Experiment Cocktail for Quenchiplexing Detection of a Double Mutation	
97. 216T at 2x and 216C at 1x Primer Concentrations	121
98. 6.10 Experiment Cocktail for Quenchiplexing Detection of a Double	
99. Mutation 216T at 2x and 216A at 4x Primer Concentrations	121
100. 6.11 Experiment Cocktail for Quenchiplexing Detection of a Double Mutation	
101. 216C at 1x and 216A at 4x Primer Concentrations.	121
6.12 Experiment Cocktail for Quenchiplexing Detection of a Triple Mutation	
216T at 2x and 216C at 1x and 216A at 4x Primer Concentrations.....	122
6.13 Sequences of Primers for KRAS FRETplexing Assay Development.	125
6.14 Experiment Cocktail for Detection of a Single 216T Mutation Using	
102. FRETplexing.	127
6.15 Experiment Cocktail for Detection of a Single 216T Mutation Using	

FRETplexing.....	127
6.16 Experiment Cocktail for Detection of a Double Mutation 216C at 2× and	
103. 216T at 1× Primer Concentrations Using FRETplexing.	129
6.17 Experiment Cocktail for Detection of a Double Mutation 216C at 2× and	
104. 216A at 4× Primer Concentrations Using FRETplexing.	130
6.18 Experiment Cocktail for Detection of a Double Mutation 216T at 1×	
and 216A at 4× Primer Concentrations Using FRETplexing.....	130
6.19 Experiment Cocktail for Detection of a Triple Mutation 216C at 2× and	
105. 216T at 1× and 216A at 4× Primer Concentrations Using FRETplexing.	131
6.20 FRETplexing Experiment Cocktail for Control Experiments Using Wild	
106. Type Sequences.	135
107.	
108.	
109.	
110.	
111.	
112.	
113.	
114.	
115.	
116.	
117.	
118.	
119.	
120.	
121.	

NOMENCLATURE

APTS. Aminopropyltrimethoxysilane

BMD. Biomarker Monitoring Device

BSA. Bovine Serum Albumin

CE. Capillary Electrophoresis

CRC. Colorectal Cancer

CTC. Circulation Tumor Cell

Cy 3. Cyanine 3

Cy 5. Cyanine 5

DARPA. US Defense Advanced Research Projects Agency

DCF. Delayed Craft Function

DNA. Deoxyribonucleic Acid

EBPG. Electron Beam Pattern Generator

EDC. 1-Ethyl-3-(3-(dimethylamino) propyl) Carbodiimide

ELISA. Enzyme-Linked Immuno Sorbent Assay

FAM. Fluorescein Amidite

FRET. Forster Resonance Energy Transfer

HER2. Human Epidermal Growth Factor Receptor 2

HPLC. High-Performance Liquid Chromatography

IL-18. Interleukin-18

IPA. Isopropyl Alcohol

KRAS. Gptase KRas

LB. Luria-Bertani

LtC640N. Light Cyclor 640

MD. Microfluidic Devices

MDD. Medical Devices and Diagnostics

MSP. Membrane Scaffold Protein

NGAL. Human Lipoclin-2

NIH. National Institute of Health

PCR. Polymerase Chain Reaction

PBS. Phosphate Buffered Saline

PDMS. Poly(dimethylsiloxane)

RNA. Ribonucleic Acid

RT-PCR. Real-Time Polymerase Chain Reaction

SLED. Superluminescent Light Emitting Diode

SNP. Single-Nucleotide Polymorphism

SOI. Silicon on Insulator

SPRs. Surface-Plasmon-Resonance-Based Sensors

STI. Sexually Transmitted Infection

qPCR. Quantitative PCR

UV. Ultraviolet Light

Chapter 1

Development of Microfluidic Devices with the Use of Nanotechnology to Aid in the Analysis of Biological Systems Including Membrane Protein Separation, Single Cell Analysis, and Genetic Markers

Introduction

Since the early 1990's, medical devices and diagnostics (MDDs) have enjoyed success and development within certain medical niche applications, such as blood sugar monitors and heart rate monitors. Recent advances and innovations, however, have the potential to make medical device technology a ubiquitous technique that could be used by almost every field of science; by bringing the laboratory to the field with the advent of nanotechnology development and fully integrated devices. MDDs have the potential to integrate an entire laboratory onto a single chip system. The devices ensure the reduction of reagent volumes and reaction times, making them cost effective for any lab environment. Furthermore, the reduction of sample size by use of chip technology provides an excellent opportunity for science to turn "green" with the reduction of waste products. Potential applications for utilizing chip technology in MDDs include the testing of pharmaceuticals and biotechnology products for drug discovery and development, development of medical assays and portable testing devices, isolation, and separation of proteins to evaluate function/structure relationships, detecting nano- and pico-gram quantities of chemicals or biological agents that may be used for terrorist activities, and the rapid detection of disease states to address public health issues.^{1,3,4,6} The first generation of MDDs now entering the marketplace emphasize flexibility and usefulness in a variety of contexts, a trait that the industry deems crucial to the device's commercial

success, such as Motorola Labs single-use portable self-contained full-scale automated DNA amplification and detection device (Figure 1.1).⁵

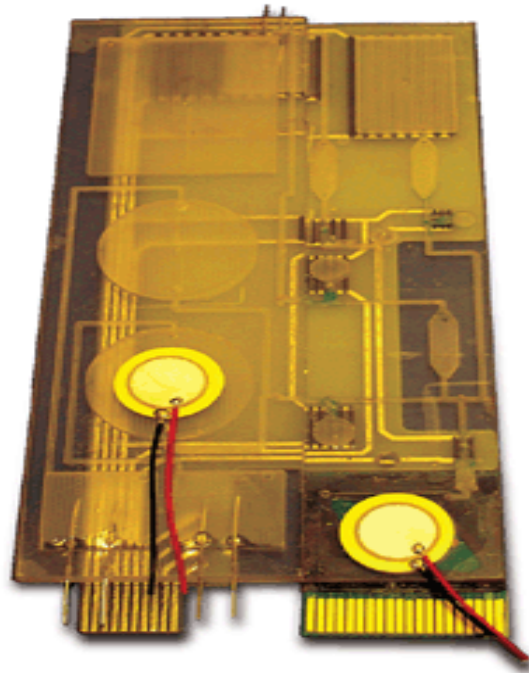


Figure 1.1. Self-contained Microfluidic Device. This Microfluidic device was a one-time-use only system developed by the Motorola Corporation for DNA amplification and detection. Unfortunately, it was a single-use only system.

One of the great appeals of MDDs is the interdisciplinary nature of the application. With the advent of microfluidics, optics, and microchip technology, numerous scientific methodologies and almost any technique has the potential for miniaturization. Another indication that MDDs have become a critical area of examination is the proliferation of journals focusing specifically on MDDs, as exemplified by the journal *Lab on a Chip* (Figure 1.2).



Figure 1.2. Lab on a Chip.²⁵ An academic journal dedicated to advances in microfluidic research.

Basic Principles

Microfluidics refers to a set of technologies that control the flow of minute quantities of liquids, and on rare occurrences, gases produced in the device. The first MDDs manipulated solutions of less than 1 mL. Today, microfluidic laboratories are using fluidics that measure nano- and pico-liter amounts of sample.⁷ “Unlike microelectronics, in which the current emphasis is on reducing the size of transistors, microfluidics is focusing on making more complex systems of channels with more sophisticated fluid-handling capabilities,” as detailed by George Whitesides, of Harvard University.⁸ Although micro and macrofluidics systems require similar components, including pumps, valves, mixers, filters, and separators, the physics behind the two types of fluids are completely different. As the scale decreases from macro to microchannels, the flow of fluid begins to behave differently at the microscale. Surface tension, viscosity, and electrical charges can become dominant forces on the microfluidic flow, because the surface-to-volume ratio is much greater than for macroscale systems. In the microfluidic

system, fluid reacts differently than for larger fluid volumes; hence, microscale components require new fabrication methods.

All of the current challenges in generating microfluidics relate to the ability to control the movement of the fluid inside the device. Traditional methods used for controlling fluid movement are not effective when scaled to the small volumes used in microfluidics; the physics behind the movement of fluid is different for very small volumes.¹³ For example, the forces (surface tension) exerted on very small volumes by the wall of the channel can restrict flow rates or cause particles to fall out of solution. In contrast, the surface forces exerted upon the movement of large volumes of fluid in a channel are negligible, because the surface to volume ratio is small. Thus, the critical element needed for this field to develop is a reliable mechanism to control the movement of the solution inside the device.¹¹ It is one thing to simply inject liquid into a chip and generate a reaction, but having the ability to direct that fluid into a series of channels and divide it into numerous samples represents a level of sophistication that has yet to be perfected in microfluidic devices.

History

The microfluidic medical devices first developed in the early 1990s were initially fabricated in silicon and glass using etching techniques adapted from the photolithography industry, as shown in Figure 1.3.^{10,12} The generation of these devices was a time consuming process, often taking

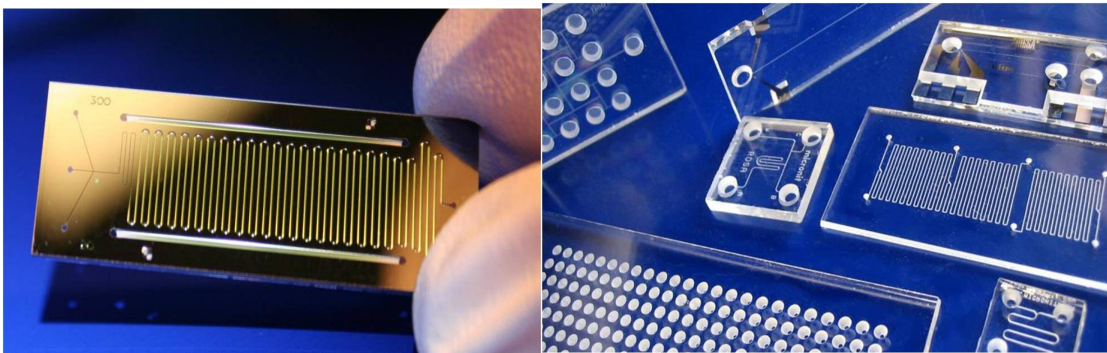


Figure 1.3. Common Glass Microfluidic Device. Typical microfluidic devices found in the commercial market.

several days or even weeks to fabricate. The devices that were generated using this technique demonstrated excellent precision but were very expensive to produce, and were very inflexible, since they were all fabricated out of glass, which made widespread use impracticable. The current trend in microfluidic chip development has moved toward the application of soft lithography fabrication methods, based on printing and molding of organic materials; poly(dimethylsiloxane) (PDMS) is the most widely used silicon-based organic polymer used to build microdevices, but there are many other polymers that can be used, each with its own unique chemical features.

Microfluidics have shown great appeal for a number of applications, because they require only a small amount of volume and reagent (nanoliters) needed to perform tests, compared to microliter or milliliter requirements for existing standard laboratory test methods. Microscale reactions also occur at a much faster rate because of the unique physics of small fluid volumes; diffusion requires less time in a nanoliter volume than for larger microliter volumes. The current drive for microchip development is to make MDDs that prepare samples and perform automated routine assays. Such lab-on-chip

technologies hold the promise of turning a single chip into a multi-function laboratory, equipped to perform a series of applications (purification, protein labeling, reactions, separation, and detection) all within a volume of less than one microliter.

Fabrication

Photolithography fabrication of microfluidic chips begins with a horizontal channel design of a microfluidic pattern layout using a CAD program and with a high resolution printer, and that is printed on a transparency (Figure 1.4).¹⁴ Silicon wafers are obtained with the desired maximum microfluidic dimensions, using a wafer placed on a spincoater (Figure 1.5) to deposit a thin layer of the appropriate photosensitive polymer (photoresist). The photoresist becomes the horizontal distance of the microfluidic channel, so the rotation speed is determined by the thickness of the desired channel and the viscosity of the specific resist.⁹ Several types of photoresist are available, which can generate devices with a channel size range between 1-400 μm .

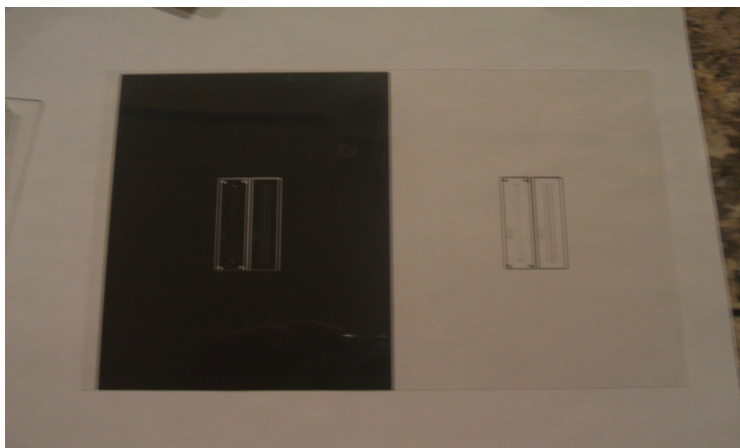


Figure 1.4. High Resolution Printer Transparency. Channel designs to generate masks for photolithography.



Figure 1.5. Spincoaters. Spincoaters are used to apply photoresist to silicon wafers.

Once the desired photoresist is applied, the wafer-photoresist mask is baked to remove the photoresist solvent layer. Once baked, the wafer is exposed to ultraviolet light through the overlaying transparency made using the CAD program. The mask-aligner (Figure 1.6) allows for the exact placement of the transparency onto the wafer. When generating a multilayer microfluidic, as seen in Figure 1.7, the mask-aligner allows the precise lineup of different transparencies to generate complex features. Instead of having a single layer microfluidic chip, layer upon layer of channels that interact with each other can be designed to fit any custom application (Figure 1.7). The ultraviolet light exposure is pictured in Figure 1.8.



Figure 1.6. Mask-aligner. An instrument used for multilayer fabrication and exposure of the microfluidic wafer to UV light.

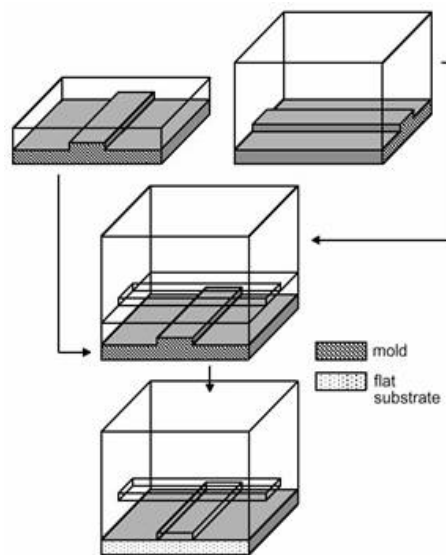


Figure 1.7. Multilayer Fabrication Diagram Expressing How Valves can be Generated in Microfluidic Devices .²⁴

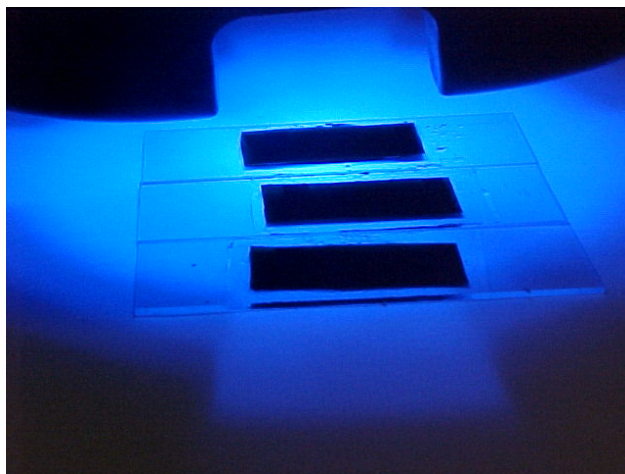


Figure 1.8. UV Exposure of Photoresist. Mask aligner exposure of photoresist-covered microscope slides with high-resolution transparencies.

Once the wafers are developed, the transferred microfluidic pattern is present on the silicon wafer. The areas of the photoresist that are exposed to ultraviolet light have different chemical properties than the unexposed photoresist. During the developing process, the unexposed photoresist dissolves faster than the exposed region, leaving the desired microfluidic pattern. The pattern is then used with a desired polymer to make the microfluidic device. For most devices, the polymer is poly(dimethylsiloxane) (PDMS). Once a microfluidic device is fabricated, the channels are exposed to the environment, allowing the chips to become plasma oxidized binding the polymer to the glass substrate.

Several microfluidic laboratories have used these techniques for the construction of three-dimensional networks of channels and components.¹⁹ Figure 1.7 reveals how two overlapping channels can be used to create a microfluidic valve that provides a high level fluid flow control.¹⁷ Using a similar technique, microfluidics constructed with a multilayer system can control the movement of fluid to different segments of the device for controlled reactions.¹⁶ This method of fabrication has its advantages, especially when

using semiconducting material to generate microfluidic devices. The following chapters will question the idea of just using wafers as a mask for microfluidic device development.

Ink-Jet to Biochips

Microfluidic technology started in the computer industry with ink-jet printing. Ink-jet printers use orifices of less than 100 μm in diameter to generate drops of ink onto the paper (Figure 1.9). In this simple process, printers control a small amount of the fluid, making them the first MDD. This same ink-jet technology is now used in biotechnology to deliver reagents to microscopic arrays on the surface of biochips.¹⁵ These biochips are used in many different scientific fields, especially in the pharmaceutical industry where arrays are used to determine drug reactivity.

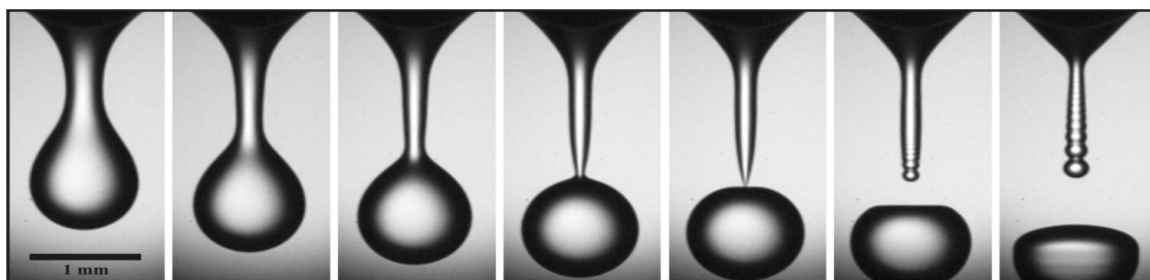


Figure 1.9. Microfluidic Droplets from an Ink-Jet Printer.²⁶

Just like the ink-jet printers, most microfluidic devices use electrokinetic and pressure methods to move small amounts of fluid around a microchip. The manipulation of fluid is the key principle for developing medical devices. Unfortunately, the techniques described above are useful only for certain microfluidic applications, particularly medical devices that only require straight channels; for many other applications, having a microfluidic device that has channel flexibility is essential.

In the late 1990s, Stephen Quake fabricated three-dimensional structures from multiple layers of soft elastomer by imprinting each layer and then binding them together to form the pumps, valves and channels integral to the microfluidic chip.²⁴ This enabled a single microfluidic chip to serve many functions. With three-dimensional microfluidics, sample preparation, manipulation of live cells, perfusion of reagents, and analytic sample detection can be achieved on a single device, providing flexibility in fluid manipulation to generate small lab-on-chip systems.

Polymers

MDDs are fabricated from polymers that are cured on a template created from the remaining photoresist. Of the readily available polymers, the most widely used is PDMS (Figure 1.10). PDMS is a silicon-based organic polymer that is extremely inexpensive. Once cured, the polymer (< 200 microns) is visibly clear, capable of providing a platform for fluorescence detection, as seen in Figure 1.11.¹⁶ The polymer is very versatile when applied in the liquid form and baked, and the polymer will take the shape of any design. However, the polymer cannot handle harsh solvents or high pressures and is only partially transparent to ultraviolet light (UV), where the thickness of the polymer determines the amount of UV transparency. There are other polymers used to make MDDs. For example, sifel is a perfluoropolyether backbone with a terminal silicone cross-linking group that has the potential to take the place of PDMS. It is stable to many organic solvents that degrade PDMS, but is expensive. In addition, it forms a cloudy material unlike PDMS, making detection through the polymer problematic. With all of the advantages that PDMS has in the field of microfluidic development, it is the best

material to use. The following chapters will address alternatives to PDMS that can still be optically transparent, yet have a greater reagent and pressure versatility not found in PDMS. Even though the cost is greater, the benefits of building fluidics inside semiconductor material enable cheaper medical devices.

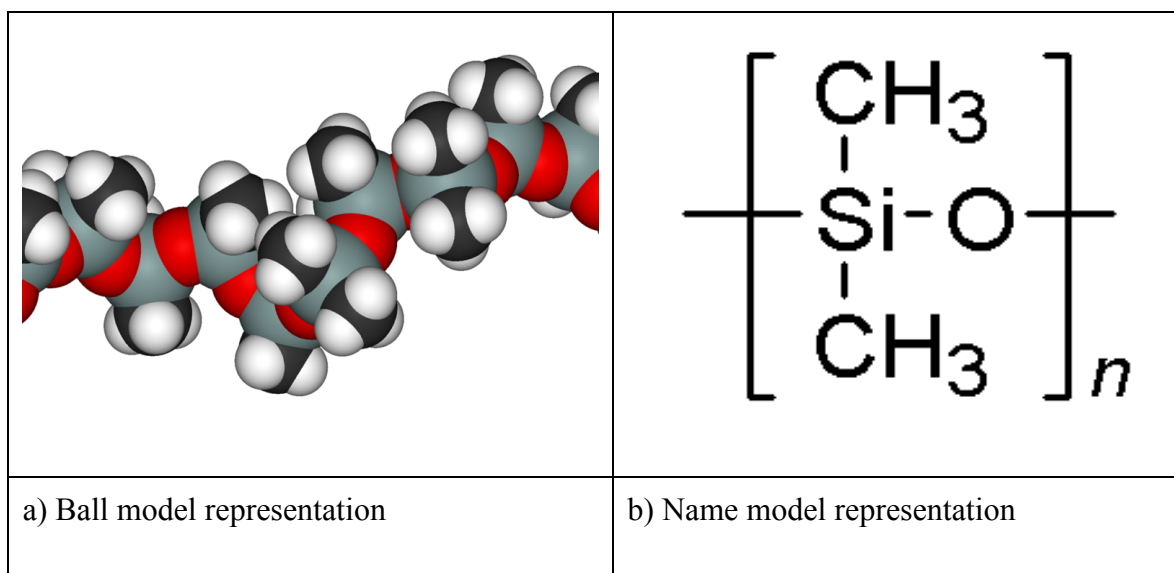


Figure 1.10. PDMS Structure. Chemical composition of PDMS polymer.

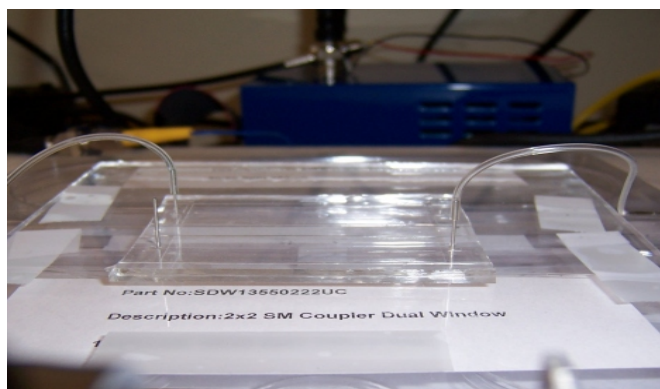


Figure 1.11. PDMS Microfluidic Device. Side view of a microfluidic device made from PDMS polymer.

Detection

There are several detection methods used with MDDs, including ultraviolet (UV) light, conductivity, magnetic binding, and fluorescence.¹⁸ Fluorescence detection is used extensively. Fluorescence occurs when a given wavelength of photons is directed to a molecule that triggers the emission of another photon with a longer wavelength. With this emitted light, the concentration of protein present can be quantified by knowing the extent of derivatization on a protein and how many green photons are being released. This detection method is highly effective for determining low concentrations of samples, yet fluorescence is much more of a versatile tool than a simple detection mechanism, and it might be possible to get more information using fluorescence to gather information other than concentration.

Conclusion

Over the next decade, the field of nanotechnology in conjunction with microfluidics will continue to evolve and advance, generating smaller, more complex MDDs. Instead of having samples shipped to diagnostic laboratories, samples will be processed in the field with little expertise. The US Defense Advanced Research Projects Agency (DARPA) envisions that microfluidics can solve the problem of inadequate medical care in the third world by reducing overall medical costs for detection and treatment of diseases, with the same high standards of detection that can only be found in modern medical laboratories.²¹ With skyrocketing medical costs, MDDs might also be the solution to help reduce overall medical expenditures.

Chapter 2

A Microfluidic-Based Method for Recovering Enhanced Enzymatic Activity of Membrane Bound Proteins

Introduction

One common system for determining protein function is to understand their tertiary structure using x-ray crystallography to reveal the outside surface geometry of the protein, which can be used to determine binding sites. The use of x-ray crystallography has yielded the 3-D structure of nearly all soluble proteins, but this method is limited, in that it cannot be used to determine the tertiary structure of membrane proteins, since these membrane proteins are not soluble under physiological conditions and are imbedded in a non-soluble lipid bilayer. As a result, the 3-D structures of only a small number of membrane proteins are known.

Membrane proteins represent important key regulators of material and information transfer between cells and their environment. They are the gatekeepers for the movement of material into and out of the cell. Membrane proteins also serve as structural elements of the cell itself, and between compartments comprising organ systems. Specific defects in membrane proteins are associated with many known diseases and as such, are the targets of many pharmacologically and toxicologically active substances to treat disease. Thus, an improved understanding of membrane proteins should provide stronger more selective drugs with fewer side effects. Understanding of the structure, function, and mechanisms of integral membrane proteins is difficult due to the limitations of successfully separating and purifying proteins from their encasing lipid environment.

The isolation of membrane proteins, to study their physiological activity, is limited, since many of the current methods used for isolation denature the protein and change their 3-D conformational structure, which affects their function (binding capabilities, enzymatic activity, etc). When protein separation from the lipid environment occurs, the 3-D conformation of the native protein, needed for understanding the molecular machine, is typically not the same conformation of the protein in the natural environment; hence only a limited amount of information can be obtained. A major hurdle to understanding the structure and function of membrane proteins is the reproducible procedure for isolating the membrane proteins in a mono-dispersed form that maintains the phospholipid-protein native structure and functionality.²⁷ Furthermore, many of the membrane protein functions are not independent, but require other proteins for activity; they are just one part of a network of proteins that can span all regions of the cell. Thus, the isolation of just one protein may not represent the complete physiological function.

Techniques are available to study the molecular structure and function of soluble proteins, but few techniques are available to study membrane proteins. One new method of isolating membrane proteins uses nanodiscs and allows for separation of protein with their membrane intact.²⁸ In this method, a cell membrane preparation containing the target membrane protein is totally solubilized with detergent in the presence of a membrane scaffold protein (MSP). After removal of the detergent by dialysis or by Bio-Beads, a soluble MSP-supported nanodisc is formed, with the target incorporated into the resulting phospholipid bilayer.²⁹ Unfortunately, in the nanodisc-based technique, the amphiphilic detergent (such as 0.5 M cholic acid) that solubilizes the membrane protein

simultaneously separates the proteins from their native lipid bilayer, affecting their structural and functional features.

Through the use of microfluidic technology, it is possible to isolate proteins from their membrane bi-layer without affecting the 3-D structure or functionality, by limiting the time that the detergent interacts with the membrane protein (see Figure 2.1). The precise control afforded by the lab-on-chip system, for the reaction between membrane proteins (sample) and a mixture of detergent and membrane scaffold protein (MSP) (reagent) to dissolve the lipid bi-layers into soluble nano fragments of transmembrane proteins, is influenced by regulating the flow rate, temperature controlling elements, and detergent quenching beads.

Microfabrication of a microfluidic chip

The first microfluidic devices were fabricated at Caltech's Nanofabrication Laboratory. These devices were manufactured with a complex network of valves and control channels that made the device difficult to use. Subsequently, microfluidic chips were fabricated at Kavli Nanoscience Institute. These microfluidic chips were of a simpler design, using only a one-channel layer with no complex valve

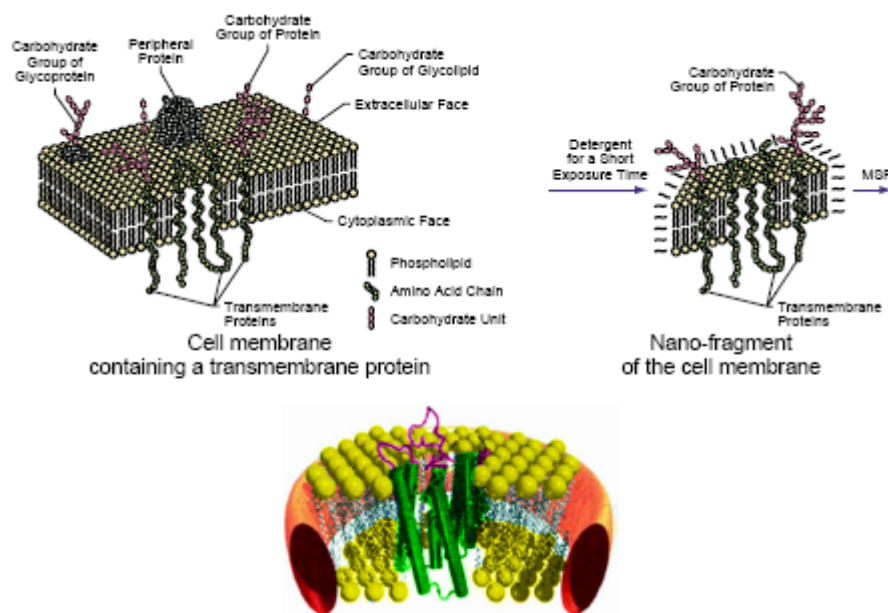


Figure 2.1. Schematic Presentation of the Membrane Isolation Preparation Process. Membrane proteins are removed from the membrane with some lipid still attached to the protein. The cell membrane images (Figure 2.1) are from Wolf.³¹

system. Each mold of the microfluidic device was fabricated from Dow Corning Sylgard 184, a two-part cure silicone cast on photoresist, which generates a master mold. The molds are made by spin-coating photoresist onto a silicon wafer, where the spin rate determines the horizontal distance of the microfluidic channel that is formed. A pattern with a high-resolution transparency mask (typically 3,386, 8,000, or 20,000 dpi) is placed on the silicon wafer with photoresist. The transparency mask determines not only the pattern of the microfluidic device, but also the maximum longitudinal distance of the channel. As a result, the only variable that can be controlled once a transparency mask is made is the vertical distance or thickness of the microfluidic channel itself. After the channel is formed, the unexposed photoresist is removed using developer and the

resulting wafer is washed in an alcohol solution (preferably isopropyl alcohol) and then deionized water. The resulting wafer is dried under compressed nitrogen and baked for 90 minutes in a 300°C oven. After the wafer is cooled, Poly(dimethylsiloxane) (PDMS) is added onto the surface of the wafer and baked until the polymer is hardened to produce the microfluidic chip, as seen in Figure 2.2.

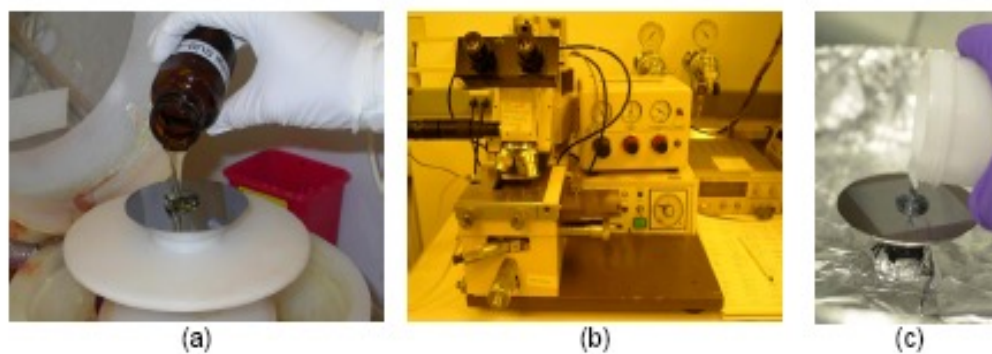


Figure 2.2. Microfluidic Chip Preparation: a) Application of photo resist, b) UV exposure of the wafer, c) PDMS application.

The resulting devices are cut from the mold and mounted onto thoroughly cleaned glass microscope slides. Mounting is accomplished by exposing both the glass and the microfluidic chip to plasma oxidation, and rendering their surfaces hydrophilic by creating silanol groups that interact with the glass surface. The completed microfluidic chip is presented in Figure 2.3.

Membrane Isolation

Rat membranes were custom isolated by the Burnham Institute (La Jolla, CA) according to the method of Meier *et al.*⁴⁰ Specifically, rats were euthanized and their livers were rapidly removed and chilled on ice. Ten-gram portions of liver were cut into small pieces, washed three times in 80 mL of cold 1 mM NaHCO_3 (pH 7.4), and homogenized in the same volume of 1 mM NaHCO_3 with a loose (Type A) Dounce homogenizer (seven up-and-down strokes). The homogenate was further diluted to 1800-2000 mL with cold NaHCO_3 and filtered twice through two layers of 60-grade cheesecloth. The filtered solution was centrifuged at $1,500 \times g$ for 15 minutes (GSA rotor, E.I. du Pont de Nemours & Co., Inc., Sorvall Instruments Div., Newtown, CT). The resulting “crude nuclear pellet,” was resuspended in 5.5 pellet volumes of 56% sucrose (wt/wt; density = 1.2623) and stirred for 15 minutes to disrupt membrane aggregates. The sample was dynamically loaded onto a 100 mL cushion of 56% (wt/wt) sucrose with a

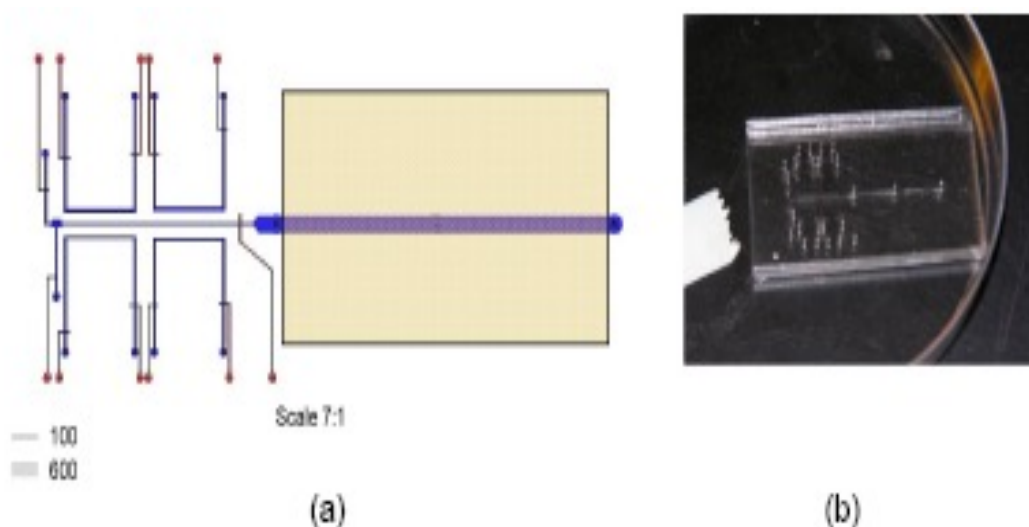


Figure 2.3. Microfluidic Design and Fabricated Device. a) Initial design of the microfluidic chip. b) Actual fabricated microfluidic chip.

variable-speed pump (Sorvall Instruments) into a zonal rotor (TZ28) and overlaid first with 400 mL of 44% sucrose (wt/wt; density = 1.1972), followed by 200 mL of 36.5% sucrose (wt/wt; density = 1.1587). The rotor was completely filled to its total volume capacity (1,350 mL) using 0.25 M sucrose. During the entire loading procedure, the rotor is running at 3,000 rpm. The completed discontinuous sucrose gradient system is centrifuged at 20,000 rpm for 120 minutes. After a slow deceleration to a complete stop, 70 15 mL fractions were collected from the bottom of the rotor. Each fraction was analyzed for density, turbidity (absorbance at 700 nm), and marker enzymatic (alkaline phosphatase) activity. Fractions containing the bulk of the plasma membrane fragments (e.g., fraction 54-64 out of 70) were combined and diluted with 250 mMol NaHCO_3 to 1,000 mL. The suspension was centrifuged in a rotary centrifuge at $7,500 \times g$ for 15 minutes and the pellet was gently resuspended (by vortex mixing) in 250 mL of NaHCO_3 pH 6.4. The resuspended material, representing the liver plasma membrane, was resedimented at $2,700 \times g$ for 15 minutes. A total quantity of 5 g of concentrated rat liver membrane in 250 mMol NaHCO_3 solution was received from the contract laboratory.

Cell membranes from *S. oneidensis* strain MR-1 were obtained from cultures grown in Luria-Bertani (LB) medium at 25°C. For aerobic growth (high oxygen), 20 mL of LB broth was inoculated with 1 mL of overnight culture and placed in a 250 mL flask which was incubated on a rotary shaker at 200 rpm. The cells were harvested at the exponential phase ($\text{OD}_{600} = 1$). For low oxygen growth, the speed of the rotary shaker was reduced to minimize oxygen uptake. The membrane sample from *S. oneidensis* was obtained from Dr. Vladimir Kery, Molecular Biosciences, Pacific Northwest National

Laboratory, according to our material transfer agreement. The membranes of *S. oneidensis* were prepared according to the method of Giometti et al⁵³ and separated from the soluble components by high-speed centrifugation.

Sample preparation procedure

A. Membrane Sample Preparation.

Frozen cells were thawed and immediately mixed with two volumes of lysis buffer containing 50 mM glucose, 10 mM EDTA, 25 mM Tris-HCl, pH 8.0, and 4 mg/mL of lysozyme in the presence of protease inhibitors (complete mini protease inhibitor cocktail; Roche Diagnostics, Indianapolis, IN). Lysozyme was added to the lysis buffer immediately before use. The solution was sonicated then shaken at 4°C for 12 hours. The resulting lysate was centrifuged for 40 minutes at 12,000g in a refrigerated Eppendorf centrifuge to remove unbroken cells. The supernatant was collected and centrifuged at 160,000g for 30 minutes in a Beckman (Beckman-Coulter, Fullerton, CA) TL100 tabletop ultracentrifuge, followed by an additional 10 minutes of centrifugation at 435,000g for further purification. The additional ultracentrifugation step increases the purity of the membrane sample since active lysate may still be present, degrading the desired proteins. The final supernatant was collected as the soluble cytosolic fraction, and the pellet was suspended in lysis buffer containing 0.5% w/v CHAPS detergent (Bio-Rad, Hercules, CA). The resuspended pellet was transferred into a chilled Dounce homogenizer and evenly dispersed with 10 slow strokes of the pestle. The dispersed

pellet was collected as the crude membrane preparation. The crude membrane fractions were stored at -80°C for further analysis.

B. Preparation of the Nano-Disc Samples: Rat Liver Membrane.

The concentrated rat liver membrane sample, prepared as described above, was diluted 100 fold with 0.05 mM Tris-HCl buffer pH 8.0. In accordance with the procedure for self-assembly of Nanodisks²⁹ the rat liver membrane was detergent-solubilized with 0.5 M cholic acid and mixed with human apoprotein A1 (University of California, San Diego Biology Department) and detergent in the approximate ratio of 1:100:200 (apoprotein/membrane/detergent). The reconstituted samples, which include approximately 100 nmol of scaffold protein, 10 mmol of membrane, and 20 mmol of cholate, were preincubated for 1.5 hours at 4°C. The detergent was removed by incubating with Bio-Beads[®] SM-2 Adsorbent (approximately 0.4 g Bio-Beads[®]/1 mL of reconstitution mixture) for 1.5 hours at 4°C.

C. Preparation of the Nano-Disc Samples: *Shewanella oneidensis* Membrane.

Nano-Discs containing *Shewanella oneidensis* membrane were prepared as follows. Concentrated *Shewanella oneidensis* membrane was diluted 100 fold with 0.05 mM Tris-HCl buffer pH of 8.0. The diluted sample was mixed with 0.5 M cholic acid and human apoprotein A1 in the approximate ratio of 1:100:200 (apoprotein/membrane/detergent) and incubated at 38°C for 1, 2, 3, 4, 5, and 6 hour time intervals. At the conclusion of each time period, the detergent was removed by incubating with SM-2 adsorbent beads for 2 hours at room temperature. All samples were filtered

through a 30 nm filter, and the concentration/absorbance of the solubilized cytochromes were measured in an ELISA reader at 410 nm. The concentration of the released transmembrane cytochromes gradually increased with an increase of the incubation time of the sample, reaching its plateau after 5 hours of incubation.

D. Preparation of the Membrane Nanofragments: Rat Liver Membrane.

Rat liver membrane was mixed with apoprotein A1 and 0.5 M cholic acid (detergent) in the approximate ratio of 1:100:200 (apoprotein/sample/detergent) and heated to 38°C. The heated sample was injected through separate ports of the microfluidic chip into the mixing chamber and stirred using magnetic nanobeads. Once the sample was mixed, the liquid was moved through the macrofluidic compartment, filled with SM-2 adsorbent beads (BioRad Laboratories, Hercules, CA) (approximately 0.4 g of BioBeads/1 mL), cooled to 4°C, and sent into the outflow port of the chip. A microfluidic membrane separation was performed using incrementally increasing flow rates of 1 mL/minute, 5 mL/minute, 10 mL/minute, 20 mL/minute, and 50 mL/minute. The processed samples were collected in centrifuge tubes at the outflow port and analyzed.

E. Preparation of the Membrane Nanofragments: *Shewanella oneidensis* Membrane

The *Shewanella oneidensis* membrane sample was incubated in 0.5 M sodium cholate at 38°C for 2 hours prior to initiating the separation procedure. After the conclusion of the heat-treatment step, the treated sample was mixed with apoprotein A1

and 1.5 M sodium cholate and again heated to 38°C. The mixture was injected into the mixing chamber of the microfluidic chip, and moved to the macrofluidic separation compartment as described previously. The membrane separation process was performed using low flow rates of 0.1, 0.5, 0.8., 1.0, and 2.0 mL/minute. The processed samples were collected in centrifuge tubes at the outflow port and analyzed.

Apparatus

The microfluidic chip apparatus that was used for the membrane protein isolation studies is described in Figure 2.4. The design of the chip uses two solution ports, one for membrane samples and the other for detergent. There is a mixing chamber for the two solutions to interact and start the reaction between the detergent and membrane solutions. Two parallel warming channels are used to increase the reaction temperature to 38°C. Conversely, two parallel cooling channels are used to reduce the temperature of the reaction to 4°C. The final process releases the solution to the quenching bead chamber.

Experiment

A. Fluid mixing

The initial concept to use nano-magnetic beads in the microfluidic mixing chamber was to stimulate the mixing of the two fluids, while preventing laminar flow. Experiments with unfunctionalized magnetic nanobeads (DynaL Biotech) were designed to introduce vortices within the fluid flow region and, therefore, enhance mixing. However, the direction of the nanobead movement, using an external magnet (Figure 2.5), was not able to overcome the energy provided by the flow rate. The nanobeads would follow the

solution flow aligned with the magnetic field, but they did not greatly disturb the laminar flow. Figure 2.6 shows that the magnetic beads are experiencing laminar flow even though there is a rare earth magnet trying to collect the beads into the chamber.

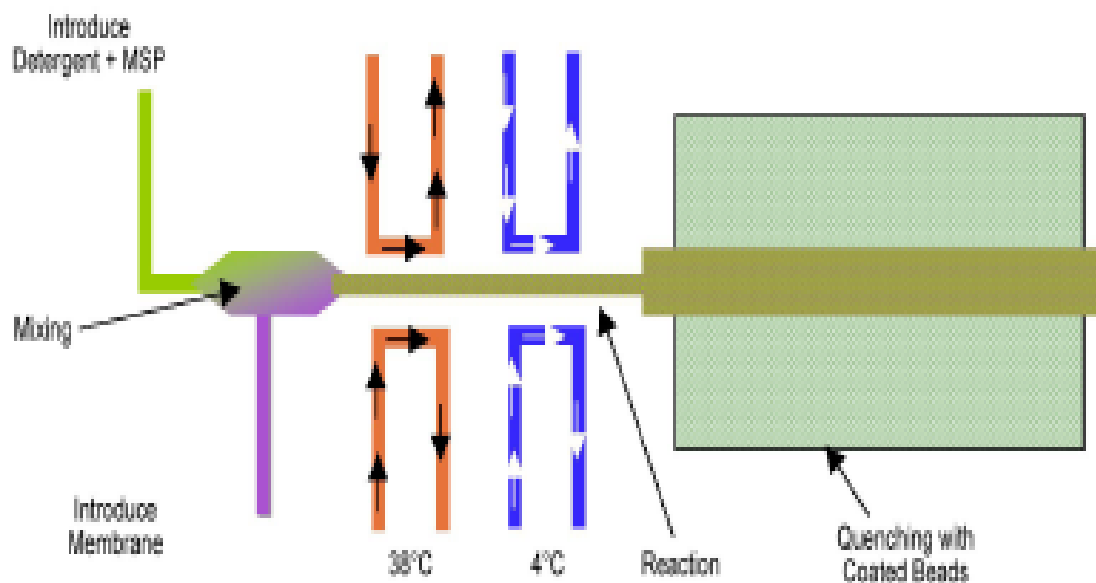


Figure 2.4. **Conceptual Function of the Microfluidic Device.** Description of how the microfluidic chip controls fluid movement and reaction temperature to perform the membrane separation reaction.

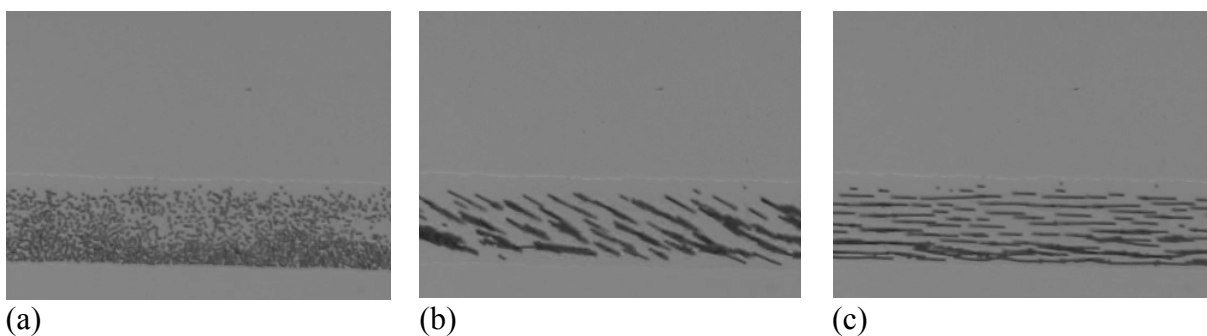


Figure 2.5. Magnetic Beads in the Reaction Chamber: a) A magnified view of a microfluidic channel with magnetic beads; (b and c) In the presence of a rare-earth magnet at two orientations.

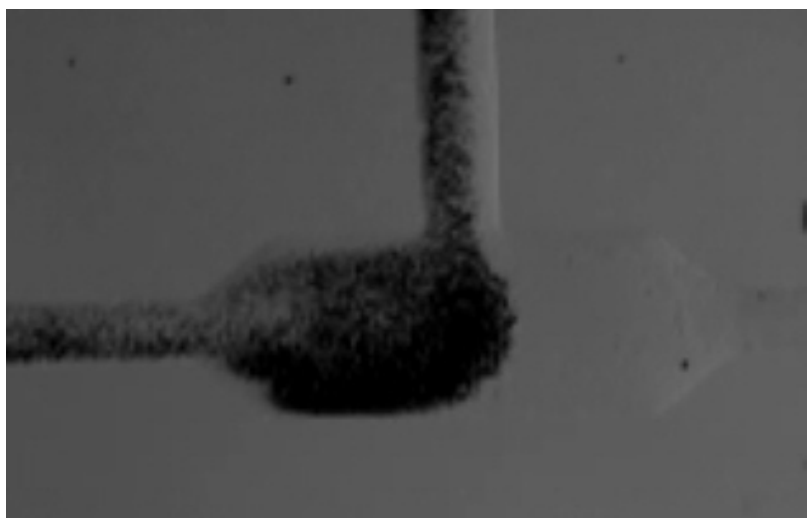


Figure 2.6. Laminar Flow out of the Reaction Chamber. Nanobeads in the reaction chamber demonstrating how the magnetic beads move by laminar flow out of the reaction chamber.

The final microfluidic device design naturally produced a laminar flow of the sample in a reaction chamber, sandwiched between two identical reagent flows (Figure

2.7), and it was this system that was used as a solution mixing control indicator. By controlling the relative ratio of sample and reagents, and their total flow rates, the reaction time can be precisely determined, which is governed by diffusion of sample/reagent and the length of the microfluidic channel. The fluid layer channels are 100 μm wide and approximately 25 μm high, which can hold a maximum of 11 nL of solution. Mixing was achieved by a laminar-flow mixing system, and the mixing time was determined by the diffusion time between the sample and reagent flows. Given that the sample and reagents react as long as they are in contact with each other, by controlling the distance (channel length) they travel and rate at which they travel (flow rate) the diffusion limited reaction time can be accurately controlled.

B. Analytical procedures

The microfluidic protein isolation system was evaluated using both eukaryotic and prokaryotic microbial membranes. The extracted nanofragments were filtered with a 30 nm polycarbonate filter, to select all fragments smaller than 30 nm and the concentration/absorbance of the solubilized cytochromes was measured in ELISA reader at 410 nm. The concentration of the released transmembrane cytochromes gradually increase, with the increase of the incubation time of the sample, reaching its plateau at 5 hours of the incubation. As a control, the activity of the unfiltered starting sample was compared to that of the filtered sample.

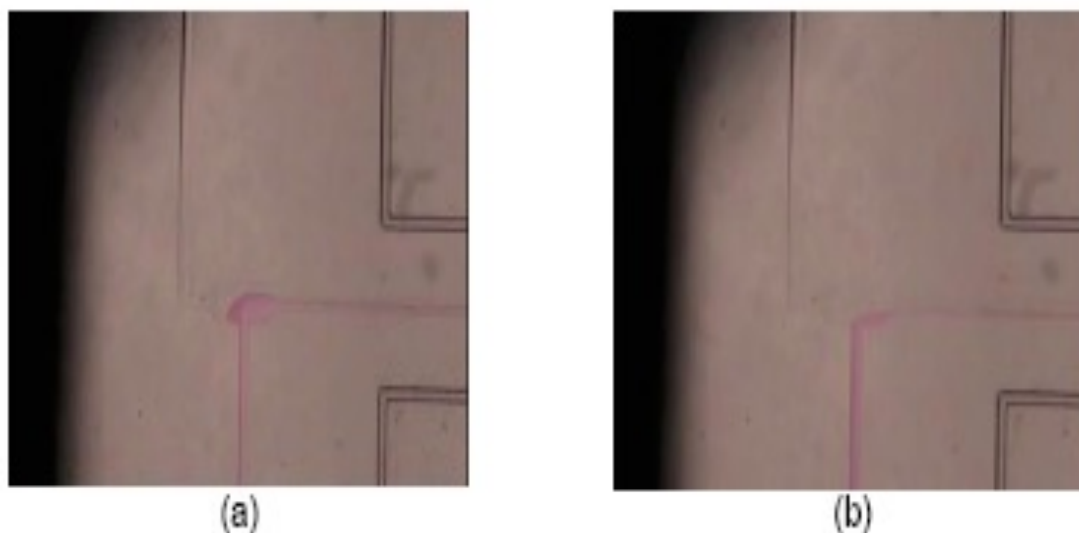


Figure 2.7. Laminar Flow Diagrams. a) Membrane flow rate exceeds the flow of the detergent channel. b) Detergent flow rate exceeds the rate of the membrane channel.

Alkaline phosphatase activity was measured in ELISA microplates using 150 μ L of each of eight samples. The microfluidic chip samples were collected at flow rates of 1, 5, 10, 20, and 50 μ L/minutes. A Nano-Disc sample and unprocessed, filtered, and unprocessed unfiltered samples were included in the assay. A reaction mixture/incubation medium (150 μ L) consisting of 0.5% p-nitrophenylphosphate and 1 mM MgCl_2 in 0.05 mM Tris-HCl buffer of pH 8.0 was added to the triplicate samples.

Control samples for the enzymatic reaction consisted of buffer only and twice diluted incubation medium without sample, as a reaction mixture control. The microplates were incubated at 37°C in sealed Ziploc bags to prevent evaporation. The enzymatic reaction was stopped after 15 minutes by adding 100 μ L of a 1 M potassium phosphate solution. An incubation time of 15 minutes was determined from prior studies

as optimal for enzyme activity. The optical density of the p-nitrophenol product released was measured by an ELISA reader at 410 nm.

In addition to an alkaline phosphatase assay, the activity of peroxidase was measured in ELISA microplates using the same samples, controls, and assay methods as described above. The optical density of the peroxidase products was measured in an ELISA reader at 450 nm.

Results

Since laminar flow was used to mix the membrane with the detergent solution, as the flow rate increased the amount of time needed to fill the microfluidic chip decreased and lowered solutions interacting with one-another for membrane separation. The data presented in Figure 2.8 demonstrates the relationship between flow rate and interaction time to limit protein degradation, as the flow rate increases the amount of time needed to fill the 10 nL device is reduced.

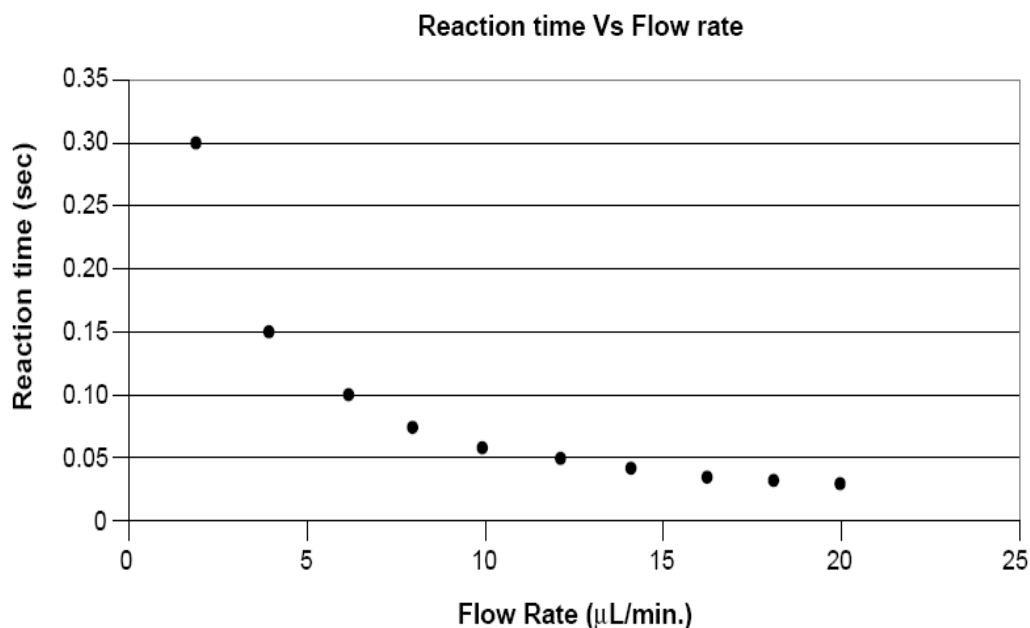


Figure 2.8. Reaction Time Vs Flow Rate. The reaction region is estimated to contain approximately 10 nL of material.

The current best membrane separating system available for extracting proteins from prokaryotic cell membranes is the Nano-Disc system, which only generates an ELISA optical activity reading of around 0.15 (Figure 2.9). In contrast, when the microfluidic chip system is used on the same membrane source by controlling the flow rates, the separation yield is almost twice the optical activity density. The data also reveals that at every flow rate measurement, the microfluidic system is equal to or better

ELISA Reading vs. Flow Rate for *Shewanella oneidensis*

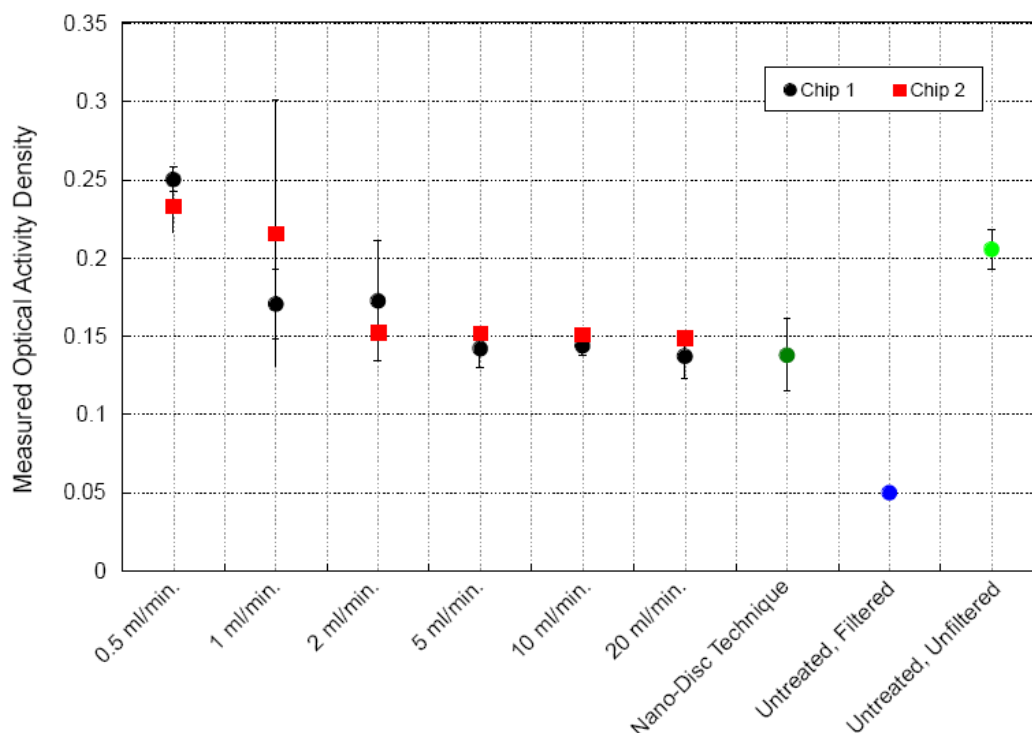


Figure 2.9. Activity of the Peroxidase Enzyme. 15 membrane samples of the *Shewanella oneidensis*: Microfluidic chip samples at 0.5; 1.0; 2.; 5.0; 10.0 and 20.0 mL/minute flow rate obtained from two separate chips, Nano-Disk sample (all filtered through 30 nm membrane filter), unprocessed filtered, and unprocessed unfiltered sample measured in ELISA microplates at 450 nm.

than the current technology. The data also demonstrates that the system is not microfluidic chip dependent, since multiple reproducible results were generated in three separate experiments, revealing that these devices can be mass-produced with consistent results.

ELISA Reading vs. Flow rate for Fat Liver Cell.

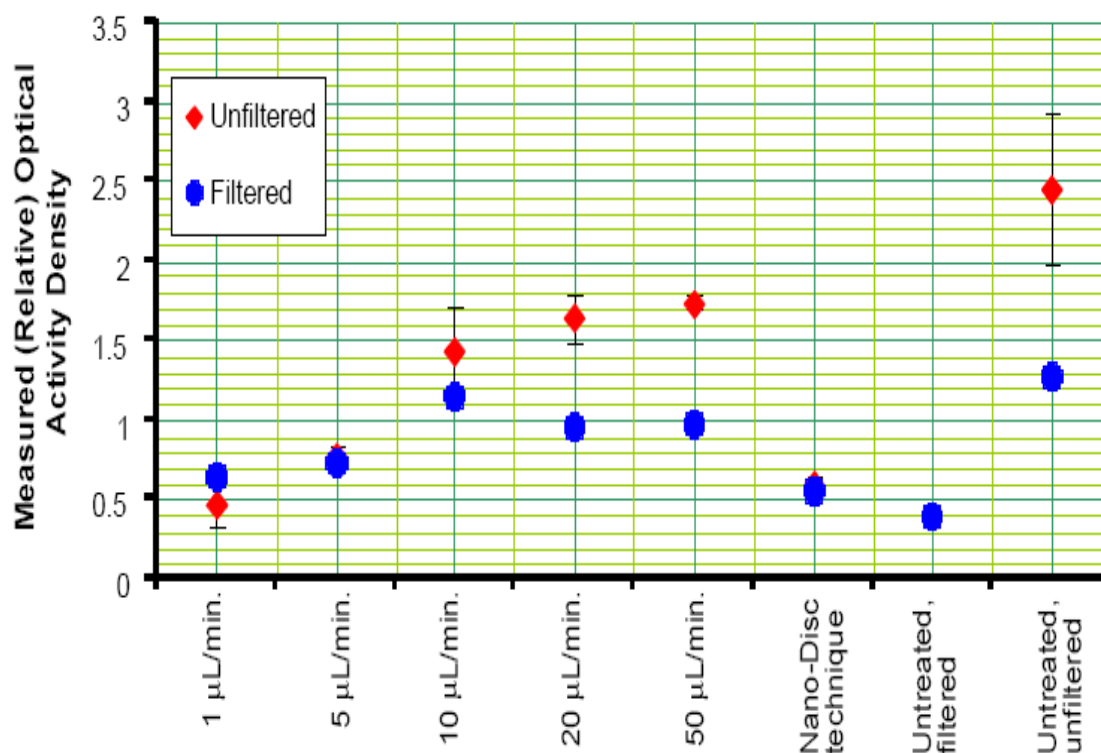


Figure 2.10. Activity of Alkaline Phosphatase. Sample of rat liver cells are run at 1 mL/minute, 5 mL/minute, 10 mL/minute, 20 mL/minute, and 50 mL/minute flow rates in the microfluidic chip; Nano-Disc sample filtered through 30 nm pore filter (blue) or unfiltered (red), unprocessed, filtered and unprocessed unfiltered, sample measured in ELISA microplates by means of an ELISA reader.

From the data presented in Figure 2.10, all experimental flow rates consistently showed equal or greater activity than the conventional Nano-Disc technique, with the microfluidic chip method yielding peak flow rates that contain two times the activity of the conventional method. This suggests that with the same sample size, the microfluidic system is able to generate almost twice the amount of separated active protein. As with

the prokaryotic cell membrane, the eukaryotic rat liver membrane proteins can be isolated using the microfluidic chip by controlling the solution mixing to ensure active membrane separation.

Conclusion

Membrane bound proteins are the most difficult type of proteins to separate. There are only a handful of membrane bound proteins that have been isolated. Proteins that have been isolated typically have a denatured structure since the membrane is out of its native environment. Membrane proteins have both hydrophobic and hydrophilic regions, when imbedded into the cell membrane. Membrane bound proteins can be isolated from both eukaryotic and prokaryotic cell types using a microfluidic platform, with retention of activity that is far greater than using traditional separation techniques. With the precise control over the protein and detergent solution which microfluidics provides, proteins are clipped out of the membrane in small lipid disks, which now act like soluble proteins and can be studied by traditional methods. The active density of the ELISA test revealed that the amount of isolated protein is up to twice the concentration of that obtained from traditional methods. This technique furthers our understanding of how proteins function in a membrane system, because we can get key insights about their structure from their interaction with isolation media chemicals. Unfortunately, the ability of separating membrane bound proteins without denaturing is only one part of the problem in researching membrane bound proteins. The other key issue is that many membrane bound proteins require other proteins for their proper function. By simply separating one protein and studying its structure and some of its function without the

other proteins, there will still be unanswered questions. For future research, when a membrane protein is isolated it should also be examined with other cellular proteins to see if there are protein-protein interactions.

Chapter 3

A Microfluidic Approach to Generate a Biomarker Monitoring Device

Introduction

It is well established that early detection of disease or rapid treatment of an injury will enhance an individual's survival rate or minimize long-term injury. For a number of years, researchers have attempted to identify biological indicators that signal the onset of a disease or injury. These biological indicators have become known as body-borne biomarkers. These biomarkers provide vital information about a person's health status and physiological effects of medications.⁵⁴ Advances in proteomics have led to the discovery of a number of human biomarkers associated with diseases, post therapeutic reactions, and physiological conditions that signal developing cancers. Biomarkers provide an opportunity for the early detection of previously untreatable or low survival rate maladies, such as organ system failures.

Rapid detection and identification of biomarkers, using body fluid samples, will not only aid early diagnosis and treatment of several diseases and adverse physical conditions, but have the potential to extend the average human lifespan by providing critical physiological data about the body before major damage can occur. Among the various types of biomarker detection technologies available today, a few are portable and do not require an expert to perform the diagnostic tests. These biomarkers are based primarily on four principles: electrochemical sensing,⁵⁵ mechanical (piezoelectric) sensing,⁵⁶ electrical impedance sensing,⁵⁷ and optical sensing.⁵⁸ The first three methods are known to be susceptible to environmental conditions (temperature, humidity, etc.),

and therefore produce a high percentage of false positives under ambient conditions. The fourth method can be classified into three main categories: fluorescence sensors, ellipsometric and interferometric sensors, and surface-plasmon-resonance-based sensors (SPRs).⁵⁹ Fluorescence sensors require labeling of sample biomarkers for sensitive optical detection and are therefore time consuming to produce and require expert users. Fluorescence labeling also has the problem of needing a dark environment for reading the sample. In addition, the shelf life of each fluorescence label, if not stored properly, is only a few minutes to a couple of hours due to a high probability of photo bleaching. Ellipsometric and SPR sensors use several discrete optical components such as polarizers and analyzers, making them expensive and very sensitive to vibrational instability. Since these components need to be perfectly aligned to provide an optimal signal, any field applications where the device experiences excessive vibrations will produce poor results. Interferometric methods have limited throughput because of their complexity and lengthy signal processing times. Therefore, currently available point-of-care devices for the detection and measurement of biomarker concentrations, using this detection method are not appropriate for field applications requiring high throughput, field ruggedness, and ease of use by nonmedical personnel. Thus, given the limitations of each of these detection mechanisms, a new diagnostic system needs to be generated to not only withstand the harsh conditions provided in non-laboratory field applications, but to also have the sensitivity and throughput needed to detect biomarkers.

Biomarker monitoring device (BMD) performance is based upon optical loss characteristics during light propagation through an optical waveguide, with a surrounding medium that changes the refractive index through the specific surface binding of

biomarker proteins. As the density increases, the amount of light able to reach the detector increases. A BMD incorporates a self-referencing mechanism to effectively eliminate false readings induced by changes in the light source and/or in ambient conditions. The BMD system requires a very small volume of reagent (<100 uL) and very little sample preparation, making it ideally suited for field applications and laboratory experiments. In addition, non-experts design the BMD for use, since the only requirement is injecting the sample into the correct inlet and running washing solutions between tests.

A prototype BMD demonstration system was prepared using a custom-designed multimode optical waveguide sensor, consisting of four channels (two detection and two reference channels) such that test samples and controls are run simultaneously to ensure accuracy. The optical setup of the BMD system was designed to operate at a wavelength of 1550 nm, which is a common wavelength for protein detection. Most of the components of the BMD system were commercial off-the-shelf components. Two biomarker proteins (human lipocalin-2 [NGAL] and interleukin-18 [IL-18]), which are directly related to Delayed Graft Function (DGF) following kidney transplantation,⁶⁰ were detected with high specificity (>99%) from samples in a physiological buffer (phosphate buffered saline) and in spiked porcine blood at room temperature. The results showed that the BMD provided a unique bio-monitoring platform that was capable of detecting biomarker proteins with high specificity and sensitivity, without the need for labeling or the use of expensive reagents that might require expert preparation.

BMD construction and function

The BMD sensor was fabricated by fusion splicing an 18.85cm-long termination fiber (Fitel OFS, Hampton, NJ) between two standard Single Mode Fibers (SMF-28, Corning Inc.). Since the termination fiber does not have any cladding, the aqueous buffer, which can be any fluid from phosphate buffered solution to whole human blood, functions as the cladding for the light guided into the sensor region (Figure 3.1). From the figure the sensor region is the center multimode fiber section where no cladding is present and light can escape from that region. As a result of this configuration, as the concentration of proteins that are bound to the fiber increases, correspondingly greater light intensity is able to reach the detector, generating a signal proportional to the amount of bound protein. The sensitivity of the BMD was evaluated using the design shown in Figure 3.2a. Sensitivity was measured by monitoring changes in the refractive index of the surrounding buffer medium when light at 1550 nm wavelength from a high-power (10 mW) superluminescent laser diode (DenseLight, Inc., Singapore) was split and sent

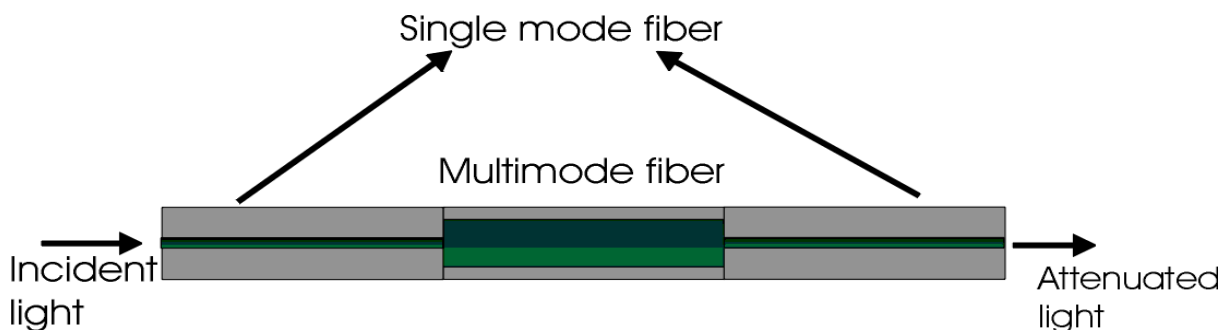


Figure 3.1. Multimode Fiber Interferometer for the BMD Sensor. The configuration consists of two single-mode silica fiber sections (8 μm core diameter, 125 μm cladding) at the ends, and a multimode fiber section (125 μm core diameter) in the middle with no cladding.

through the sensing and reference legs of the sensor, and the transmitted light signals were detected at detectors D1 and D2 (Thorlabs, Inc., Newton, NJ). To determine the refractive index sensitivity of the BMD sensor, signals at the detectors were measured simultaneously using liquids of different refractive indices. As the concentration of material increases in the liquids there are more opportunities for light to reflect off that molecule and back into the fiber at the detector (Cargille Laboratories, Cedar Grove, NJ). Each liquid can also absorb the laser light ejected from the sensory region, and this too can be an accurate measurement, because the signal to the detector would be reduced compared to the control. The measurements were conducted by surrounding the sensing channel with media of varying refractive indices (1.3 to 1.4) while the reference channel was maintained in phosphate buffered saline. The measured results are shown in Figure 3.2b.

The slope of the measured response (Figure 3.2b) is 15.44dB/unit refractive index. If the optical detector system is capable of measuring an optical loss with 0.01 dB accuracy, the sensitivity of the BMD sensor to refractive index changes will be 6.5×10^{-4} dB. This refractive index sensitivity compares well with other types of optical fiber sensors, including fiber grating sensors (Figure 3.3). While the refractive index sensitivity of the prototype sensor was in the order of 10^{-4} , it can be improved by at least an order of magnitude by optimizing the length of the multimode waveguide sensor, making it comparable to other devices on the market. With the fiber fusing and splicing process that was used to fabricate the BMD prototype sensor, it was difficult to control the length of the multimode waveguide, as the variation in the slicing process is more than one hundred micrometers, resulting in a small amount of inconsistency from one sensor to another.

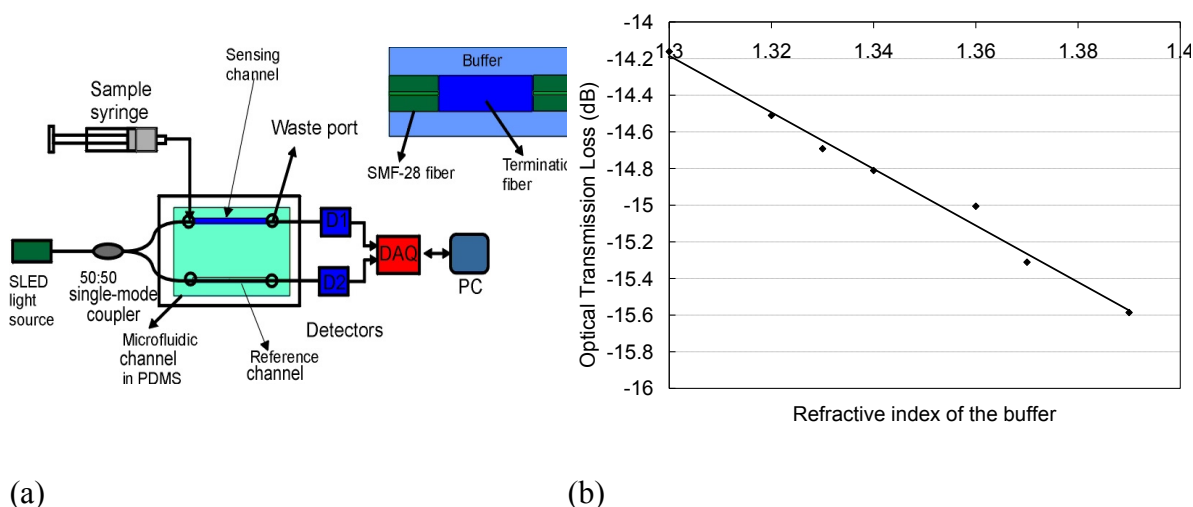
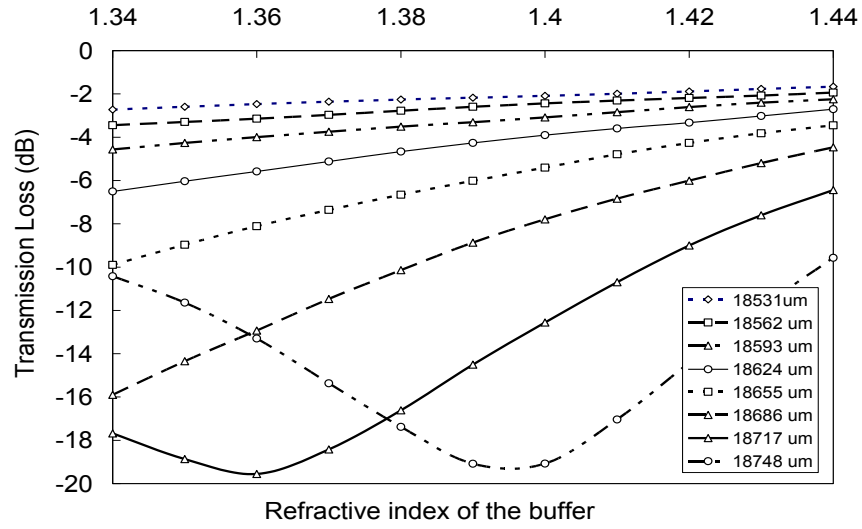


Figure 3.2. Design of a BMD Sensor. (a) BMD design for the sensor head, light source, detector, data acquisition (DAQ) system, and microfluidic device. (b) Measured optical loss using the BMD sensor as a function of the refractive index of the surrounding medium (cladding).

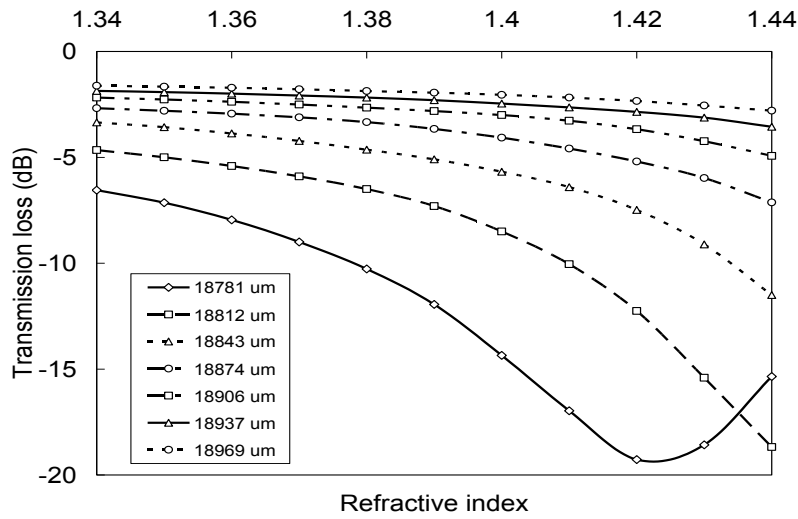
BMD applications

A. Immobilization of Antibody on Sensor Surface

Immobilization of antibodies on a glass surface using Poly-L-lysine (PLL) is reported in the literature^{62,63,64,65}. In the BMD sensor, poly-L-lysine (Sigma P8920) was used to immobilize avidin proteins (Sigma A9275) on the fiber surface as shown in Figure 3.4. Fluorescein-labeled biotin in phosphate buffered saline (PBS, Sigma, B9431)



(a)



(b)

Figure 3.3 a and b. Optical Field in the Multimode Waveguide. Optical loss as a function of refractive index of the cladding for different multimode waveguide lengths.

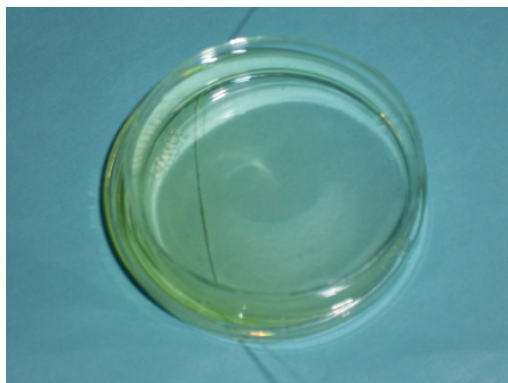


Figure. 3.4 Fiber Preparation. Immobilization of avidin on an optical fiber surface, followed by BSA as a blocking reagent.

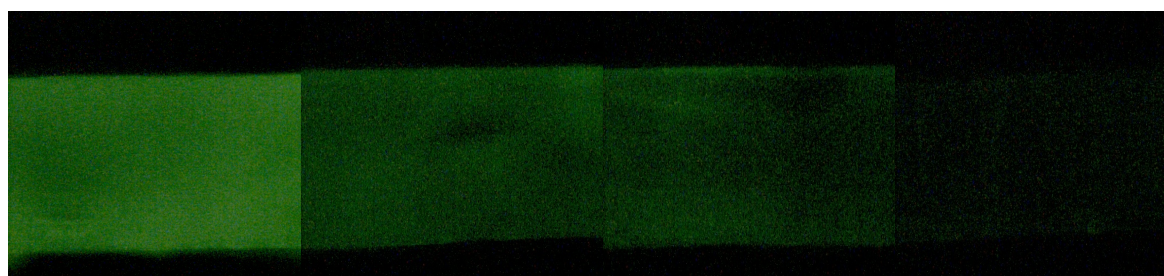
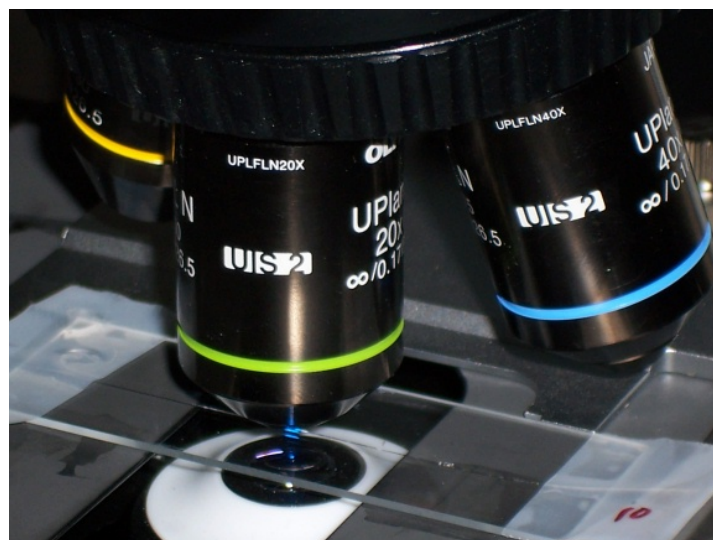
was used as the target molecule. The immobilization protocol used for this process is as follows: (1) the surface of the fiber is cleaned with a 3:1 (v/v) methanol:chloroform mixture, (2) the fiber is washed with pure (HPLC grade) methanol, (3) the fiber is rinsed in deionized water and dried in a nitrogen stream at room temperature, (4) the cleaned fiber surface is immersed in a solution containing poly-L-lysine in deionized water (0.01% w/v) for 30 minutes, (5) the Poly-L-lysine coated fibers are arranged in a vertical position to ensure that a uniform monolayer of PLL is formed on the surface, and (6) the coated fiber is dried in a temperature controlled oven at 45°C for 30 minutes. In order to get stable immobilized proteins by covalent bonding, the PLL coated fiber surface is treated with 1-ethyl-3-(3-(dimethylamino) propyl) carbodiimide (EDC) for 10 minutes. EDC surface activated fiber is immersed in a freshly prepared solution of avidin (50 mg/mL in PBS buffer, pH 7.2) and stored overnight at 4°C. After removing the fiber from the avidin solution, the fiber is rinsed in PBS buffer and the PLL surface is treated with a bovine serum albumin (BSA) solution (1 mg/mL in PBS buffer) for 15 minutes at room temperature to block any available non-avidin binding sites on the PLL coating.

Excess BSA is removed by rinsing the PLL coated fiber in PBS buffer (pH 7.2). The fiber sensor surface is ready to capture biotinylated target molecules.

The efficiency of the immobilization method was evaluated by binding five different concentrations (1, 10, 25, 50, and 100 pg/mL) of fluorescein-labeled biotin (excitation wavelength 488 nm, emission wavelength 514 nm) to five separate avidin coated PLL fibers. Each of the avidin-immobilized optical fiber waveguides was incubated in a separate fluorescein-labeled biotin sample for approximately 5 minutes. The sensor surface was washed using PBS buffer and the fluorescence images were visualized and recorded using a fluorescence microscope equipped with a CCD camera. The binding efficiency results are shown in Figure 3.5. The intensity of observed fluorescence indicates a uniform avidin/biotin binding on the waveguide surface, and the amount of binding is proportional to the biotin concentration in the sample solution. No measurable fluorescence was observed for fiber coated with the 1 pg/mL biotin sample.

B. Fabrication of the Microfluidic Chip

Master templates for the BMD MDD were fabricated in a silicon substrate using standard UV lithography with SU8 photoresist, as shown in Figure 6a. Features, such as micro-



100 pg/mL

50 pg/mL

25 pg/mL

10 pg/mL

Figure 3.5. Fluorescent Images of Fluorescein-Labeled Biotin Coated Fibers. Fluorescence images were taken from a CCD camera attached to a microscope. Different concentrations of fluorescent labeled biotin were bound to avidin molecules immobilized on the optical fiber surface. The fluorescent label was excited by 488 nm light, and the emission wavelength was 514 nm.

channels with cross-sections of 300 μm x 400 μm , were fabricated using multistep photolithography for the BMD prototype. The process flow diagram (steps a-c) and the

resulting devices are shown in Figure 3.6b. Poly(dimethylsiloxane) (PDMS) MDDs were fabricated by a simple molding and lift-off process.

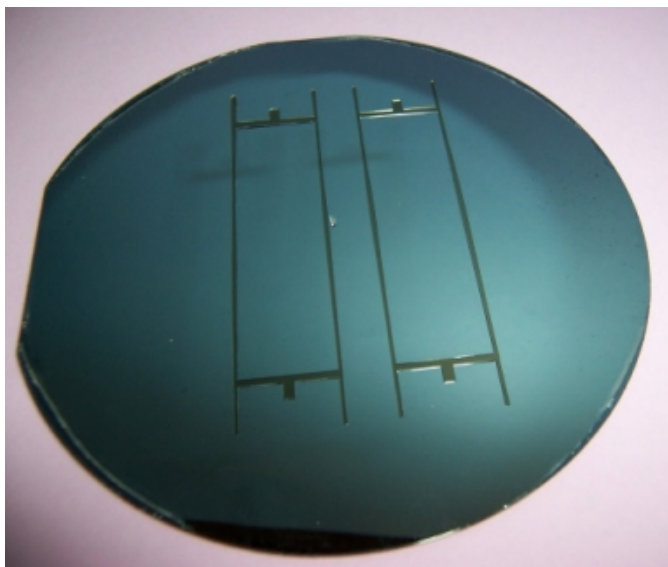


Figure. 3.6a. A Microfluidic Template. Master template fabricated by SU8 lithography on a silicon substrate.

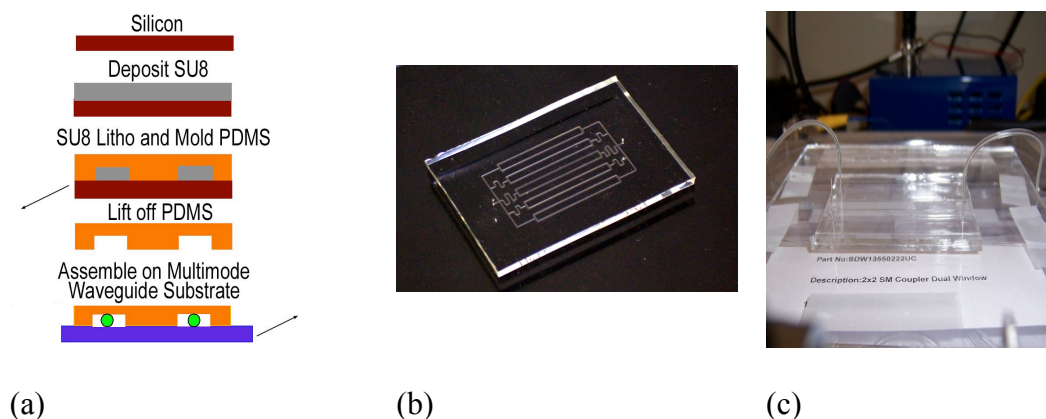


Figure 3.6b. PDMS Mold Fabrication. (a) The fabrication process flow, showing the molding steps to obtain a PDMS MDD; (b) a fabricated microfluidic device, and (c) microfluidic device with fluidic interconnects.

Access to the fluidic channels was produced by mechanically drilling 300 μm holes in the molded PDMS. Platinum ferrules were inserted into these drilled holes and a syringe was attached to the inlet port ferrule via a flexible tube for assaying sample buffers. Laying the multimode waveguides on a cleaned glass plate and sealing them with the PDMS MDD, as shown in Figure 3.6(c), completed sensor assembly.

C. Investigation of Avidin/Biotin Binding on the Sensor Surface

Experiments were conducted with a prototype sensor to detect unlabeled biotin using the same immobilization method described above. The experimental setup is identical to the one shown in Figure 3.3, with the exception that the MDD had common inlet and outlet points for the sample buffer flow. Avidin was immobilized on the sensing arm of the sensor before the fiber waveguides were assembled within the microfluidic

channels. Transmitted light signals from the sensing and reference fiber legs were recorded. Initially, both channels of the sensor were filled with PBS buffer to collect the background signal. Four different sample solutions, each with different amounts of biotin in 50, 100 and 500 pg, and 1 ng in 100 μ l volumes, were prepared for the experiment. First, a sample with the lowest concentration was pumped into the microfluidic channels and the detector signals were recorded immediately after the pumping had stopped. During the pumping of samples, the detector signal showed several spikes due to the mechanical disturbances induced by the flow pressure on the sensor elements. To reconstitute the sensor surface after each experiment, the sensor waveguides were flushed with freshly prepared 0.1 M glycine (pH 2.0) in PBS buffer for 2-5 minutes, followed by three flushes with PBS buffer (pH 7.2). The test results are shown in Figure 3.7.

The results show a clear difference in the detected signal level for the different concentrations of biotin in the sample buffer. However, the prototype sensor did not show a linear response with the concentration of the target molecules below 200 pg/mL. Variation in waveguide sensor length during the sensor fabrication process is believed to have contributed to this non-linearity. The large standard deviations in the sensor signal can be attributed to the loss of activity of the sensor surface during the repeated regenerative processes, as observed in Figure 3.8.

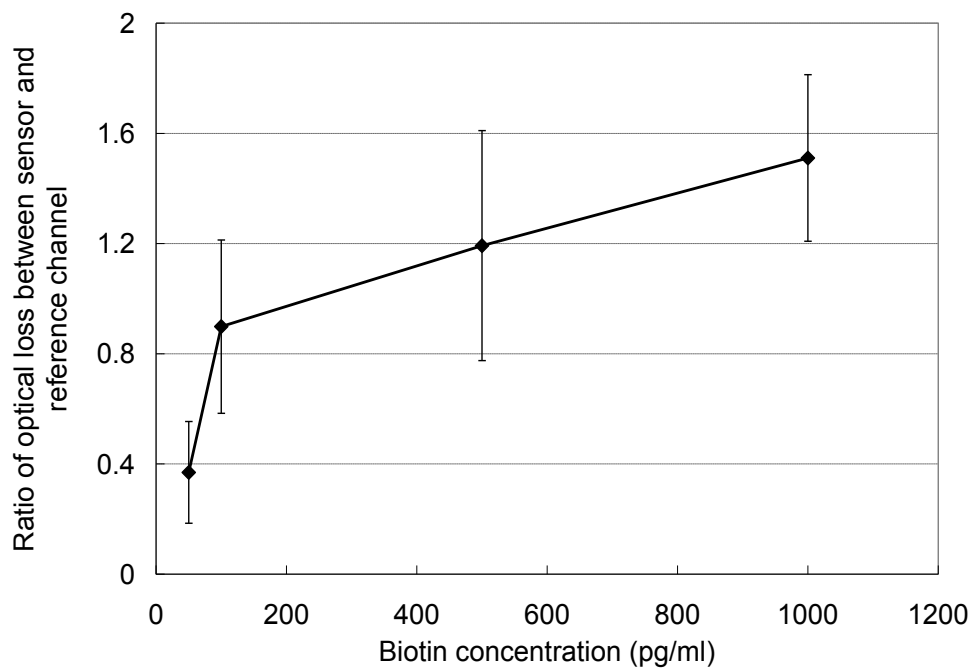
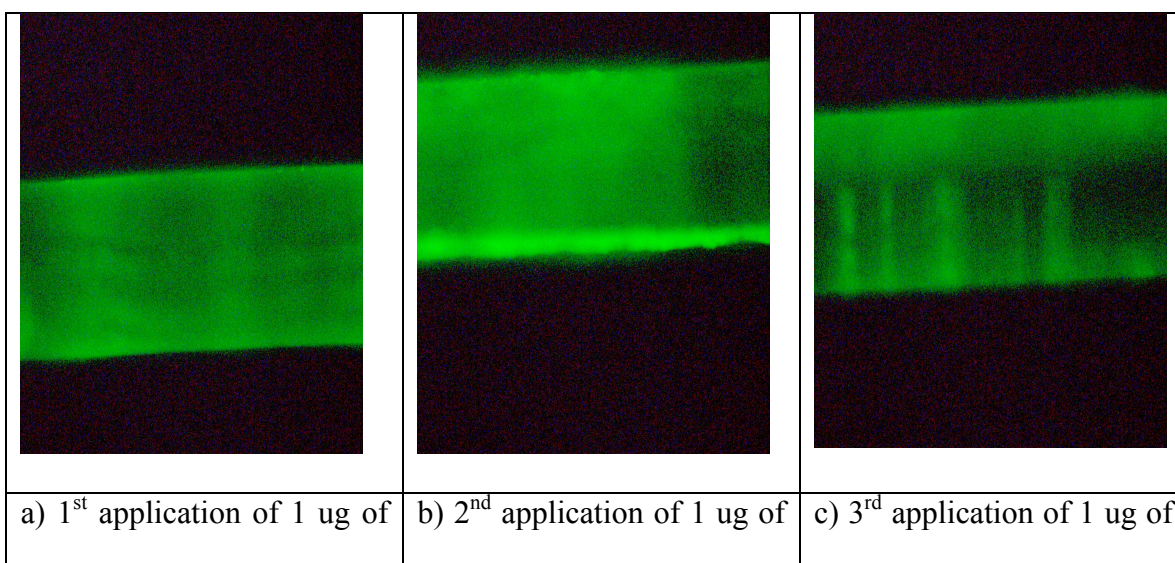


Figure 3.7. Optical Loss of Biotin. Experimental results from the BMD prototype sensor when different concentrations of biotin solutions were used in the detection channel. Each test point represents the mean and standard deviation of three test results.



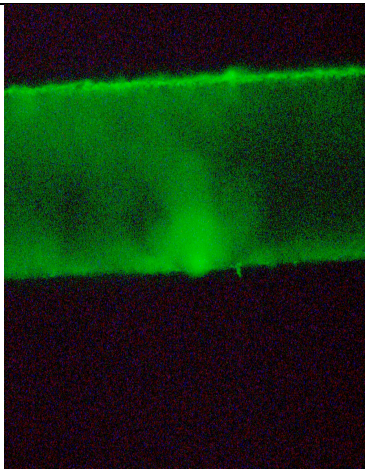
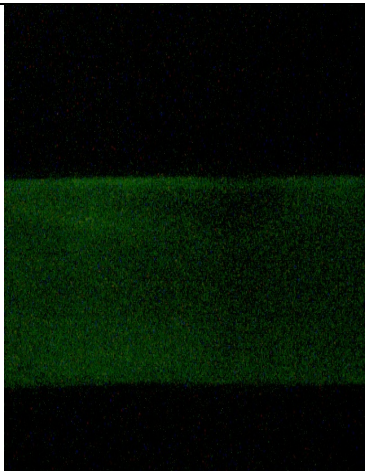
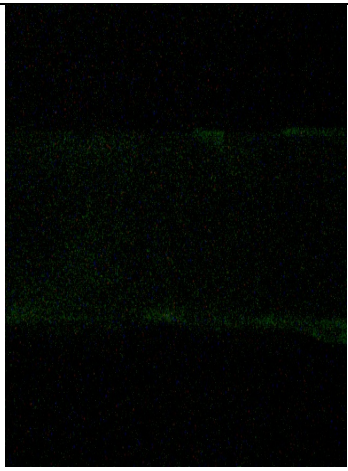
Biotin	Biotin	Biotin
		
d) 4 th application of 1 ug of Biotin	e) 5 th application of 1 ug of Biotin	f) 6 th application of 1 ug of Biotin

Figure 3.8. Successive Regeneration of Biotin on a Avidin Coated Fiber Optic Cable. Avidin coated fibers were treated with labeled biotin then washed with pH 2.0 glycine.

The fluorescent intensity, as detailed in Figure 3.8, is high during first and second applications. Since there is only one fluorescent marker on each biotin molecule this suggest that a high concentration of biotin attached to the avidin coated fiber, but after every successive wash application (a pH 2.0 glycine wash for 5 minutes) to clean the fiber surface from bound biotin, it becomes clear, especially after the third wash, that the levels of fluorescent intensity have decreased and specific segments of the fiber are much lower in intensity than other regions. By the fifth application the overall fluorescent intensity is dramatically lower than the intensity of the initial application. By the sixth application the amount of florescent label present is nearly negligible when compared to the first three applications of biotin.

Biomarker detection results

Experiments were performed to evaluate the capability of the BMD to detect two biomarkers separately, as well as simultaneously. The experimental setup, shown in Figure 3.9, was used for evaluating the BMD to resolve biomarker specificity. The biomarkers, human lipocalin-2 (NGAL, MW 25kDa) and interleukin-18 (IL-18, MW 44kDa), and their biotinylated antibodies were purchased from R&D Systems, Inc. (Minneapolis, MN). The experimental set up consisted of four channels, two detection channels (AB1 and AB2) and two reference channels (R1 and R2). Each channel had a separate optical detector. Light from the superluminescent light emitting diode (SLED) was split into four different optical fiber channels using a 1'4 waveguide splitter and sent to the detectors via the BMD sensor channels. Waveguide sensor surfaces were immobilized with avidin as described previously. After treatment with a solution containing 3% BSA protein, sensor waveguide AB1 was immersed inside a sample buffer containing 10 ng/mL of biotinylated anti-lipocalin antibody, while sensor waveguide AB2 was immersed inside a sample buffer containing 10 ng/mL of biotinylated anti-interleukin antibody. The reference sensor waveguides, R1 and R2, were kept in phosphate buffered saline (pH 7.2) during this process. All waveguides (detection and reference waveguides) were laid on a clean glass plate for 25 minutes and a PDMS microfluidic chip was aligned and sealed on top of the fiber waveguides. The microfluidic chip had one common entry and exit point for injecting fluid samples in and out of the channels.

Three different sample solutions were prepared from the two biomarkers as follows:

Sample 1. 36 pmol NGAL-2 in Tris-HCl buffer (pH = 8.0).

Sample 2. 0.22 nanomol IL-18 in Tris-HCl buffer (pH = 8.0).

Sample 3. Mixture of Sample 1 and Sample 2 at 1:1 (v/v).

Four different tests, as described below, were designed to demonstrate the specificity of the BMD to resolve and identify each biomarker.

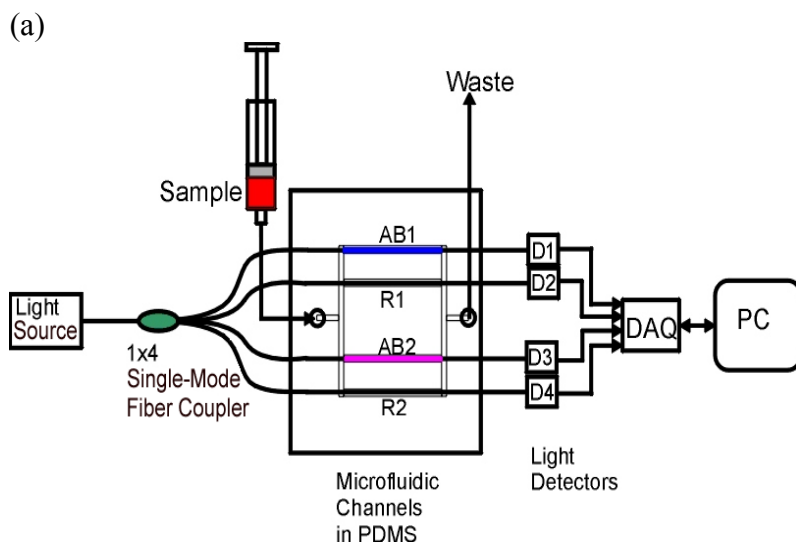
Test 1: No biomarker sample is injected into the microfluidic channels.

Test 2: 100 μ L of Sample 1 is injected into the microfluidic channels.

Test 3: 100 μ L of Sample 2 is injected into the microfluidic channels.

Test 4: 100 μ L of Sample 3 is injected into the microfluidic channels.

During Test 1, all the microfluidic channels contained Tris-HCl buffer (pH 8.0). Each subsequent test (Test 2 through Test 4) was performed using 100 μ L of sample injected into the microfluidic channels using a glass syringe. The sensor system was cleaned after each test using 0.1 M glycine (pH 2.0) followed by rinsing with 0.1 M PBS (pH 7.2). Each sample was carefully injected to minimize mechanical disturbances inside the microfluidic channels. The system was left undisturbed for 2 minutes before the SLED light source was turned on, and the data from the photoreceiver array were continuously recorded for 10 minutes during each test. The test results are shown in Figure 3.10.



(b)



Figure 3.9. Biomarker Monitoring Device Prototype. (a) Schematic of the BMD setup for simultaneously detecting two biomarkers: AB1 = detection channel 1; AB2 = detection channel 2; R1 = reference channel 1; R2 = reference channel 2, D1..D4 = optical detectors, and (b) the experimental setup.

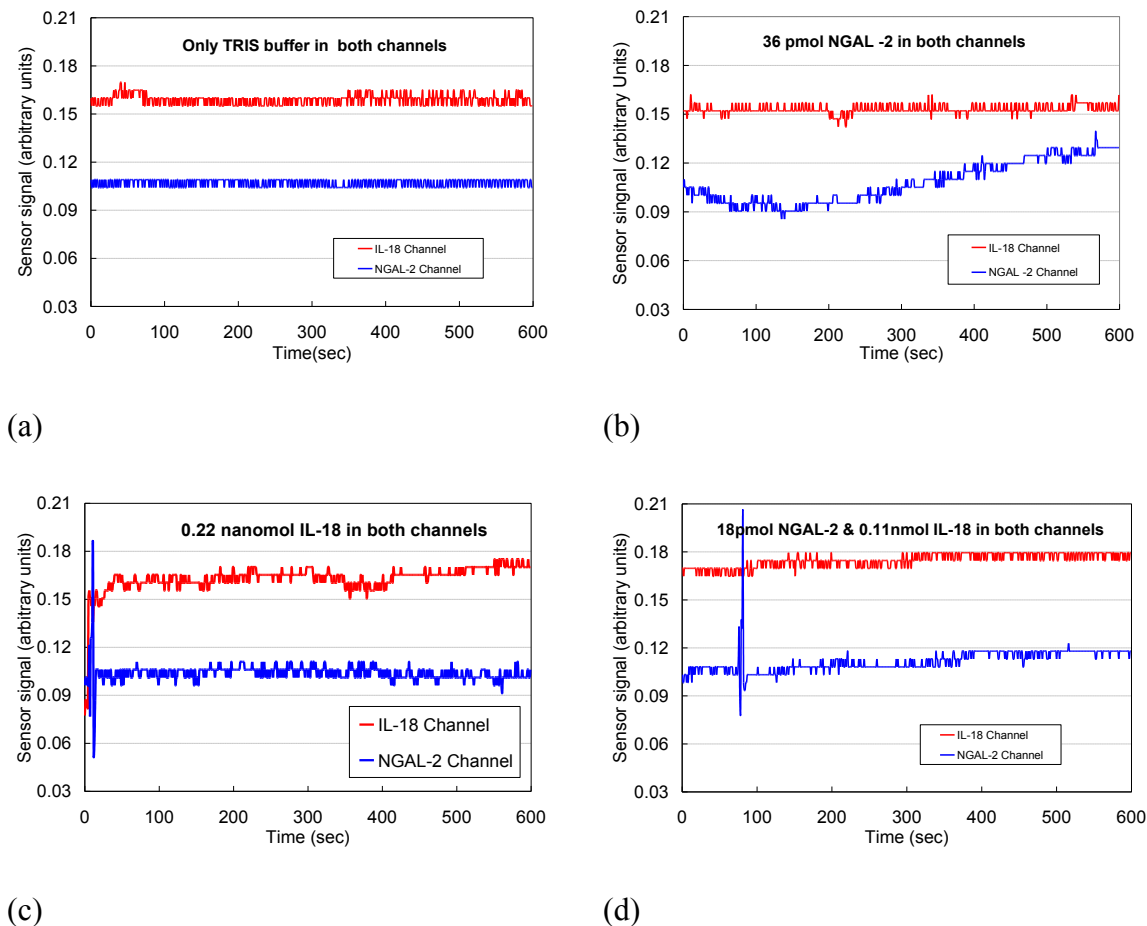


Figure 3.10. BMD Sensory Data. Experimental results for all microfluidic channels in the BMD when filled with (a) PBS buffer (pH 8.0), showing no response in any channel; (b) Sample 1, showing a response only in channel AB1; (c) Sample 2, showing a response only in channel AB2; and (d) Sample 3, showing a response in both channels.

The experimental results show that the BMD sensor channels immobilized with different antibodies respond to only the specific biomarker of interest. No cross-sensitivity between the two tested biomarkers was noticed during repeated experiments. It was observed that the sensitivity of the sensor response continuously decreased with the number of repeated tests due to a loss of activity on the sensor surface. However, the

sensitivity was sufficiently high for the BMD to detect the presence of the biomarkers after four regeneration process steps. It should be noted that the concentration of NGAL and IL-18 biomarkers in Test 4 was 50% lower than the concentrations used in Test 2 and Test 3. These results demonstrate that the BMD is capable of specifically resolving the tested biomarkers.

A series of experiments were also performed to investigate the sensor response when the biomarker proteins are contained within a whole blood matrix. Porcine blood at room temperature was mixed with the same biomarkers as identified previously. However, the biomarker sample solutions were prepared at a concentration of 100 ng/mL in PBS buffer (pH 7.2). The solutions were then mixed with the porcine blood in a 1:5 ratio, resulting in a final concentration of 20 ng/mL. The test method was identical to that described previously with the exception that porcine blood was substituted for Tris Buffer. First, the microfluidic channels were filled with porcine blood to record the baseline reading. The sample solution containing both biomarkers in spiked porcine blood was injected into the sensor system and the signal was recorded (Figure 3.11).

The data demonstrate that a difference in signal level is clearly distinguishable when there is whole blood in the channel and when the biomarkers are present in the blood sample. It should be noted that the rate of change in the sensor signal for the IL-18 biomarker is smaller than that of the NGAL biomarker, which is consistent with the

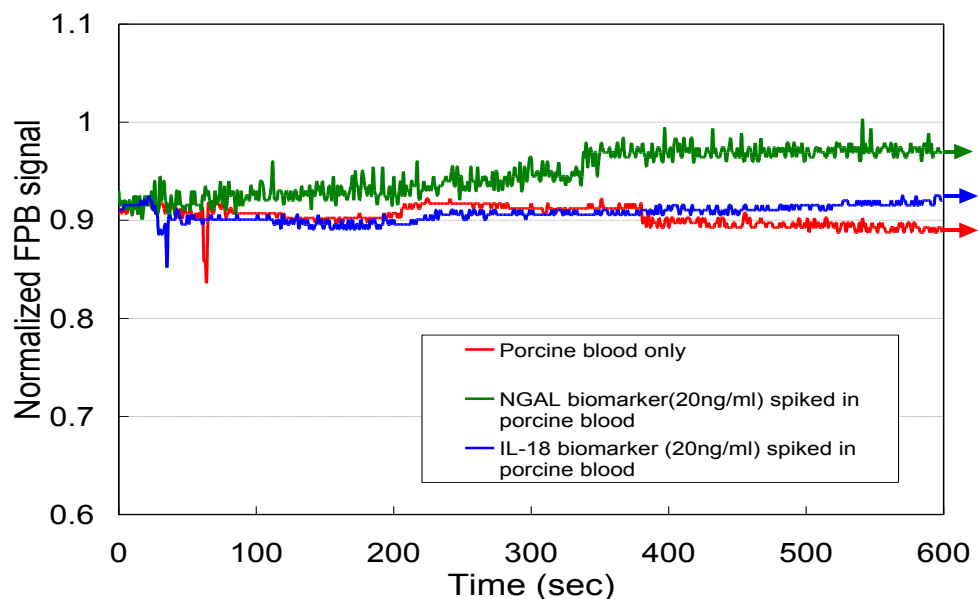


Figure 3.11. BMD Sensory Data of Biomarkers Spiked into Whole Porcine Blood.

previous tests performed with biomarkers present in PBS buffer. Depending upon the binding rate and the affinity of the antibodies for the biomarker, some biomarker proteins may require more than ten minutes of incubation time to induce a change in the refractive index so that the optical signal can be distinguished from its baseline value.

Conclusion

The feasibility of a new optical sensor, based upon optical loss in single mode to multimode light guiding properties of waveguides, to simultaneously detect at least two biomarkers at picomolar concentrations with nearly 100% specificity was demonstrated. The BMD prototype detected two different biomarkers, human lipocalin-2 and recombinant human interleukin-18, at nanogram/mL concentrations using less than 100 mL of sample. This sample volume represents a significant decrease in sample volume

from any commercially available instrument on the market today. The test data also demonstrated that the sensor element of the BMD (uncladded fiber optic cable covered in a specific protein) could be reused by a simple regenerative process that removes all of the biological matter for replacement with another protein. Although it is not clear if the reduction of signal is the result of degrading the avidin protein on the fiber, or the stripping of the poly-l-lysine from the fiber surface, for either case the optical fiber can be re-prepared with more poly-l-lysine solution with added desired protein to create a new active biosensor. The BMD prototype test system was designed to simultaneously evaluate two biomarkers. However, many more biomarkers can be simultaneously evaluated because the only limiting factor is the number of fiber optic cables that can be linked together and thus the power to send concentrations of light through the system. This new sensor system represents the promise of a smaller, faster, and more easily handled hand-held biomarker monitoring device for point-of-care applications than any current existing sensor systems. The BMD allows for fast, on-the-spot data collection, eliminating the time required to transport either a sample or a person to the test site to analyze the data.

Chapter 4

Generation of Microchannels in Silicon on Insulator Wafers

Introduction

Microfluidic devices for all their convenience have not had the vast impact on science and creating portable laboratories as many have hoped; this is the unfortunate result of needing large equipment to run these small devices. The reaction chambers and reagents required are small, but many fluidic devices require valves, pumps, and detection equipment that turn these tiny devices into a large complex network of instruments. The Axel Scherer lab has strived to turn microfluidics back into the intended purpose; small integrated devices in which all of the detection and controls are self-contained in the device. The first step in the integration process is to use materials that can both handle the biological or chemical samples being analyzed and can also be used for mechanical and electrical components needed to accomplish these tasks^{66, 70}. We can limit our search for new materials by looking for some key properties: a material should be relatively chemically inert and optically transparent, and be able to handle pressure and ideally have some electrical properties; one such material is silicon on insulator (SOI) wafers^{66,70,71}.

SOI wafers are composed of a three layer material stack of the following: an active layer of prime quality silicon (DEVICE LAYER) over a buried layer (BOX) of electrically insulating silicon dioxide over a bulk silicon support wafer (HANDLE), as shown in Figure 4.1. In electrical engineering SOI are replacing bulk silicon wafers (approximately 0.75 mm thick) with wafers that have three layers: a thin surface layer of silicon (from a few hundred Angstrom to several microns thick) where the transistors are

formed, an underlying layer of insulating material, and a support or "handle" silicon wafer. The insulating layer, usually made of silicon dioxide and referred to as the "buried oxide" or "BOX", is usually a few thousand Angstroms thick, but can be several microns thick. When transistors are built within the thin top silicon layer, they switch signals faster, run at lower voltages, and are much less vulnerable to signal noise from background cosmic ray particles. Since on an SOI wafer each transistor is isolated from its neighbor by a complete layer of silicon dioxide, they are immune to "latch-up" problems and can be spaced closer together than transistors built on bulk silicon wafers. Building circuits on SOI allows for more compact chip designs, resulting in smaller IC devices (with higher production yield) and more chips per wafer (increasing fab productivity).

Since SOIs are already used in the fabrication of transistors, is it possible to use this material for other purposes. By exploiting the buried oxide layer of SOI and the fact that we can selectively etch different materials, is it possible to generate a channel inside an SOI without significant damage to the top layer of silicon, and if this can be accomplished, what properties does this new type of device have that can be beneficial to generating an integrated fluidic device?

Device Fabrication

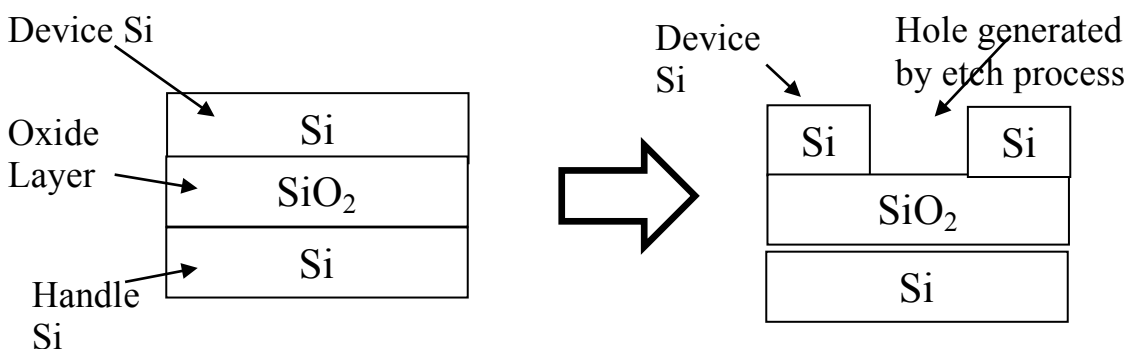


FIG. 4.1A

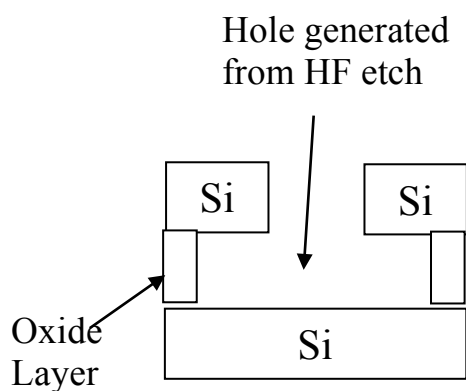


FIG. 4.1B

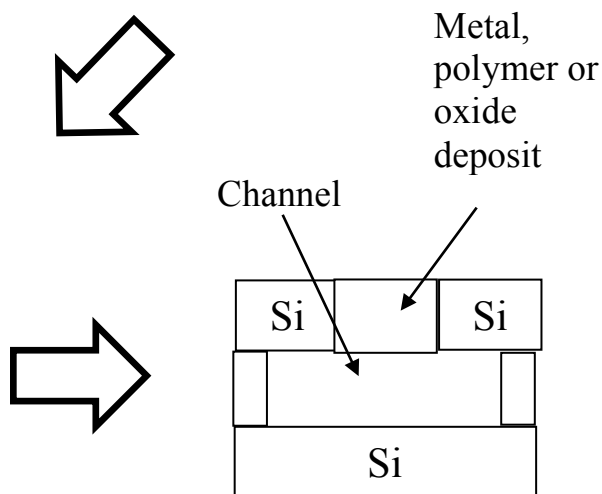


FIG. 4.1C

FIG. 4.1D

Figure 4.1A, B, C and D. Outline of the SOI channel fabrication process. Schematic representation of the process that develops fluidic channels inside the oxide layer of silicon on insulator wafers.

A. Wafer Thinning

1. Chemical Mechanical polishing

A wafer was sent out to Aptek Industries, Inc. for their chemical mechanical polishing procedure.

2. KOH etching

1. Place chip in beaker of $\text{NH}_4\text{OH}:\text{H}_2\text{O}_2:\text{DI water}$ (1:1:40) for 3 minutes at room temperature (1a). Blow dry.

2. Rinse with $\text{HCL}:\text{H}_2\text{O}_2:\text{DI water}$ (1:1:40) for 3 minutes at room temperature.

3. Blow dry.
4. Spin apply PSB primer at 2000 rpm with 500rpm/s ramp for 60 seconds.
5. Soft bake at 110°C for 1 minute .
6. Hard bake at 220°C for 5 minutes.
7. Spin apply ProTEK PSB coating at 2000 rpm with 500rpm/s ramp for 60 seconds.
8. Soft bake at 110°C for 2 minutes.
9. Expose using 365nm (i-line or Suss Channel 1) for 40 seconds.
10. Post-exposure bake at 110°C for 2minutes.
11. Develop chip in Ethyl Lactate for 10 seconds.
12. Blow Dry.
13. Repeat steps 11-12 until fully developed.
14. Hard Bake at 200°C for 3 minutes.
15. Perform undercut in KOH or TMAH. (at 2.5hrs of 75°C KOH that I get an undercut of ~120microns. This is significantly increased at KOH temperatures above 80°C.)
16. Rinse with IPA or water.

17. Remove PSB protective coating with Piranha.

B. Mask development

1. Clean wafer with IPA and water.
2. Spin desired photoresist.
3. Expose wafer with e-beam or UV light in desired pattern.
4. Develop resist.

C. Pseudo Bosch etch

1. SF₆ etch gas while simultaneously passivated with C₄F₈.

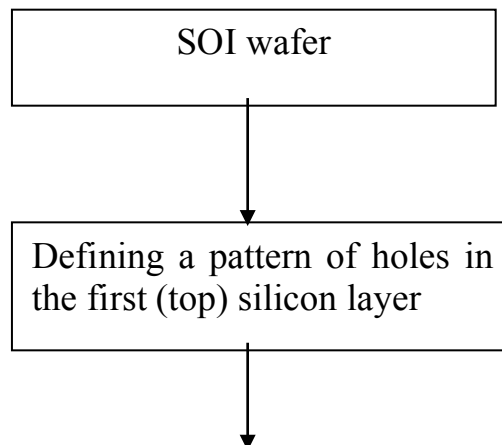
D. Channel Etching

1. Submerge wafer in HF bath.
2. After desired etch time excessively wash wafer in DI water.
3. Bake wafer for 2 hours at 150°C.

E. Channel Sealing

1. Grow a layer of oxide which will seal the etch hole, or
2. Deposit metal on the wafer, which will fill the etch hole, or
3. Spin coat a polymer layer and heat cure to fill holes.

Test Device



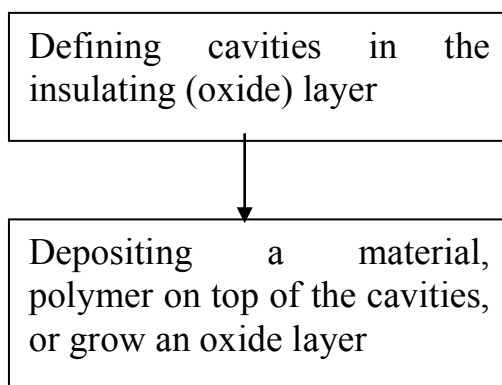


Figure 4.2 Procedural Outline for SOI fabrication. Outline of the pattern order for the generation of SOI fluidics.

Developing a new fluidic device

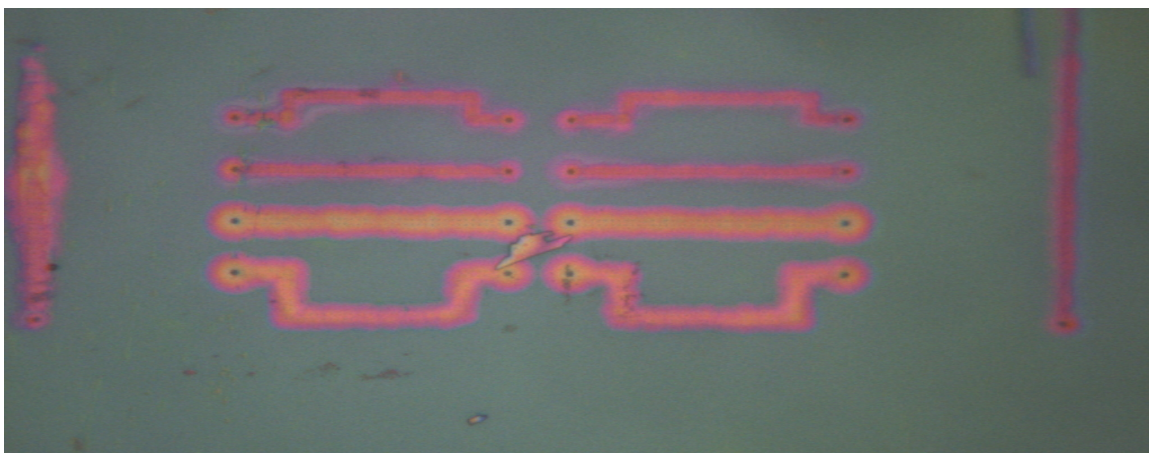


Figure 4.3 First Attempts at Generating Channels Inside an SOI Device. Proof of concept test to determine if it is even possible to generate channels in a SOI device.

There is no guarantee that an idea will be feasible even when the science behind the idea is sound. In Figure 4.3, which is a simple light microscope image through the top layer silicon, to observe the developed channels reveals one of the benefits of using SOI's, silicon is optically transparent. I attempted to generate simple pattern channels inside SOI devices of straight lines and bends, using e-beam lithography; the holes were

500nm sample holes and 50nm bulk channel holes. The procedure was not optimized, but even without optimization it was possible to generate channels. The SOI wafer use had a top silicon thickness of 400nm and an oxide layer of 2 μ m.

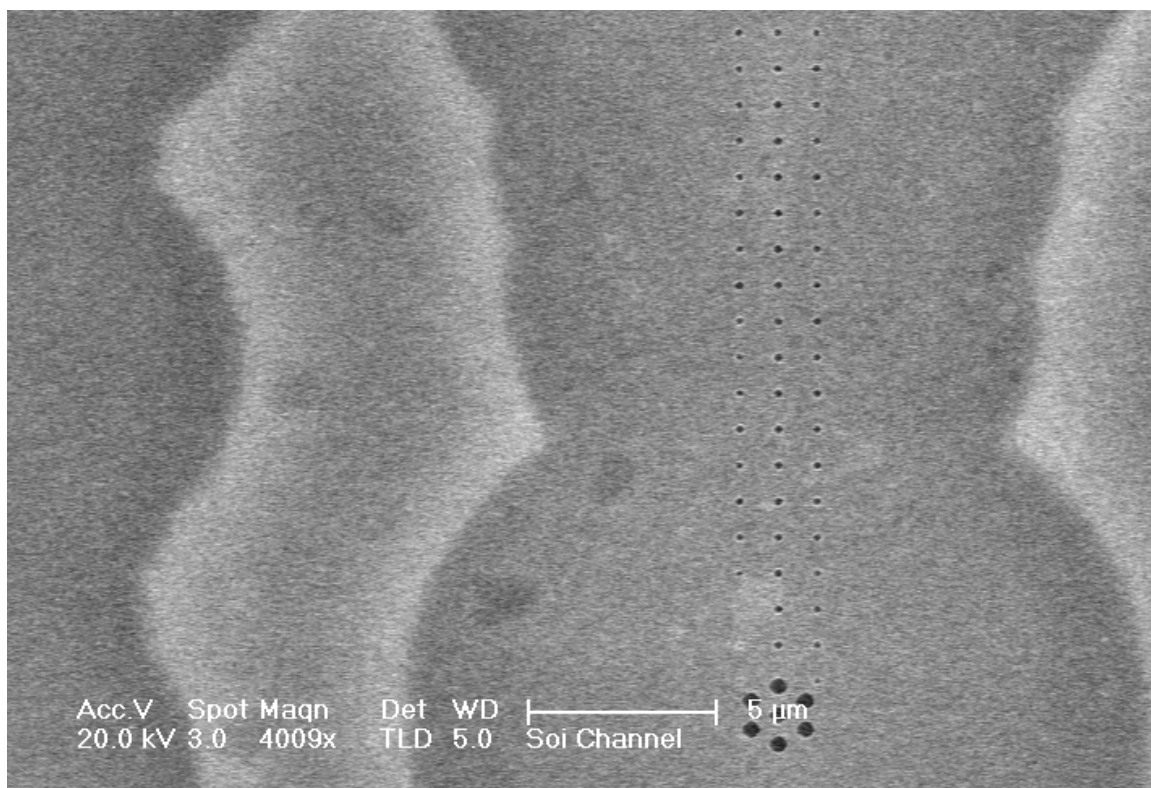


Figure 4.4 SEM Image of HF Generated Channel and Oxide Between the Two Channels.

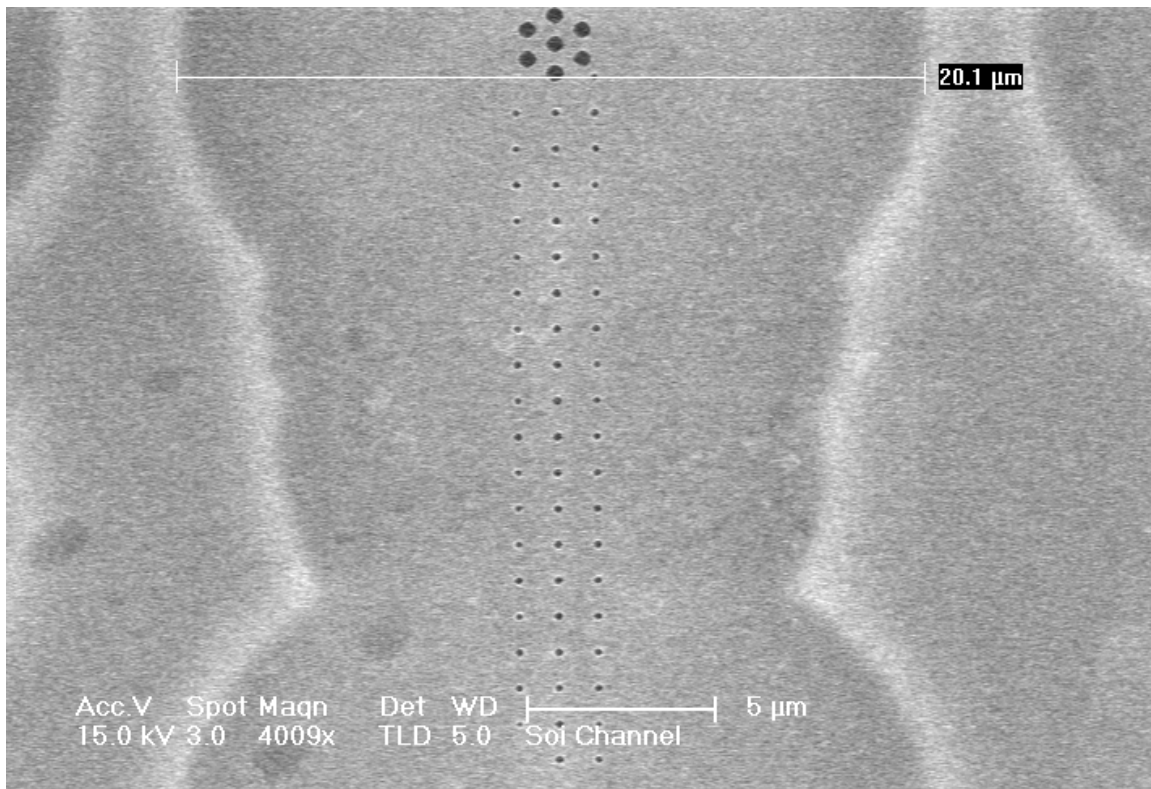


Figure 4.5 SEM Image of Channels Inside SOI Device. SEM image of first generation SOI channels displaying channel etch inconsistency.

By closely examining the device in Figure 4.5 using an SEM we can observe that the HF etch process is not uniform along the channel; as expected the channel is significantly larger in the proximity of the larger holes in the top layer silicon, yet the channel around the smaller holes should be more uniform, but this is not the case. Where the larger holes generate a channel around 20μm in diameter at its narrowest the smaller holes only generate a channel that is 10μm. To understand why this occurs, the magnification needs to be increased to have a closer look at the holes that have been etched in the silicon. There is a relationship between the hole size and channel diameter, where the larger the hole size will generate a larger channel in the SOI wafer, yet this relationship is not clearly observed in Figure 4.4.

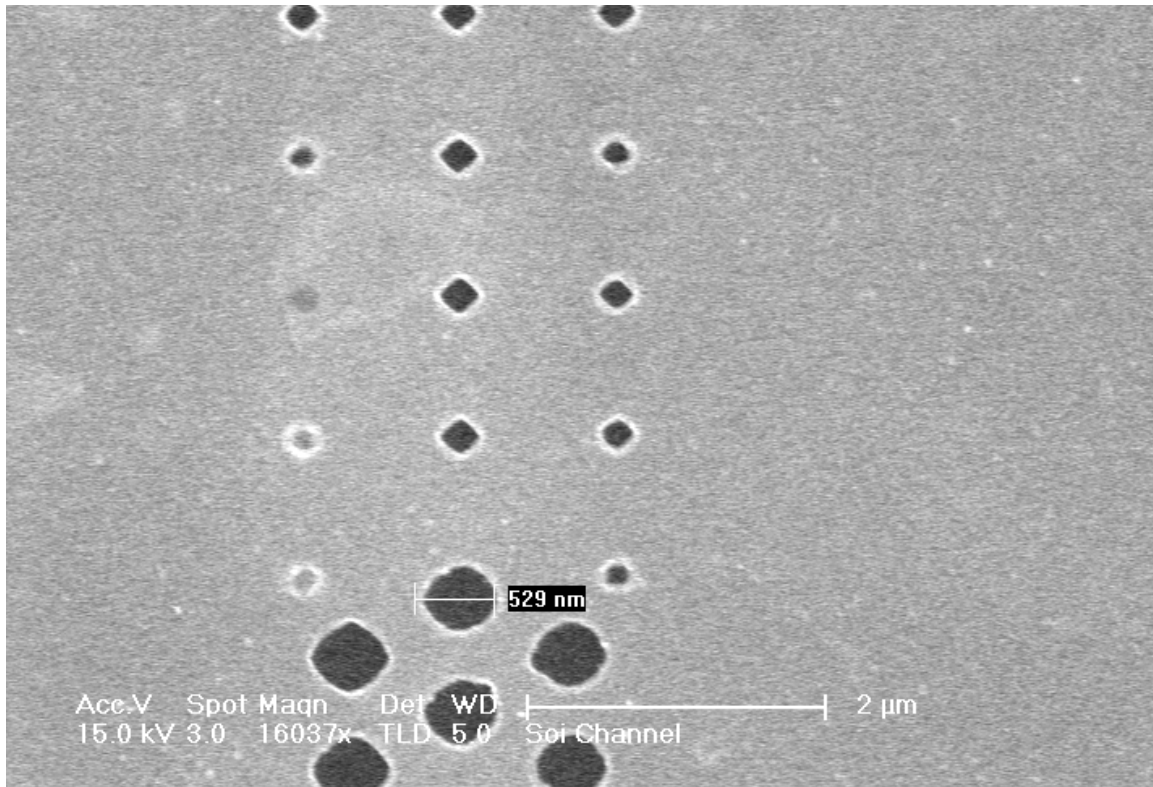


Figure 4.6 Closer SEM of First Generation SOI Channels. Increased magnification of SOI etch holes.

To understand why the oxides etch is not uniform over the channel, a closer examination of the HF access holes is needed. The etch process for the SOI channels is diffusion mediated, and the HF needs to move into the SOI to interact with the oxide and generate water and SiF_2 , which needs to diffuse out of the newly formed channel. As we can conclude, diffusion is the process that allows for the etch chemical to reach its target, and the larger the access hole, the higher the diffusion rate. As displayed in Figure 4.6, we can see different access hole and from the image we can observe that not only are the smaller holes not completely uniform, but many appear to be obstructed. From the initial trial we can see that it is possible to generate channels in the oxide layer of SOI, but the system needs optimization.

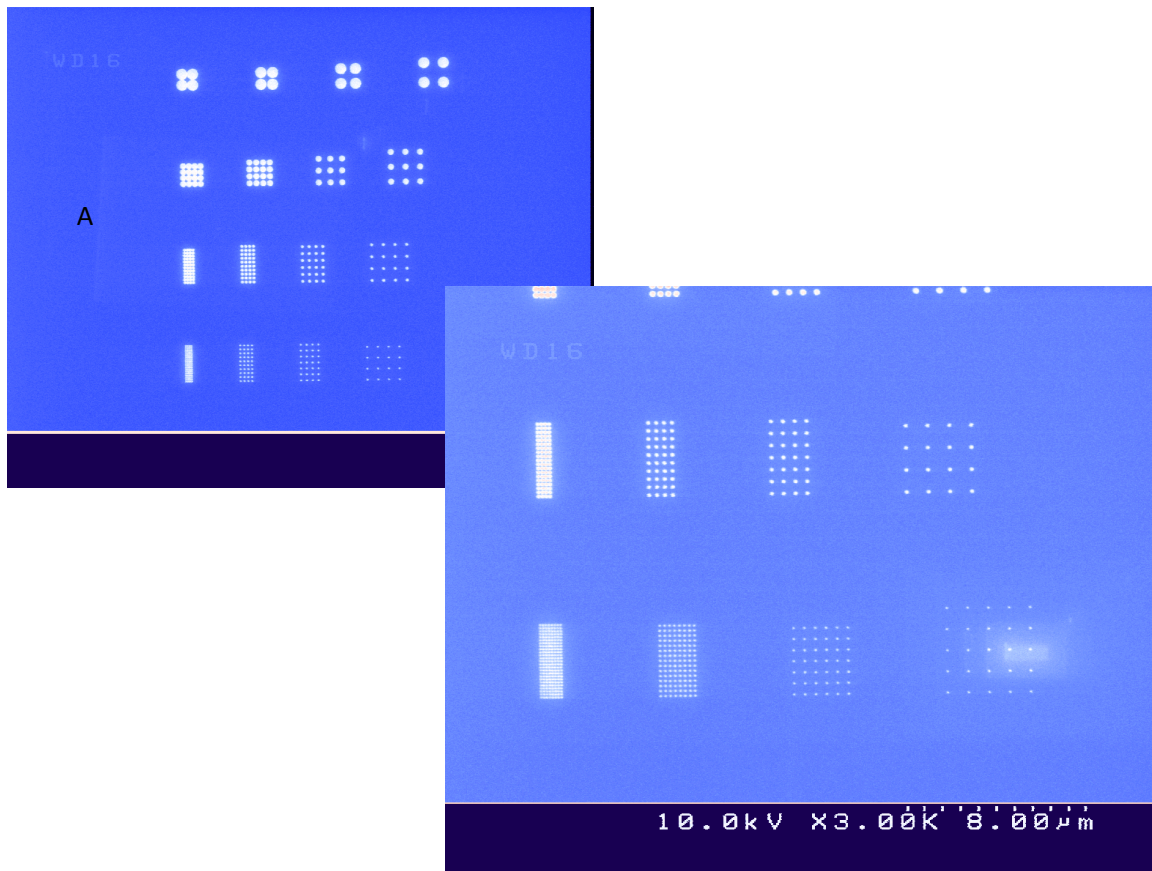


Figure 4.7 System for SOI Parameter Optimization. Auto Cad design and e-beam test pattern to optimize parameter.

There are three major variables that need to be optimized to help generate better channels from the initial trial; one being hole size, the second being hole spacing and the third is the e-beam dosage to generate the holes. Once the hole parameters are optimized channel etch times would also need its own optimization later in the process. To test these parameters simultaneously I generated a patterns (seen in figure 4.7) to test for the ideal hole size and spacing array to test different e-beam dosage. The hole size ranged from 25nm to 1μm and hole spacing from 100nm to 5μm, as seen in Figure 4.8.

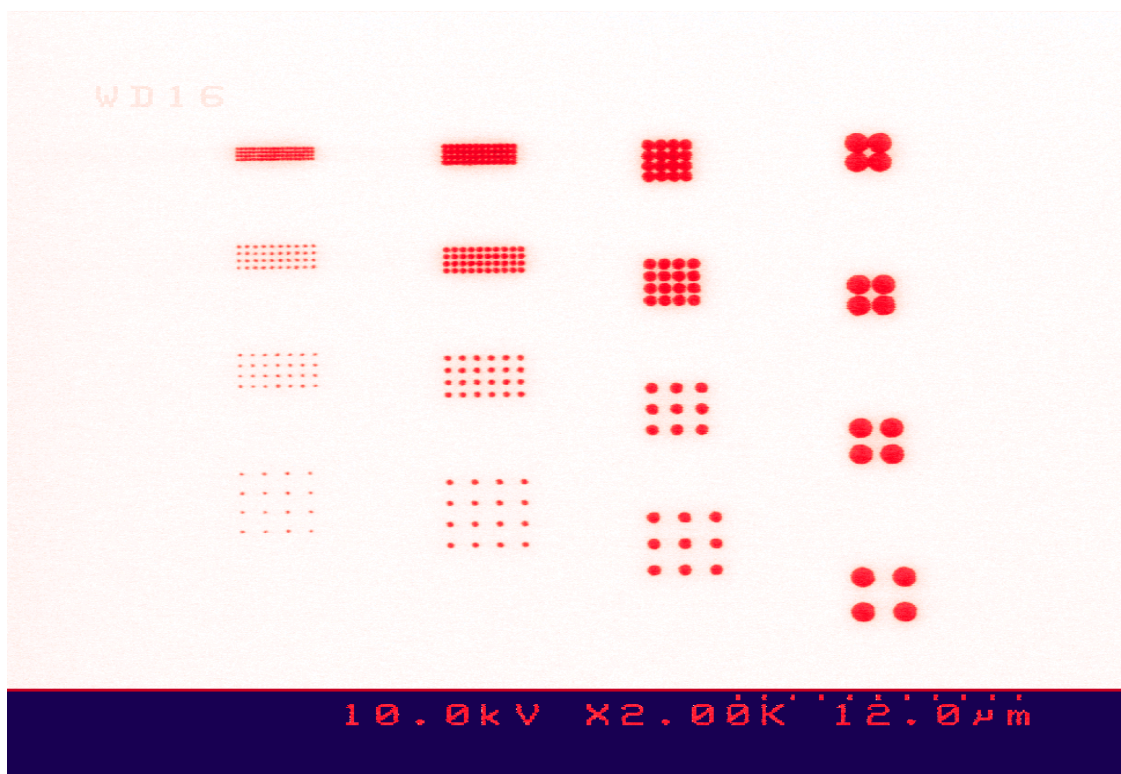


Figure 4.8 E-beam Writing of Optimization Patterns. One single copy of an array to test e-beam dosage and hole geometry for channel development.

The e-beam dosage helps to define the features in the photoactive polymer applied to the surface of the wafer; if the dose is too low the feature edges will be misshapen or will not develop properly, overexposure of the photo polymer will lead to significant morphological damage and misshapen features. As a result there is a balance between getting the correct dosage to define the features without overexposing and damaging the resist. There is also an inverse correlation between feature size and e-beam dosage. The larger features require a lower dosage and smaller features require a higher dosage. The dosage testing is displayed in Figure 4.9, where the small feature dosage is written first, followed by the large feature dosage, where a small feature is any feature below 50nm and the large feature is greater than 50nm.

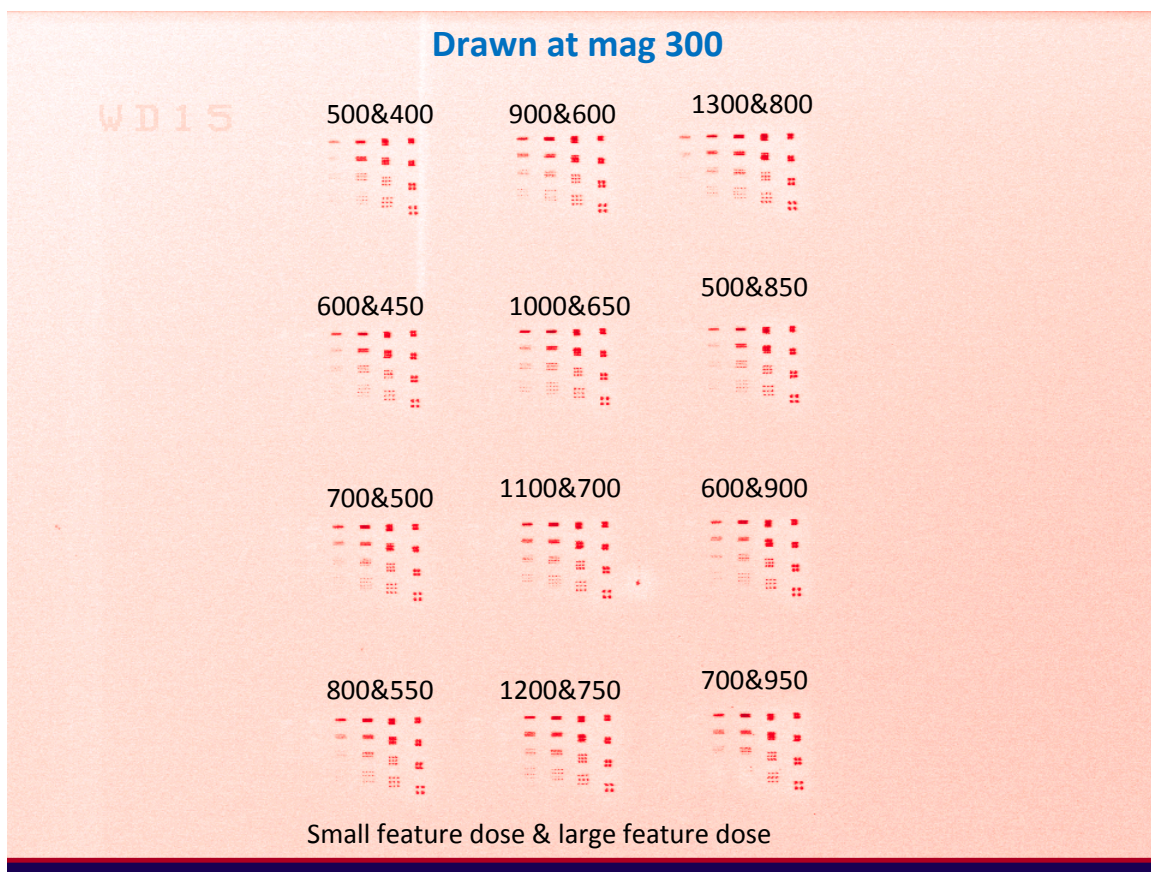


Figure 4.9. Test Array for E-Beam Optimization.

After several trials it was determined that for large features (100nm to 1µm) an e-beam dosage of 300-400 $\mu\text{C}/\text{cm}^2$ is needed, for middle range features (50nm to 100nm) an e-beam dosage around 1000 $\mu\text{C}/\text{cm}^2$ is needed, and anything smaller than 50nm needs dosages greater than 1300 $\mu\text{C}/\text{cm}^2$. Figure 4.10 shows the importance of e-beam dosage to generate uniform holes. The dosage used was 1000 $\mu\text{C}/\text{cm}^2$ and we can see the larger holes on the right have distorted edges, which results in overexposure, we can also observe the holes blend together when the hole spacing is too small. We get the opposite effect when the features are too small on the left side of the image. The holes are barely visible, which was due to underexposing the polymer; these features can be lost without proper development, resulting in the loss of the pattern in the next step of the

process. The features in the bottom center of the pattern are well defined, uniform, and clear, which will generate a clean etch.

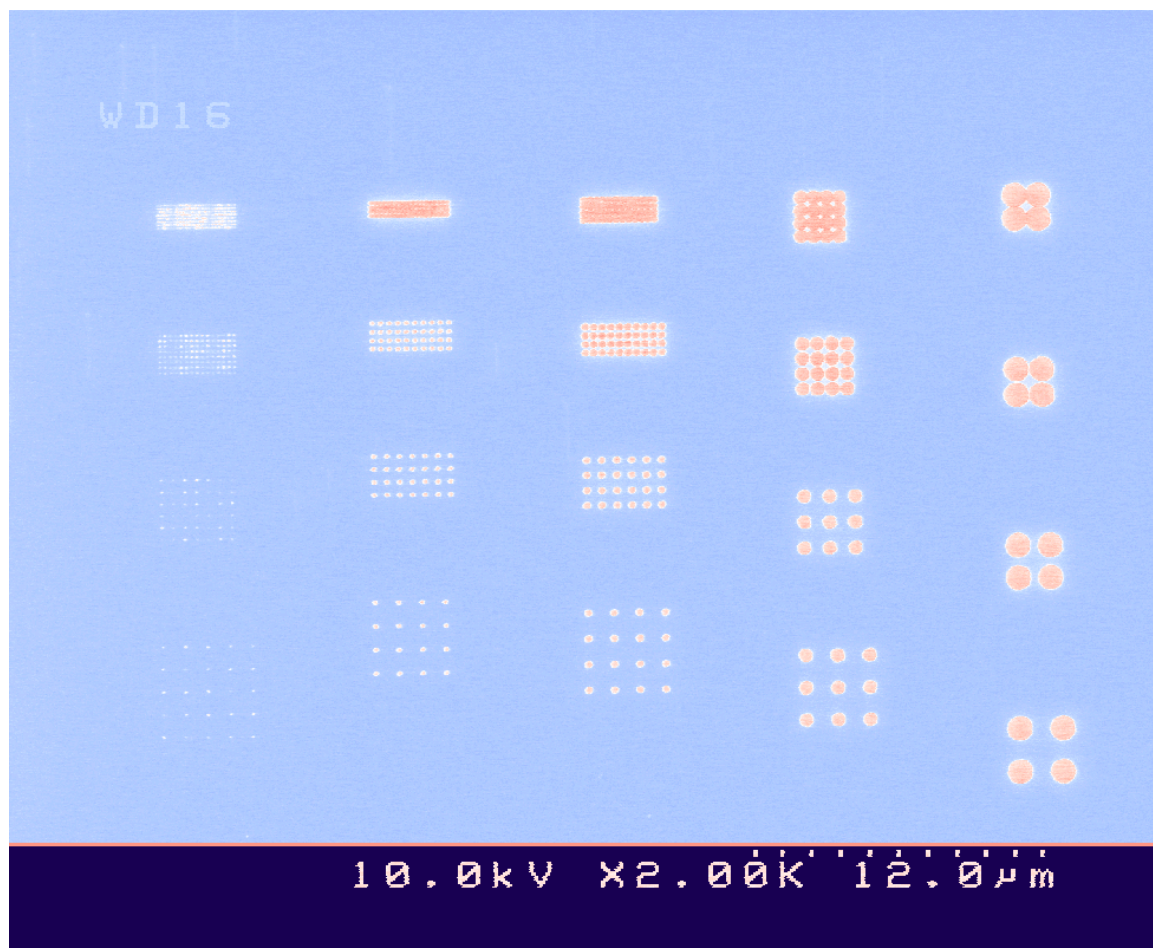


Figure 4.10. 1000 uC/cm² Dose at 300 Magnification. At 1000 uC/cm² the feature definition displayed for different hole sizes and hole distances.

After parameters were tested it was discovered that hole spacing was less critical in allowing for an ideal etch when compared to hole size, yet the distance between the hole will define the exact length and width of the channel being generated. Using a hole feature size of 100nm in diameter several devices were submerged in buffered HF. Several devices at different HF exposure times were measured in the SEM, as seen in Figure 4.11. As mentioned before the HF etch process is diffusion mediated, and

eventually fresh HF will not be able to diffuse into the channel and reach the oxide layer. Figure 4.11 shows that after 30 minutes the HF etched about 2uM of oxide, in an hour 5uM, and after 1 hour and 20 minutes about 7uM of oxide had been etched. With longer time exposures the oxide is significantly reduced; there appears to be no more significant oxide etch for the given hole diameter after the hour and 20 minutes of etching. If the device is left in the buffered HF for a longer time you would have significant loss of oxide layer along the edges of the device, and as a result you would need to protect that oxide before processing a long etch. The etch time is optimized to the 100nm diameter feature size, and if a larger or smaller hole is used to generate a channel another optimization test would need to be performed. Using this information the hole feature spacing can be designed for a channel to the exact length and width desired.

Etching through the oxide layer occurs in spheres, as seen in Figure 4.12, centering on the access channel through the silicon layer. As the sphere grows it meets the bottom silicon surface, which has a significantly slower etch rate than the oxide layer, essentially stopping channel growth in that direction. Etching continues in the other directions of the oxide layer until it meets up with other etch spheres and a complete channel is formed, as seen in Figure 4.13.

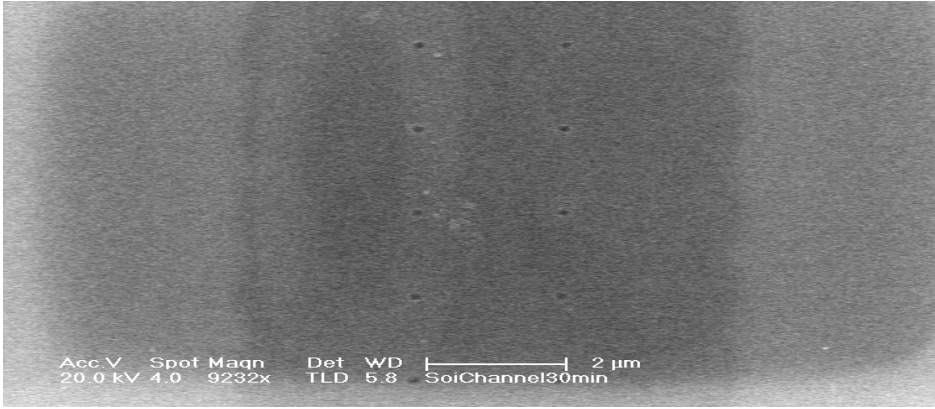
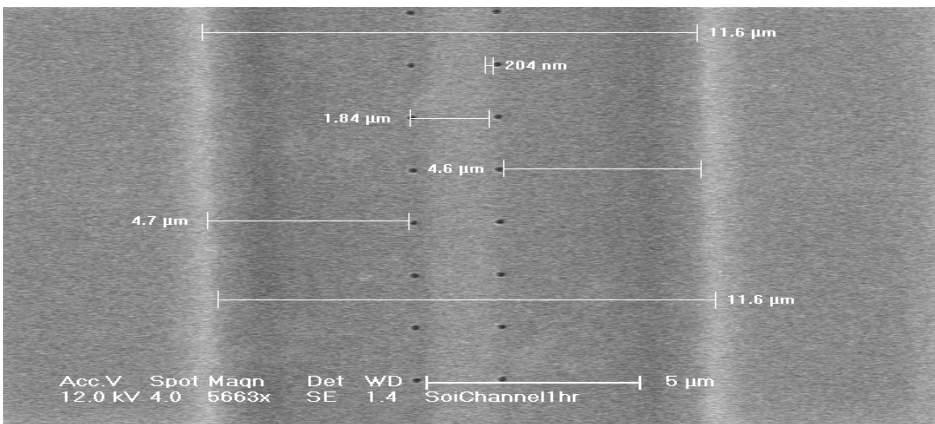
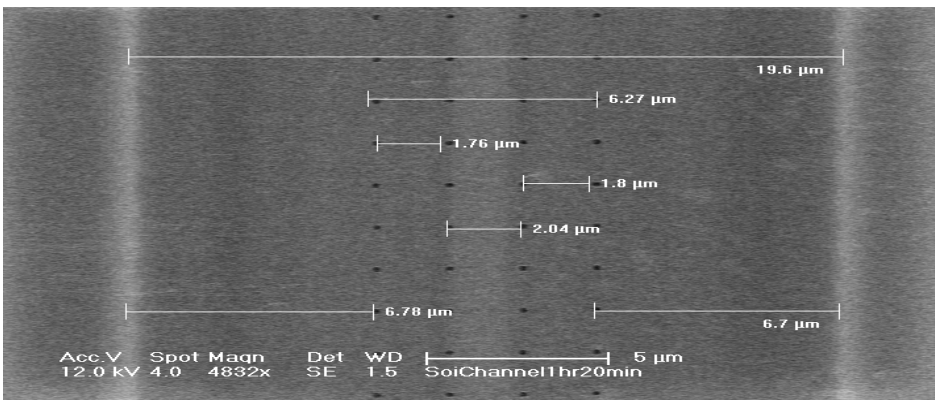
	<p>30min exposure to HF</p>
	<p>1hr exposure to HF</p>
	<p>1hr and 20min exposure to HF</p>

Figure 4.11 HF Etch Time and Distance Etched in SOI Wafer. SEM images of buffered HF exposed SOI wafers after pseudo bosch etch to remove silicon allowing for HF diffusion in oxide layer.

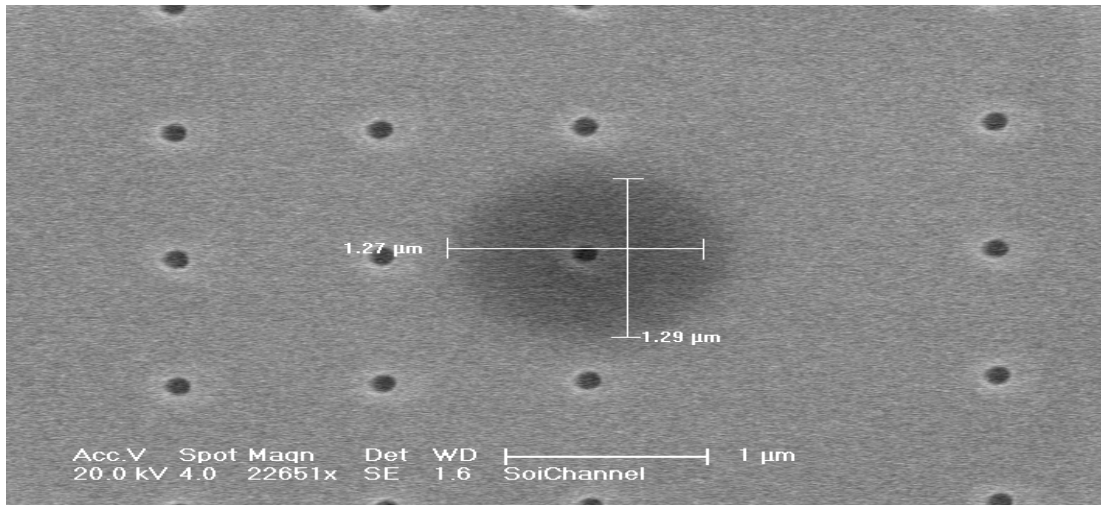


Figure 4.12. Diffusion Etch Inside and SOI Device. SEM image of buffered HF oxide etch of a single access channel in a SOI device

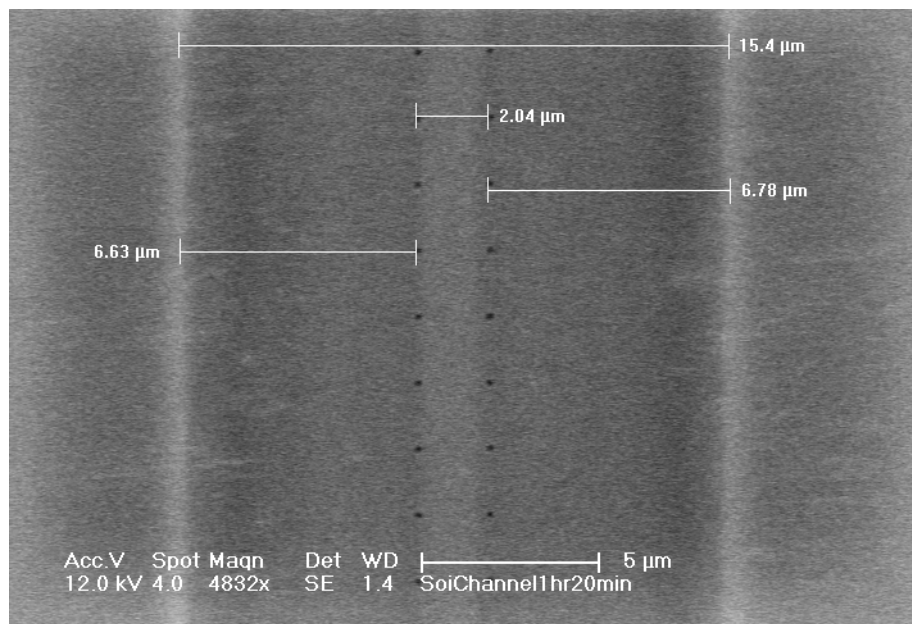


Figure 4.13. Optimized SOI channel. SEM Image of a Channel Formed with an SOI Wafer.

Now that the optimization parameters were determined, a complete clean channel inside the SOI wafer was created, as seen in Figure 4.13. From the image we can observe

that the channel walls are almost 7uM away from the access hole with 2uM distance between the access holes. Examining the surface of the SOI device is helpful to optically distinguish between the etched oxide and the remaining oxide; however, to see how the HF etch affected the walls of the channel inside the device, I used the Nova 600, which is a dual-beam focused ion FEI, to cut an access port to provide a mechanism to image deep inside the channel (Figure 4.14).

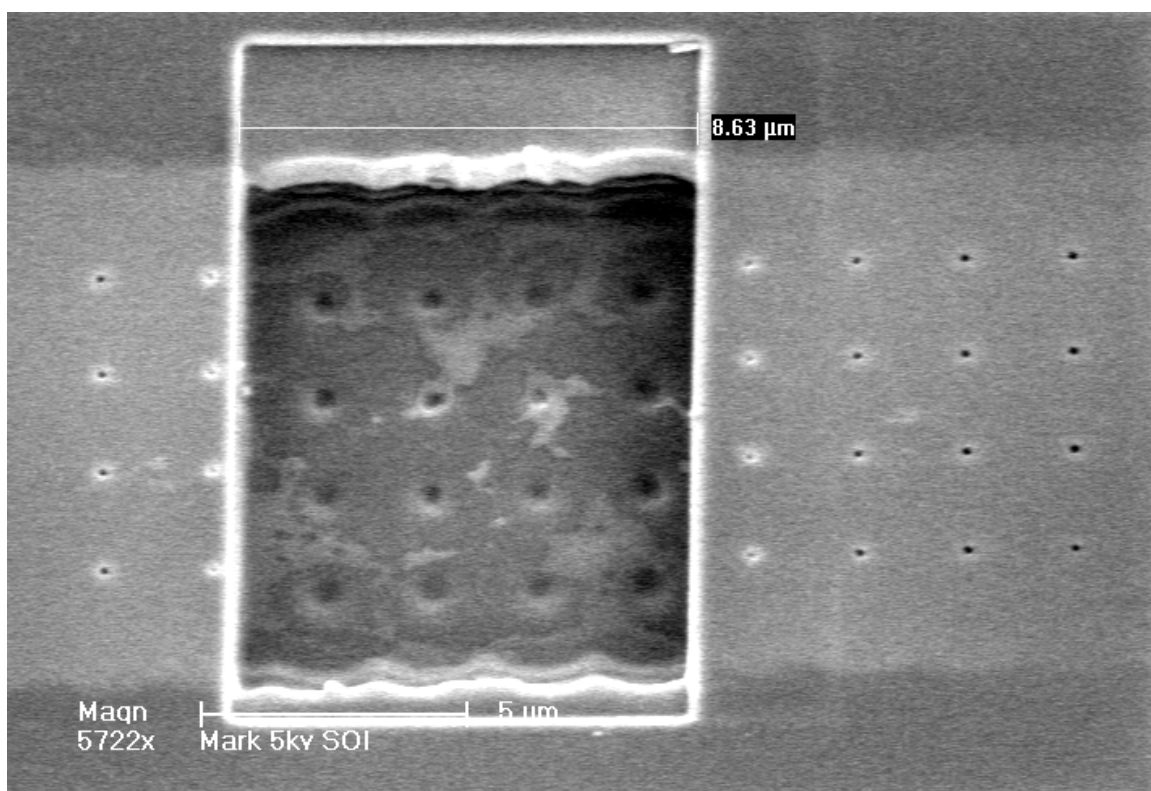


Figure 4.14. Internal Channel Access Port. SEM image after the top layer of silicon was removed.

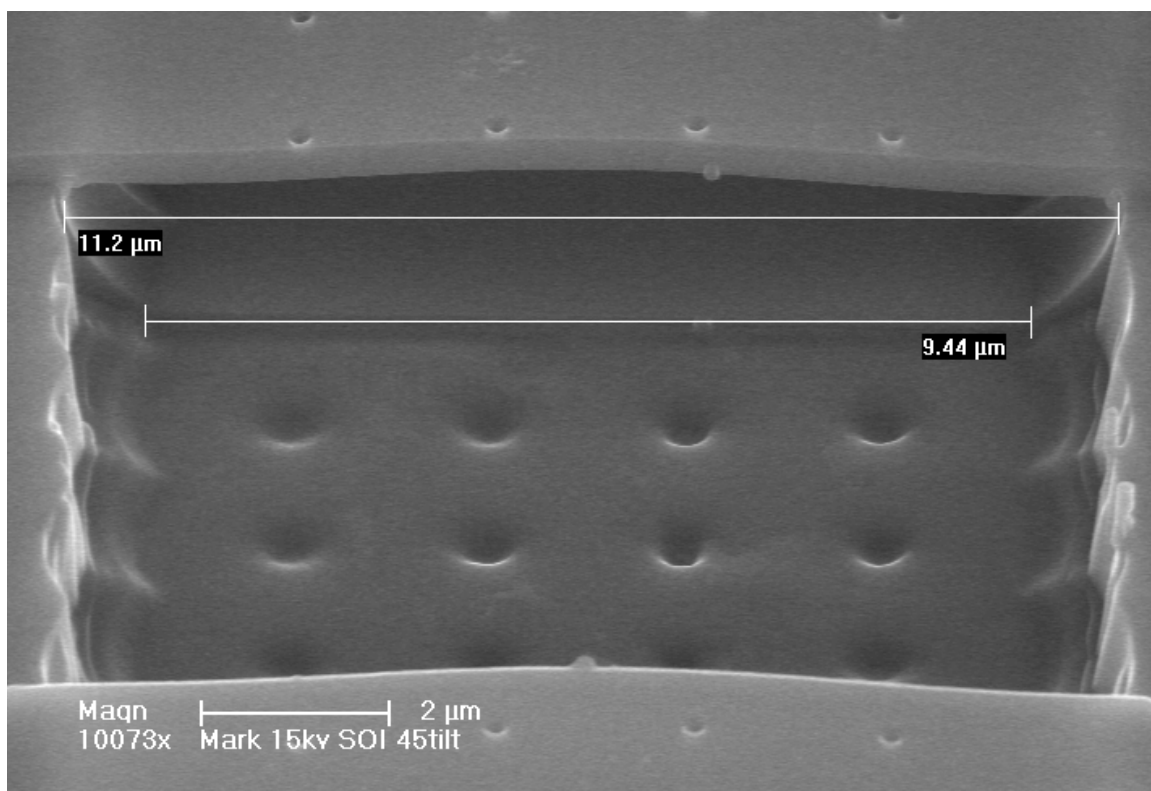


Figure 4.15 SEM Image of the Inside an SOI Channel. SEM image of the channel developed by the removal of oxide of an SOI wafer.

With closer examination of the channel (Figure 4.15) we can observe a difference between the top and bottom length of the channel. As mentioned before, the channel is created by diffusion of HF inside the access hole and when etching the oxide in a spherical fashion the upper wall will be longer than the lower wall. We can also see the spherical etch with the oxide that remains on the wall, since the access holes are spaced (Figure 4.15) by 1 μm small regions of oxide protruding inside the channel. The dimples on the bottom surface of the device were generated when the top layer of silicon was etched away to image inside the channel. Similar to traditional microfluidics, where the channel height is determined by the photopolymer used to generate the channel, SOI

fluidic height is determined by the oxide layer. As displayed in figure 4.16 we can observe that the channel height is 1.75uM.

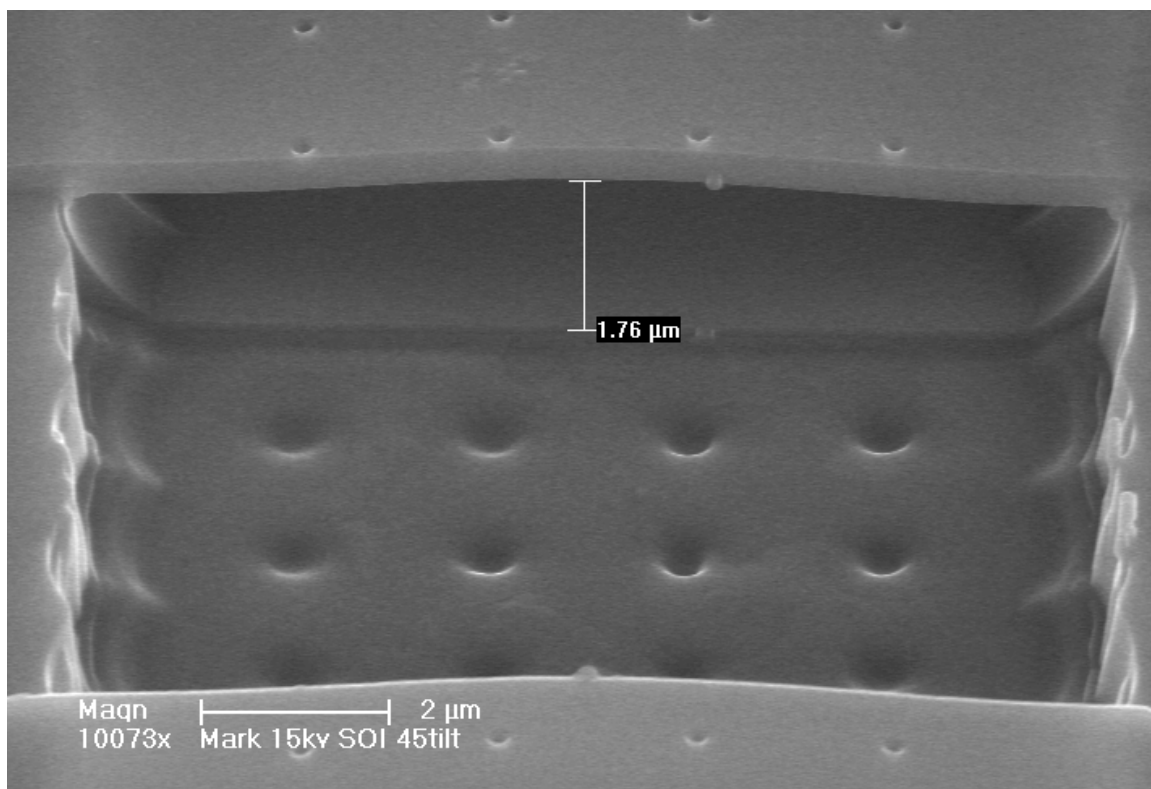


Figure 4.16 SEM Image of SOI Channel Height. SOI channel height is limited to the height of the initial oxide layer of the SOI wafer.

If we increase the magnification, as seen in Figure 4.17, we can observe that the top layer silicon is 364nm thick. The bowing of the top layer silicon is the result of how the SOI is manufactured. Either taking two wafers or growing oxide on both generally fabricates SOIs and then wafer bonding the oxide layers together, or only growing oxide on one wafer and then wafer bonding with an oxide-free wafer. Both processes will cause stress, and as the oxide is removed the stress causes the observed bowing in the channel. This stress ends up not being a problem for biological experiments, since the pressure and temperature used is not sufficient to break the top silicon layer.

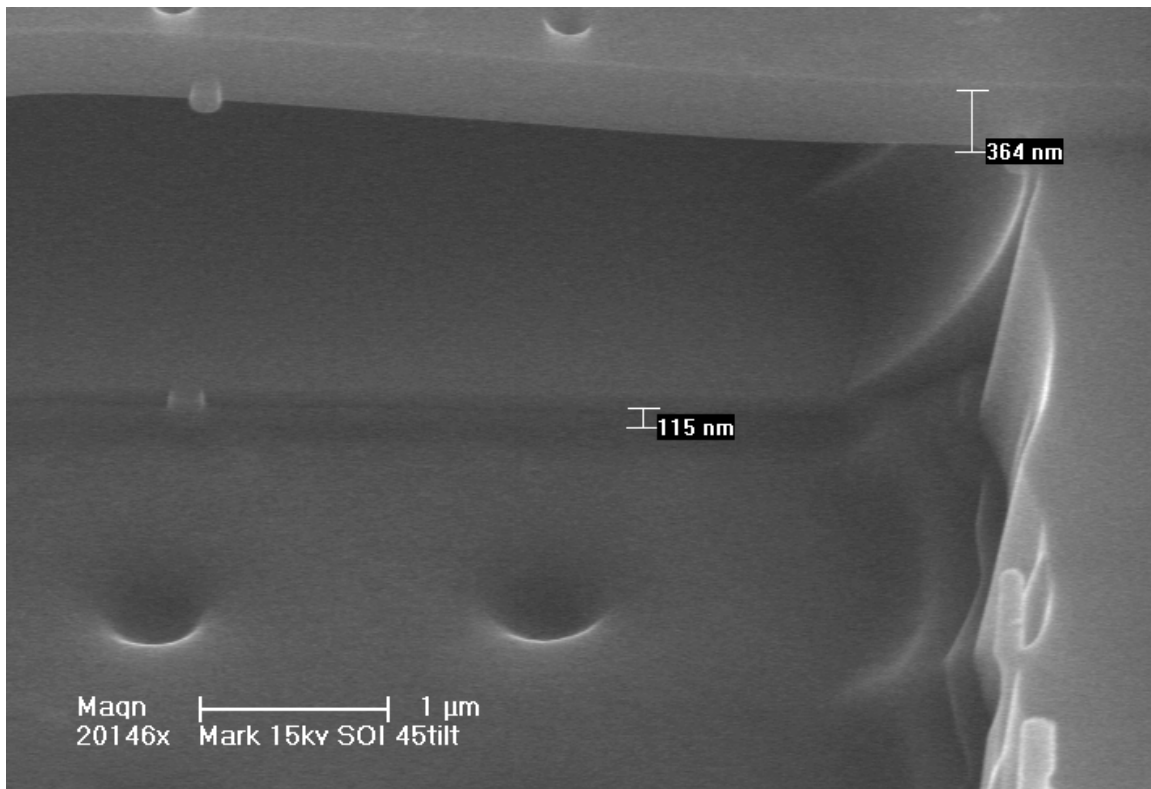


Figure 4.17 Bowing of Silicon Layer. As oxide is removed internal stress in top silicon layer is revealed.

Conclusion

SOIs have the potential to improve the current properties of microfluidic devices and focus on flexible polymers and reintroduce material that was discounted, biased on material properties. By building fluidics into the materials used to develop computers new levels of miniaturization can be achieved that were not possible with current fluidic technology. The development of the microfluidic valve by Steve Quake help further miniaturize fluidics that still often require significant external equipment to run or detection of the fluidic devices. SOI have the potential to bridge the gap between the current fluidic technology and the future fluidic devices that have the biological and electrical components made from the same material. The current polymers can still be

used for valuing and contribute to fluidic movement, yet other materials are superior for actual biological or chemical experiments. Development of a new fluidic device has its own unique challenges, first in trying to generate a working system, but also in optimizing the parameters associated with fabrication. I have proved that it is possible to form channels inside semiconductor material by exploiting the unique properties of the material itself by selectively etching the oxide layer and leaving the silicon layer relatively undamaged. With this design we have the potential to build the electrical components for movement and detection directly on the fluidic system without the need for external equipment. SOIs also have the advantages of having unique surfaces to preform selecting binding and specific regions, where the channel walls are silicon oxide and the top and bottom surface is silicon; this feature can be useful for future development of SOI channel experiments, specifically focusing on the ability to separate biological samples electrically.

Chapter 5

Eletrofluidics

Introduction

The ability to move fluid in a microfluidic device was accomplished with the use of pumps or systems of valves that function as a pump; unfortunately, as expressed earlier, this requires external equipment to control this movement, which turns a micro device into a macro system. Using the developed SOI microchannels from the previous chapter is it possible to use the properties of the semiconductor material to move objects inside the channel without the aid of external equipment or valves.

I have developed, integrated and tested a new class of on-chip controls over fluidic components that can be easily integrated within the microfluidic chip designs. These new devices hold tremendous potential for very real clinical applications that will directly affect current clinical treatment of many disorders; for the purpose of this study, the system focused on cancer detection. The fluidic device used micro-electrodes to manipulate individual cells and nanoliter reagents within micro-channels for single-cell molecular analysis. As a result of this capability for single cell detection, this device will change how we treat cancer patients, by determining molecular profiles of individual circulating tumor cells (CTCs) or, as revealed in a later chapter, how the device can be used to determine the genetic variation of cells. Currently there are no tests available that can predict which breast cancer patients would benefit from trastuzumab beyond disease progression, in part because clinical decisions are based on the HER2 status of the primary tumor biopsy, and not on that of the metastatic tumor. Because a tumor is a

dynamic disease and various mutations can arise during treatment, determining the current HER2 status of the metastatic tumors is critical for treatment decision. However, multiple tumor biopsies during treatment are too invasive for most patients, and new metastatic tumors are too small and too many for biopsy. To address this problem, I have developed devices that can do real-time cell sorting, which would allow a determination of the HER2 tumor status from a regular blood draw by molecular analysis of single CTCs.

Recent work has shown that the number of CTCs in a patients blood is a novel predictor of clinical outcome.⁷⁸⁻⁸⁰ CTCs were identified in cancer patients with a variety of metastatic cancers, with a median yield of 50 cells/ml and purity ranging from 1 to 80%.^{81,82} Enormous effort is being expended to develop methods for non-invasive tumor biopsy and CTCs assessment. However, most systems are specialized on CTC enumeration, and lack the capacity of single-CTC molecular characterization. Our proposed system stands out from others with molecular characterization of single-CTC in addition to CTC enumeration.

Microfluidic devices for clinical use in CTC enumeration and CTC molecular characterization should be robust and trouble-free. Because of the rare number of CTCs that can be obtained from a patient blood sample (typically less than a few hundred cells), the capacity for molecular characterization of single cells is critical to extract useful molecular information from CTCs. I built an electrical control design to replace the cumbersome peripheral support devices of traditional microfluidic devices for a trouble-free device. The proposed device has lithographically defining electrical valves and

pumps with the functionality of controlling picoliter volumes of reagents and isolating rare CTCs through dielectric differences within microfluidic channels. Key components for the system will be fabricated in a metal layer directly on SOI fluidic channels, and samples will actually flow through electrophoretically. CTCs will be detected and isolated with frequency-dependent conductivity signals. The whole system has no moving mechanical components, yet before any cancer cells can be tested I will test the system with beads and similar sized cells to observe if it is possible to electrically manipulate a cell at a low voltage.

Copper electrode cell concentrator

To fabricate the copper electrode a fabrication mask was made in Autocad; the design was sent to CAD Art Services to generate an optical mask. The mask was then placed on top of photoresist coated copper sheets and exposed to UV light. The sheet was then developed in hydrochloric acid, washed in water, and backed in an oven at 80°C overnight. The devices, seen in Figure 5.1, were then individually cut out of the sheet and used for testing. Testing was performed by linking the copper devices with a frequency oscillator and manipulating the frequency from 10Khz to 150kHz.

To initially test the idea of electrically manipulating cells I patterned an electrode in a copper sheet (figure 5.1). The system was designed to concentrate cells in a signal point of the center of the device using only one electrode. In Figure 5.3, we observe a close-up image of the copper pattern from this device, made using copper etch and UV light with an optical mask. The quality of the electrodes is not ideal. The electrode edges are jagged, which can change the overall frequency in that given area, but for a proof of concept, the device will work, although the device will have to be modified with further

experiments to generate better quality electrodes. Fluoresce labeled beads were diluted in a PBS solution spiked with calcium to make a 0.1 molar calcium PBS solution, although the PBS solution has ions for the movement of the bead, and calcium was used to add to the ion concentration.

The design was to use low voltage but variable frequency to move the beads, and since the test device will only use one electrode, the distance between the coppers will decrease as it gets closer to the center of the device (Figure 5.3). The voltage used was 0.2 volts and a frequency of 50kHz, and since the copper electrodes are not uniform it is not possible to determine the exact frequency at a given level of the device. Before the device is powered the labeled beads are distributed around the device. Once power is applied the beads quickly move between the electrodes, and as time progresses the beads start to concentrate towards the center (Figure 5.2). Since there is no system of electrodes the beads remain between the electrodes. After successful demonstration that the proof of concept works by manipulating beads, a redesign of the device was necessary to enable the movement of cells, having two electrodes is not sufficient to move beads or cells and an array of electrodes is needed to move beads or cells.

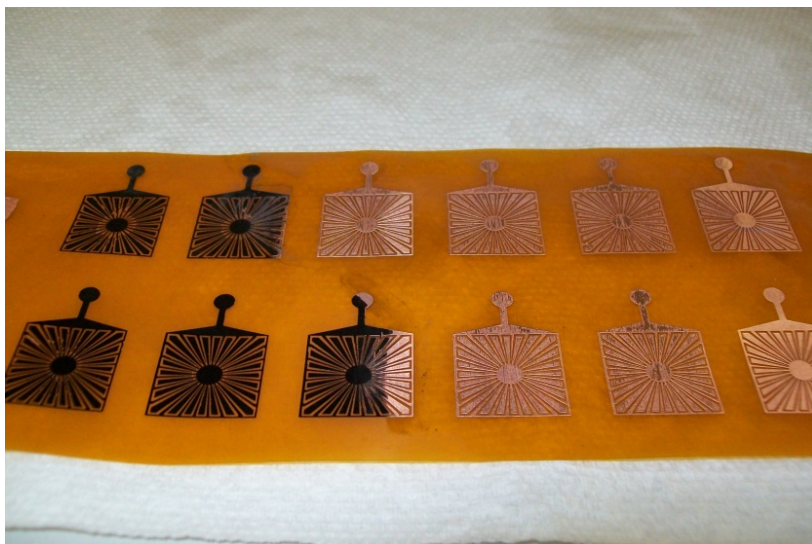


Figure 5.1 Copper Electrodes. Copper electrodes on a fabrication sheet after exposure to UV light and hydrochloric acid etch.

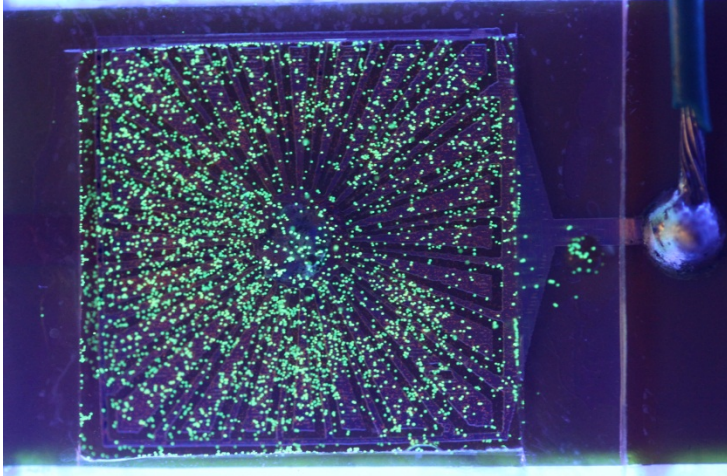
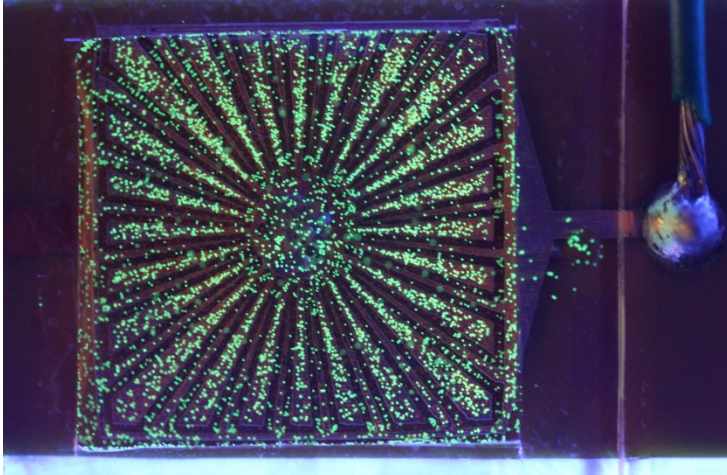
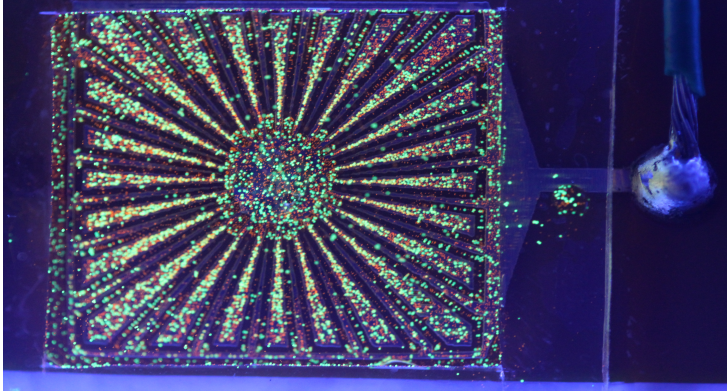
 A photograph showing a square copper electrode on a dark background. The electrode is covered with a dense, uniform distribution of small, bright green beads. A small, dark, irregular shape is visible on the right side of the electrode.	Initial distribution of beads
 A photograph showing the same square copper electrode. The beads are now concentrated in a radial pattern, with a dense cluster in the center and lines of beads radiating outwards towards the edges. The background is dark, and the electrode is illuminated from below.	Right after power turned on
 A photograph showing the same square copper electrode. The beads are now concentrated in a radial pattern, with a dense cluster in the center and lines of beads radiating outwards towards the edges. The background is dark, and the electrode is illuminated from below.	After several minutes of power on

Figure 5.2. Copper Electrode Test System. Individual copper devices were attached to a frequency generator and tested to observe the movement of labeled beads. The top image is with the device not powered, the middle image is power first applied, and the lower image is with power applied for 5 minutes and frequency range applied.



Figure 5.3. Closer Image of Copper Device. With increased magnification we can observe that using UV optical mask lithography does not generate crisp electrodes.

Electrodes made of chrome on glass

Once the proof of concept was established with the copper electrodes determining the proper spacing of the electrodes themselves, new spacing requirements were needed to allow for optimum cellular movement. Using commercially available glass slides with chromium and photoresist already deposited, I used the Heidelberg Instruments DWL-66 and later the EBPG laser to write the electrode designs with variable line spacing, as seen in Figure 5.4. The chrome masks were developed in M1039 developer (Microchem). From the image in Figure 5.4, unlike the copper electrodes, the chromium electrodes are more uniform. Although both processes involve photolithography, the copper electrodes

involve generating a mask followed by the exposure of the photoresist coated copper with UV light and etched with hydrochloric acid. In contrast, the chromium electrodes are directly written with an e-beam system, allowing for greater resolution, and are developed and etched with chromium etch, which is a mixture of nitric and acetic acid.

As with the initial problem when using only one electrode, when trying to move beads in the copper system, the chromium system must have multiple electrodes as well in order to create an oscillatory activation of electrodes, allowing the cell to move between active electrodes. This means that when designing the electrodes, no single active electrode should be active next to itself (Figure 5.4, right image). After several runs it was observed that there is a correlation between frequency and electrode spacing, and the greater the distance between the electrodes the higher the frequency that is needed to move the beads, with the optimum range between the electrodes of 100um or less.

Using this information a new chromium mask (Figure 5.5) was designed where the electrode spacing was 100um between the same electrode, and either 40um or 60um between different electrodes. This design should allow for the cell to migrate to the center of each electrode when powered, and with the electrodes oscillating on and off the cells should move between the electrodes. Limited spacing between electrode pads was needed to ensure that the correct electrode is active at a given time (Figure 5.6).

In attempt to replicate the conditions found with an SOI water glass microscope cover slides were used. Initially the glass sides were washed in a 50-50 mixture of chloroform and methanol, and rinsed with water. To prevent a solution of beads from

covering the glass slide completely, the slide was also coated with a thin layer of PDMS with a hole of bare glass left open for the experiment (Figure 5.7), to observe if beads will still migrate between the electrodes with the glass slide between the solution and the electrodes (Figure 5.7B). As illustrated in the figure the labeled bead are migrating between the electrodes. With closer examination of the device, (Figure 5.8), we can in fact see beads migrating between the electrodes of the device with a glass coverslip covering the electrodes. The slightly darker bands are the electrodes and the lighter bands in the image are the spaces between the electrodes.

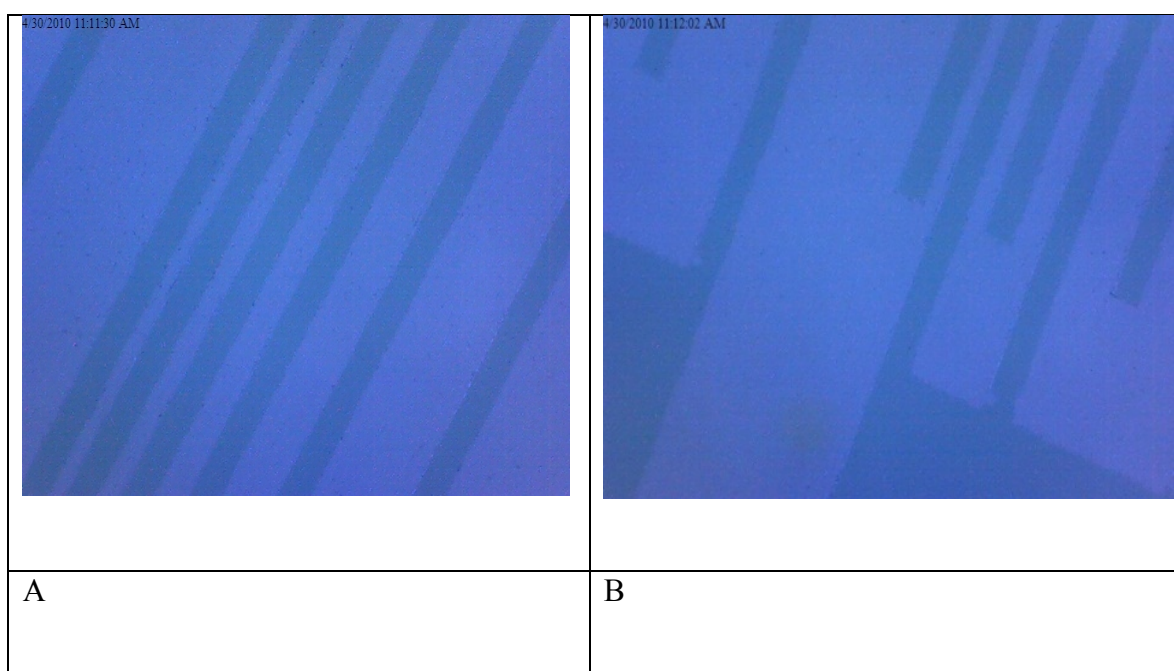


Figure 5.4 A and B. Chromium Electrodes Patterned with Direct-Write Laser System

Heidelberg Instruments DWL-66.



Figure 5.5 Chromium Etched Electrodes. Chromium electrodes spaced 100 μ m, 60 μ m, and 40 μ m apart from each other.

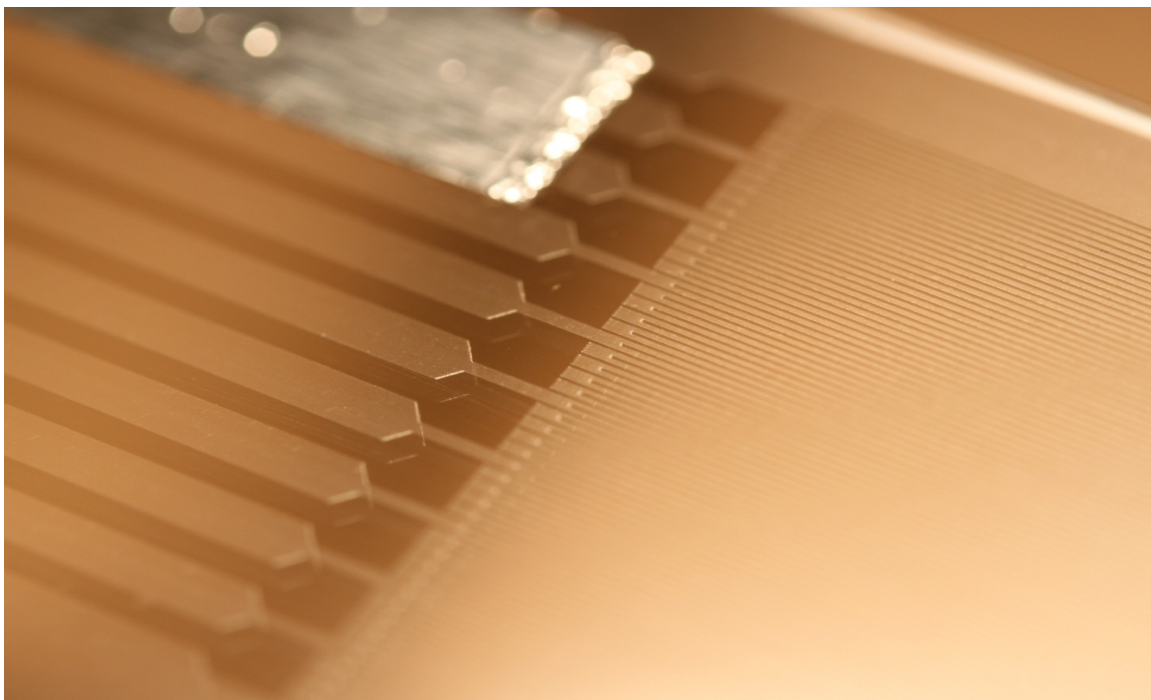


Figure 5.6. Close-up Image of Chromium Etched Electrodes. Chromium electrodes with access pads to allow for attachment to function generator; crisp features are the direct result of e-beam lithography.

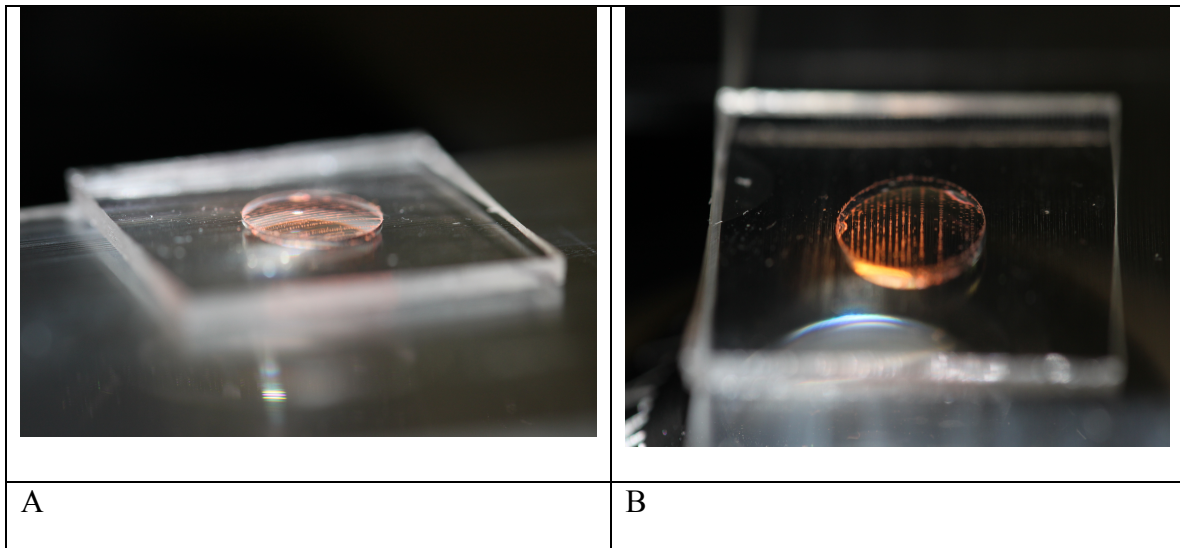


Figure 5.7. Two Different Views of PDMS Covered Glass Slides. A PDMS covered glass slide with a sample port was fabricated and placed over chromium electrodes.

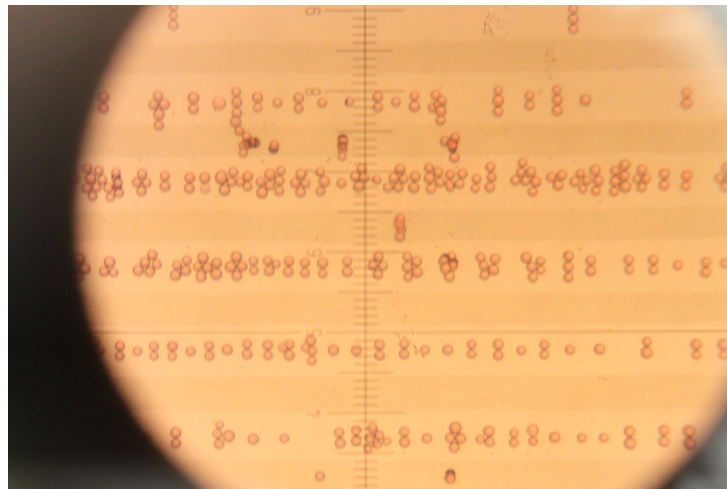


Figure 5.8. Close-up Image of Glass Slide Cove Port. When frequency is applied we can observe the congregation of beads between the electrodes of the device.

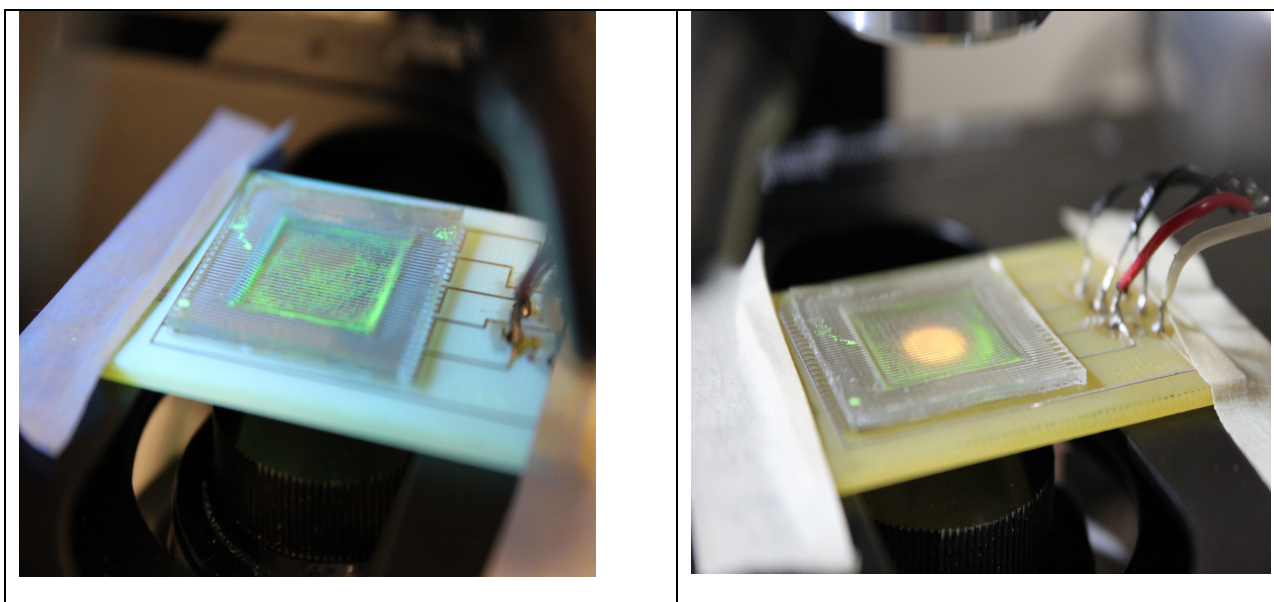
Once the parameters were determined I started to fabricate the channels on SOI

devices with chromium electrodes. The cost of the SOI is significantly greater than that of simple glass, and hence the need for optimization was performed when compared to other devices. After successful device development I tested to see if beads could flow through the developed SOI channel (figure 5.9). To perform movement, the test device would either need a lower concentration of cells or wider channels.



Figure 5.9. Beading Flowing Through an SOI Channel.

Electrofluidic channels inside SOI devices



A	B
---	---

Figure 5.10. SOI Wafer Sorting Device

A new system was fabricated out of SOI wafers where channels were developed with the technology presented in Chapter 4 and chromium electrodes; the device was then attached to a function generator for testing (Figure 5.10). A single bead size was used to test if the new system still functions as in previous tests. In Figure 5.11 we can observe consistent test results as before, and when a function is applied to the electrodes the beads congregant between the electrodes. All the samples that were tested used simple single sized beads; to test to see if the system can actually preform the intended function, a complex sample of different size beads was used (Figure 5.12).

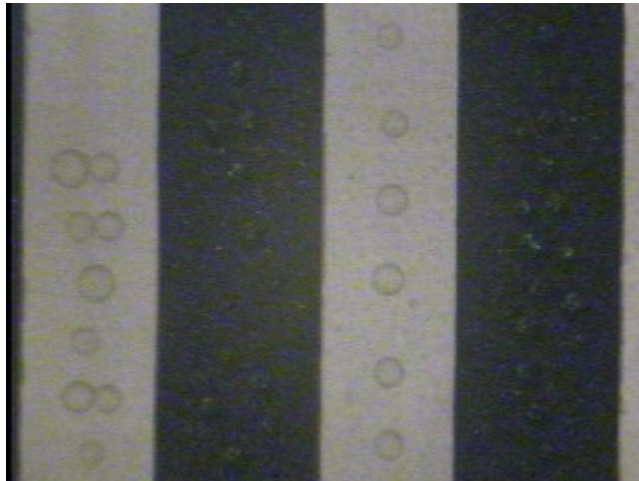


Figure 5.11. Beads Congregating Between Electrodes.

When testing the complex mixture, the sample was injected into the SOI device and then left to settle for an hour, as this should prevent any additional Brownian motion or added energy from the injection of the sample. The movement of the complex sample

can be seen in figure 5.11, and if we focus on the relative concentration of bead sized close to the injection site where the concentration of larger beads appears consistent, it appears to be uniform distributed (Figure 5.11 A), yet if we examine the beads farther down from the injection site the distribution of smaller beads is reduced (figure 5.11 B). The proposed mechanism is ion movement. As the frequency modulated in the device, ions either congregate towards or away from the electrode, and as this happens the ions push the cells like ships in the wind, and since larger cells have more surface area than smaller ones these cells move faster. This can be explained with a dielectrophoresis force equation (Figure 5.13), where r is the radius of a cell ϵ are permittivity and dielectric constants and E_{rms} are the frequency and voltage applied, respectively.

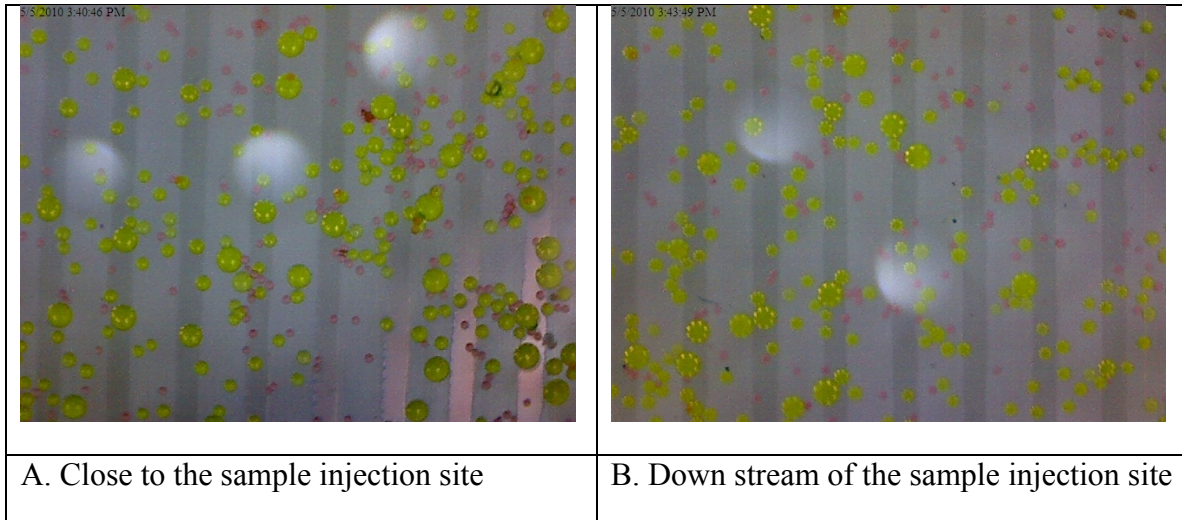


Figure 5.12. Complex Sample of Different Size Labeled Beads.

$$\langle F_{DEP} \rangle = 2\pi r^3 \epsilon_m \text{Re} \left\{ \frac{\epsilon_p^* - \epsilon_m^*}{\epsilon_p^* + 2\epsilon_m^*} \right\} \nabla \left| \vec{E}_{rms} \right|^2$$

Figure 5.13 Dielectrophoresis Force Equation.

The device works with beads, but the intent is to run human cells into the system to see if larger cells can separate from smaller cells. Just as in the previous experiment I

injected the sample in the system and let it settle to prevent any false data from injection movement. After applying a 100kHz field at 0.2 volts I was able to observe movement of larger cells over smaller ones, as seen in Figure 5.14. It is difficult to display cell movement without a video; however, I was able to find a single small cell and a large cell where you can see that the larger cell moves at a faster rate than the smaller one.

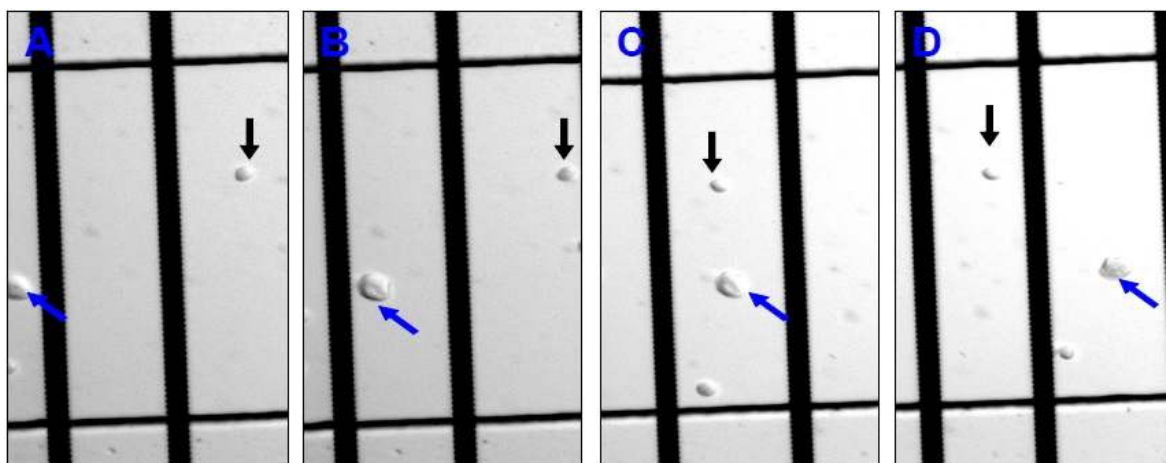


Figure 5.14. Separation of Cells by Size. Two cells with different size flow in a 100 μm SOI channel by dielectrophores force generated with 0.2 V with miniaturized electrodes. A) A small cells (black arrow) enter the channel in front of a larger cells (blue arrow). The larger cells is approximately twice of the size of the small cell. B) The large cell moving faster and shorten the distance between them. C) The large cells catch up with the small cells. D) The large cells moving past the small cell.

Conclusion

The innovation of this study has important practical applications. The technical and clinical innovations of this study could lead to a fundamental change of cancer treatment. The clinical innovation of using CTC for cancer diagnosis and treatment

evaluation is expected to deliver more effective therapies, yet to do this you have to successfully separate CTC from the other cells. This would be one step closer to the goal of personalized medicine, where treatments are designed for the individual and not for how the group reacts.

Obviously, electrolytic flow systems significantly change the local concentration of ions, as these respond to the applied electrical fields.⁷²⁻⁷⁵ Indeed, this is the basic principle behind electrophoresis, a widely used method to sort ions, bacteria, and cells by their mobility for countless applications.⁷⁶⁻⁸¹ However, this ion segregation effect also limits the use of continuous electrical current in devices where the ion concentration should remain unaltered. As a solution to avoid ionic segregation, pulsed or alternating current electrophoresis methods have been developed in the past. These systems, operating at frequencies into the MHz range, have been used to demonstrate dielectrophoresis, sorting of particles by size and dielectric constant.⁸¹⁻⁸³ For improved control over the molecules, viscous fluids such as gels are often used. Another consequence of applying an electrical field onto ionic solutions is that above the dissociation potential of water of approximately 2.03V, evolution of hydrogen and oxygen gas occurs at the electrodes, and often bubbles form within microfluidic systems. This effect is commonly an unwanted problem, as these small gas bubbles often block the flow of liquids through the system.

However, both ion segregation and electrolytic dissociation can be addressed by miniaturizing devices and completely integrating the system within either an SOI or PDMS based fluidic devices, for the sorting of live mammalian cells (i.e., CTCs). While

this is not the first time that such an approach was used to move cells, by combining electric movement with nanofabrication capabilities and integrated electrodes within the microfluidic system for single-cell sorting, this system does not require a large amount of external control hardware. The resulting devices, with minimal external interfaces, will be able to be readily controlled from electronic devices, such as laptops and cellphones, and will be able to be deployed in applications where more conventional fluidic systems monitored with fluorescent microscopes cannot function.

I have built a prototype device to demonstrate the operation principle of our proposed platform. As shown in Figure 5.14, a microfluidic channel in PDMS was bound to the rows of miniaturized chromium electrodes. Applying 0.2V to these miniaturized electrodes generates an electrophoretic flow to move live cells in PBS. The applied low voltages did not generate any electrolytic gas as we do not exceed the hydrogen evolution potential. As we use many electrodes, and apply voltages across these in sequence, the ion segregation typically associated with electrophoretic systems is avoided. The ion chemistry in our flow channels will remain relatively constant, as diffusion is allowed to redistribute the ions between applied electrical pulses. We also observe that cells with different sizes are moving at different speeds, proportional to their cross-sectional areas. Larger size cells move faster than smaller size cells, as demonstrated in Figure 5.14, which thus represents a cell sorting mechanism.

Chapter 6

Persistence Length Quantitative Polymerase Chain Reactions Using Quenchiplexing and FRETplexing

Introduction

Cancer is a group of genetic diseases that is poised to overtake cardiovascular diseases as the leading cause of death in the world, largely due to the aging population in the world. In the US alone, there are over 600,000 new cases and 250,000 deaths per year⁹⁸ and the four leading cancers, lung, breast, pancreatic, and colorectal, contribute significantly to the amount of the new cases and deaths. Hundreds of billions of dollars have been used combat cancer in both research and drug development, and as a result a wide array of therapies and drugs were developed, yet it has only been in the past ten years that targeted therapies have established themselves as powerful and effective tools that increase a patients' longevity and avoid the side effects and morbidity of conventional chemotherapy. The advent of targeted therapy comes from the idea that since cancer is a genetic condition, most individual's cancers result from a combination of specific and unique mutations. Old cancer treatments were general to specific cancers; however, therapies work on specific pathways, which can be circumvented by certain mutations, leading to drug resistance. As a result, extremely expensive drugs⁹⁹ fail to benefit a significant portion of the patients¹⁰⁰⁻¹⁰², thereby wasting health care resources and decreasing the patients' overall chances of survival. Systematic detailed genetic analysis of tumors, combined with a knowledge of the mutations critical to drug resistance, can answer this problem, but it comes with a increase in cost and time to treatment. Currently there are no techniques that simultaneously possess the necessary

affordability, coverage, speed, throughput, specificity, and sensitivity to provide such tissue analysis on a routine clinical basis.

To answer this challenge, I have helped to develop and provided two novel techniques called quenchplexing and FRETplexing. Current methods for identifying nucleic acid targets involve using intercalating fluorophores or nucleic acid probes. For instance, conjugating fluorescent dyes and quenchers onto short sequence nucleic acids allows for specific, fluorogenic tagging of nucleic acids. This technique is commonly used, and is the mechanism of action for hydrolysis probes (such as TaqMan and FRET) and molecular beacons. If a target sequence is present, its probes and primers will hybridize to it. As the polymerase extends the primer, the 5' exonuclease activity of the Taq polymerase breaks the probe sequence. This separates the fluorophore from the quencher and generates a strong positive signal. Similar signals can be generated using molecular beacons, which are short pieces of DNA that have a fluorophore conjugated to the 5' end and a quencher conjugated to the 3' end. At lower temperatures molecular beacons form hairpin structures that bring the fluorophore and quencher into close proximity. The FRET effect inhibits fluorescence even while the fluorophores are being pumped. When heated, the beacon unravels and is free to hybridize with the target sequence. As this hybridization occurs, the fluorophore is separated from its short strand nucleic acids, generating a strong signal.

Both of these new methods utilize automated PCR and the information acquired from a PCR machine. Under a traditional PCR method, primers are used to amplify a given piece of DNA. These pieces of DNA can be specific for general amplification primers. After the reaction has finished its amplification cycles, the accumulated data

appears as documented in Figure 6.1. Unfortunately, in the case of many reactions, since the label is general, the only information that is generated is knowledge that something in the reaction was amplified, or you need to add an additional specific label to determine if one specific target was amplified. With these new methods there is no need for the addition of an additional specific label, you acquire the specific information from the primers themselves and it is even possible to generate other data from the PCR reaction, beside just DNA amplification. To test this system I used the six most common mutations found in KRAS that contribute to colorectal cancer.

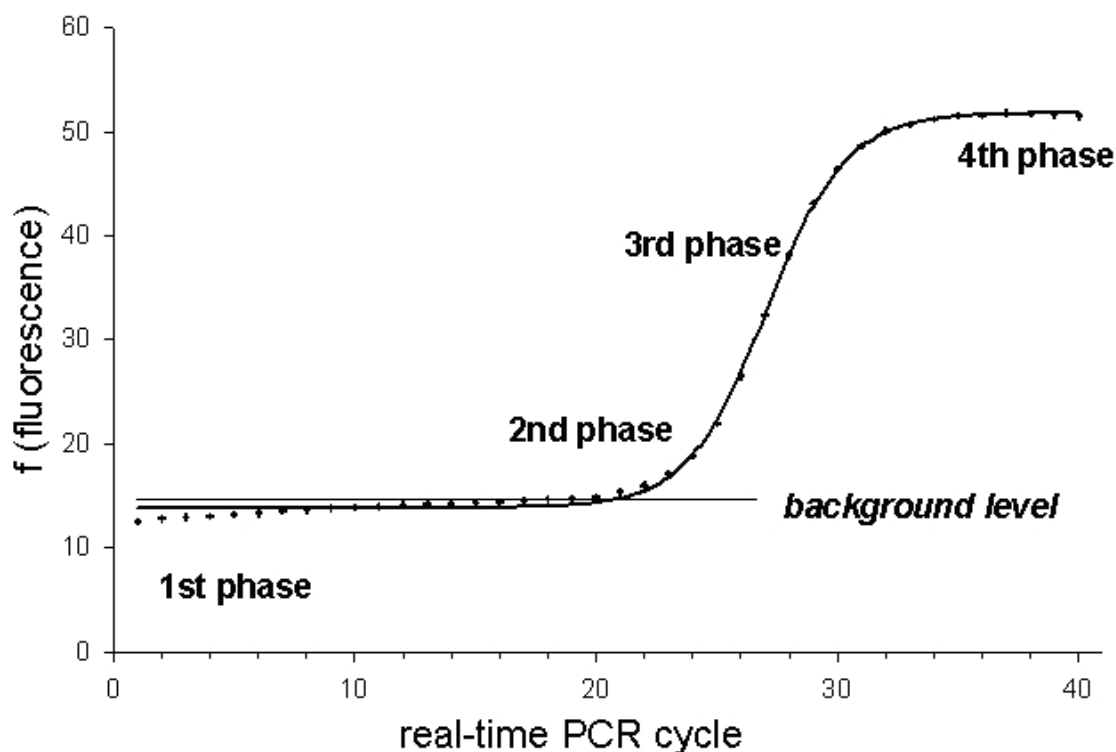


Figure 6.1. Iconic PCR graph.

KRAS Mutations in Colorectal Cancer (CRC) is responsible for 140,000 new cases and 49,000 deaths per year in the US alone⁹⁸. One of the most effective and widely used drugs against CRC is Cetuximab, which is a \$1.75B/yr industry in the world⁹⁹. However,

KRAS mutations lead to resistance to Cetuximab¹⁰⁰⁻¹⁰² in at least 35% of the patients. As a result, the American Society of Clinical Oncology (ASCO) issued a recommendation in 2009 that patients need to be tested for KRAS mutations before being prescribed the drug, with projected net savings of \$753M per year worldwide¹⁰³. However, half of the patients that test negative by traditional allele-specific assays still fail the 8-week \$30,000 regimen. Hence, new and more sensitive techniques are necessary to ensure proper stratification of patients. Thus, this technique would have a major clinical utility. Furthermore, KRAS mutations are SNP's, which are perfectly suited for PCR systems. Hence, KRAS in CRC is the ideal system for the proof of principle.

Material and Methods

Primer design

A pair of forward and reverse primers is constructed to be specific to a corresponding target sequence, which was determined by using the NIH gene BLAST program and is designed to function at reaction conditions of q-PCR. In general, the primers can be selected to ensure that the forward and reverse primers are specific to the corresponding target sequence and have similar melting temperatures (preferably within 1 or 2 °C from each other and no more than 5°C) so that specific hybridization and extension of both forward and reverse primers takes place under the same reaction conditions in the reaction mixture. Using the reaction conditions of commercially available q-PCR kits, primers can be typically between 20 to 35 bp long to allow for enough specificity at the related melting temperatures. When the target sequence includes a SNP or point mutation, the primers typically have the 3' end base overlapping the point mutation to maximize sensitivity. In particular, for detection of a SNP a base

complementary to the expected SNP in the target sequence is included in the primer at the 3' end of the primer within a range of 1 to 3 bp from such 3' end towards the 5' end direction, preferably at the 3' terminus.

A similar approach can be used for a different variation of a reference polynucleotide analyte, e.g., a mutation, deletion, or insertion, wherein the primers can be designed so that they specifically bind to a target sequence where the expected variation might be located in one or more consecutive base pairs that are indicative of the variation. In particular, the primers are designed to specifically bind to the sequence indicative of the variation, preferably with their 3' end.

All oligonucleotides were synthesized by Integrated DNA Technologies (Coralville, Iowa). Diagnostic sequences were input into IDT's OligoAnalyzer 3.1 tool. Probes and primer pairs for each target were chosen, from the OligoAnalyzer's set of generated sequences, to minimize homology with un-intended targets, probes, and primers. Forward primers for all targets were synthesized with a fluorophore at the 5' end, while the reverse primes for all targets were synthesized with a quencher at the 5' end for quenchplexing or a complement fluorophore for FRETplexing. Sequence information is tabulated in Tables 6.1 and 6.3. Nucleic acid products were synthesized and lyophilized by IDT. These products were reconstituted with TE buffer and aliquoted for experimental use. All nucleic acid targets were reconstituted in TE buffer, pH 7.0 (Life Technologies, Carlsbad, CA). Dilutions were made using UltraPure RNase-free Water (Life Technologies, Carlsbad, CA).

Assay Development

In the novel method quenchiplexing the same principles governing fluorophore - quencher interactions can be used to identifying nucleic acids based on persistence length. In this novel technique, called “quenchiplexing”, specific forward (FWD) and reverse (RWD) primers with fluorophores and quenchers, respectively, were designed for a particular target, and this target can be a virus, gene, RNA, or SNP. As the target is amplified with successive cycles of a polymerase chain reaction, the fluorophores and quenchers get incorporated into the template strands (Figure 6.2) and generate a FRET or quenching signal (Figure 6.3 and 6.4). In the Figure 6.2, f is the fluorophore label attached to a primer and q is the quencher label attached to a primer and in the case of FRETplex the quencher label is replaced with a complement fluorophore label to generate a FRET signal.

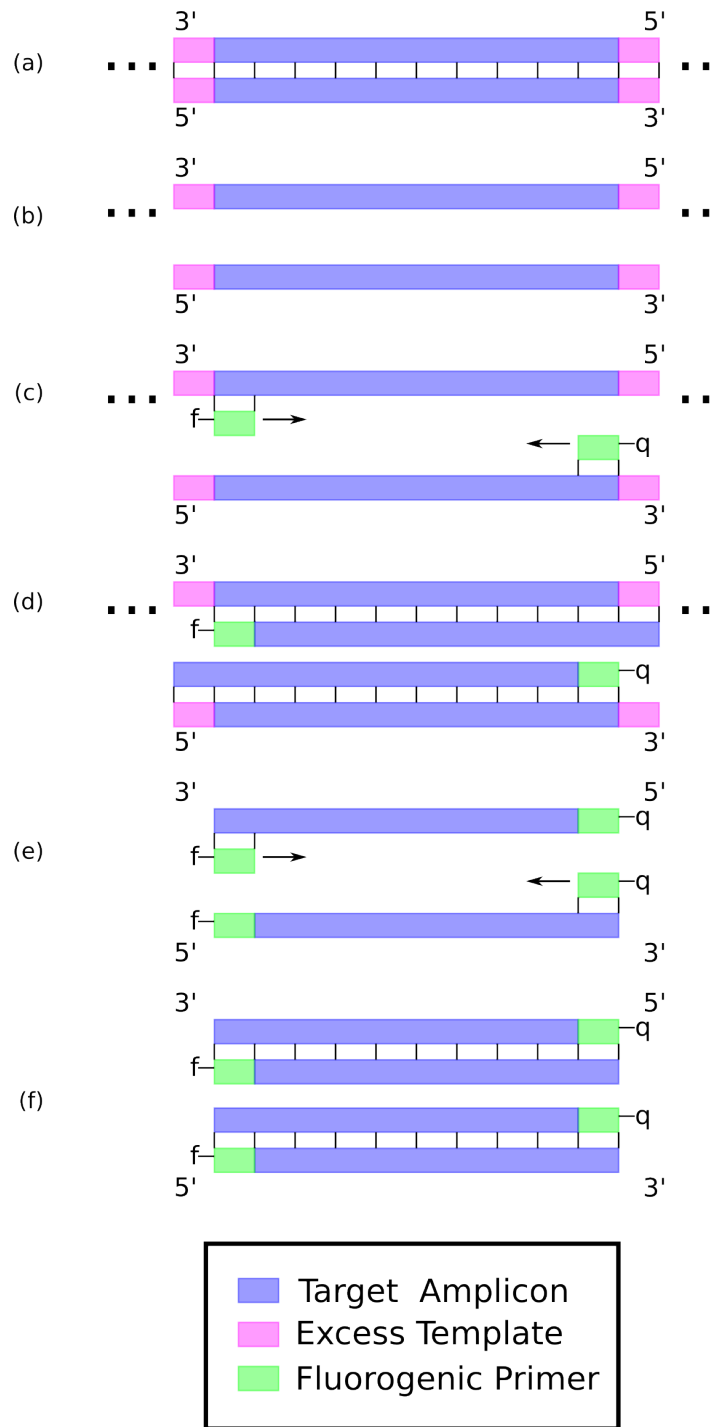


Figure 6.2. QuenchiPLEX PCR Procedure.

As the length of the template strand is known (it is defined by the locations of the forward and reverse primers), the extent of the quenched fluorescence will be fixed for a particular target. This technique will work as long as the separation between the

fluorophore and quencher is within the Förster radius of the quencher. After several cycles of a PRC cycle occur, if the desired target is present, the fluorophore tagged primer generated amplicon will hybridize with the quencher tagged primer, resulting in a reduction in fluorescent intensity in a target specific inverse PCR amplification graph (Figure 6.2).

In a similar but also novel method, FRETplex quenchers are replaced with another fluorophore. When the primer pairs are designed to attach to a donor and acceptor of a FRET donor-acceptor chromophore pair, and to specifically bind to target sequences within one or more target polynucleotides, the primers specifically bind to the corresponding target sequence; the primers present the FRET donor and acceptor at a distance up to four times the Förster distance for that FRET donor-acceptor chromophore pair.

Both methods exploit fluorescent intensity in generating data. Under normal PCR methods (Figure 6.1) amplification occurs when primers interact with a target sequence. In quenchplexing, the fluorescent intensity is uniform (straight line) when no target is present; this is the result of no DNA hybridization to allow quenchers and fluorophores to hybridize to each other, yet when the specific target is present the forward and reverse primer can hybridize together and cause a drop in the fluorescent signal (delta blue arrow in Figure 6.3), signifying the presence of the target analyte. In FRETplexing, in the absence of a specific target no fluorescence is observed, since the forward and reverse primers are unable to hybridize to each other, generating no signal, yet in the presence of the target the primers are able to hybridize together resulting in a FRET signal (Figure 6.4), where the delta displayed as the blue arrow in the figure is the change in fluorescence.

over the background signal.

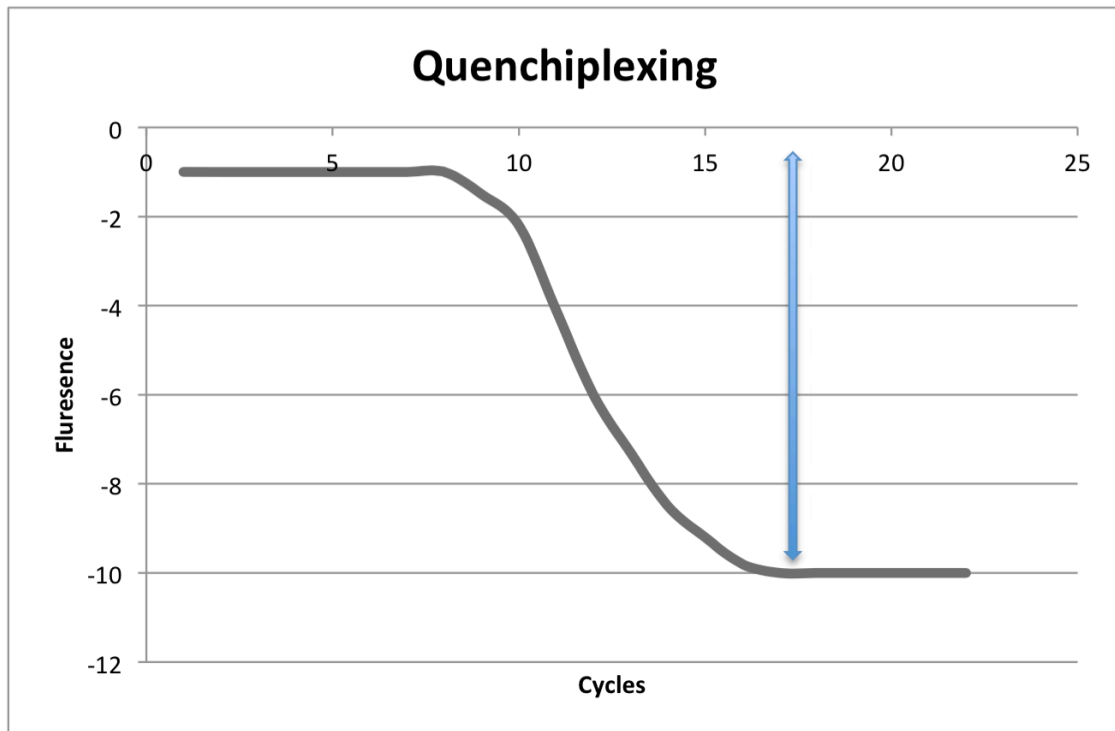


Figure 6.3.Example of Quenchiplexing PCR Result.

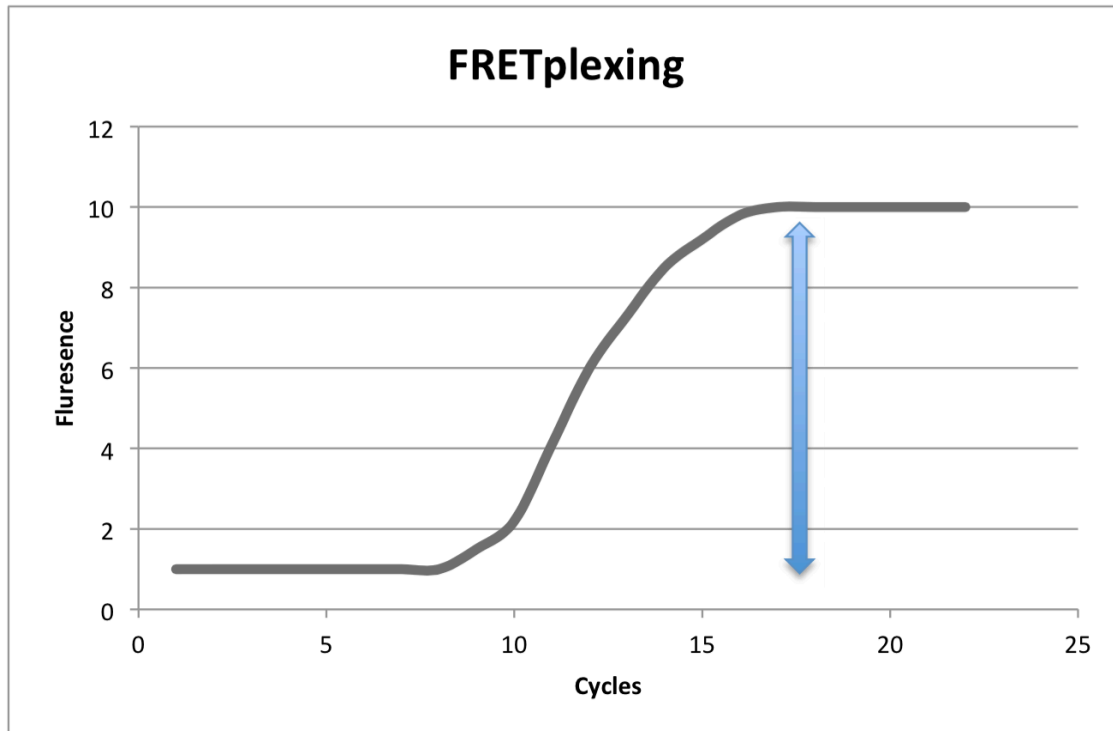


Figure 6.4. Example of FRETplexing PCR Result.

Using a standard RT-PCR machine I can perform multiplexed allelic-specific PCR assays that offer higher specificity and higher throughput, as multiple mutations would be identifiable simultaneously in each chamber. Assembling the fluorescence signals from each chamber would produce a high-resolution map that correlates the morphology with the genetic makeup of the KRAS mutation present in the sample. This mapping would allow for accurate and reliable stratification of patients.

PCR Multiplexing

State-of-the-art PCR coding is typically limited to one target per color for four colors, due to the spectral overlap of standard fluorophores. Some attempts [11-13] have been made to breach that barrier and code for more targets than available colors, but

those methods invariably bumped into the degeneracy problem: if more than one target sequence is present, the decoding is no longer unique, so the answer is ambiguous and generally useless. Our multiplexing technology [1] is the first to breach the supercolor barrier while ensuring completely non-degenerate and unambiguous decoding for any combination of targets present. In practical terms, it offers easy access to at least a 48-plex assay, compared to a maximal 3-plex under conventional coding. How the multiplex detection method works is that it can combine the use of color, multiplicity of signal intensity, and/or mathematical strategies to circumvent degeneracy and ensure an infinite number of unique codes that can be unambiguously decoded in any combination of occurrences. For example, in detecting a sample containing four analytes, each analyte can be assigned a fluorophore (blue, green, yellow, or red) and a quencher attached to analyte-specific oligonucleotides (e.g., a forward PCR primer and a reverse PCR primer). Upon amplification, the presence or absence of an analyte is determined based on the presence or absence of a signal in that particular color. Another example is based on color intensity, where each analyte is assigned a fluorescent intensity (1x, 2x, 4x etc), where 1x is the concentration of labeled primers used, and where combining the intensity generates a readable code that can be used to determine the presents of a given analyte. By taking the delta of a PCR reaction (blue arrow in Figure 6.3 and 6.4) we generate a fluorescent intensity, which ends up as linear combination of florescent intensities (1x plus 2x equals 3x, 4x plus 1x equals 5x); thus, this method is an important technological advance.

Allele-specific assays typically offer only one mutation to be identified per sample. The reason is that fluorophores have a wide emission spectra, which overlap and

cause false positives if more than four colors are used simultaneously. Thus, a mutation plus a positive control would take two of the available four colors. This is a severe restriction, especially since many mutations of the same gene can occur in the same sample. For example, there are at least eight KRAS mutations [9, 10] leading to drug resistance in colorectal cancer. As a stopgap measure, some commercial assays sacrifice identification and code multiple mutations in the same color, the rationale being that any targeted mutations present would produce a positive result and thus would mean drug resistance. However, this is woefully inadequate as mutation identification is critical in fundamental research and in the careful clinical stratification of patients. In contrast, using FRETplexing or quenchingplex methods multiple mutations can unambiguously be identified in each color or intensity together with a morphological confirmation, including with superior specificity and sensitivity.

Polymerase chain reactions

All PCR reactions were performed on a Roche 480 LightCycler I and II instrument (Roche Applied Science, Penzberg, Germany). The PCR cycling reaction was run for a minimum of 45 cycles, with a 180 sec hot-start at 95°C. The cycling conditions were as follows: denaturation for 10 sec at 95°C, annealing for 50 sec at 50°C, and detection for 12 sec at 72°C. Each experiment was run in groups of 12, with a reaction volume of 15µL. Fluorescence measurements in 523nm-568nm (Cy3) and 615nm-670nm (Cy5) were taken at the end of annealing for every cycle for quenchplex and excitation at 498nm with detection at 610-640nm for FRETplexing. The change in fluorescence intensity between the first and last measurements, for each instance of an experiment,

determined the quenched or FRET signal. Furthermore, a melt curve measurement was taken every degree between 58°C and 70°C.

Positive control experiments were performed to determine base-line quenching and FRET levels for each target and set of primers. The change in fluorescence intensity was used to assemble the expected cumulative signal levels in the delta graphs (example in Figure 6.4 and results Figure 6.25). In each case, the higher intensity count corresponded to a unique combination of present targets. The baseline concentration for a 1x count was determined by a set of fluorophore titration experiments. A 200nM 1x concentration of probes in the FAM channel allowed for a sufficiently strong signal that minimized cross-channel bleed through. The expected multiplicative signal levels were determined by multiplying this baseline by the multiplicity.

Results

Quenchiplexing

When trying to establish a new method there is no guarantee that the system will actually function as intended. Groups of STI were ordered to test the system (as seen in table 6.1). No parameters were determined yet the system was run using the parameters in table 6.2. Lambda DNA with primers was borrowed from David Baltimore to use as a control to determine if the PCR was functioning properly. The initial test result, displayed in Figure 6.5, revealed that the quenchiplexing assay does function properly, and the data from the PCR machine appears to be an inverse PCR graph. With the knowledge that the system functions I started to develop an assay to test for SNPs found in K-RAS mutations.

STI	Sequence	Forward Primer	Reverse Primer
Chlamydia	CAT TAG GAT TTA CGA AGG ATG GGA AGG TTT AAC TGA CGA AGA AAA TAT AGA TAT AGA CTT AAC ACC TTT TAA TTC ACC AC	/5Cy3/CAT TAG GAT TTA CGA AGG ATG GGA AGG TTT	/5IABkFQ/GTG GTG AAT TAA AAG GTG TTA AGT CTA TAT CTA TAT TTT CTT
HIV pol	AGC TAT AGG TAC AGT ATT AGT AGG ACC TAC ACC TGT CAA CAT AAT TGG AAG AAA	/5Cy3/AGC TAT AGG TAC AGT ATT AGT AGG ACC TAC ACC	/5IABkFQ/AAG TGC AAC CAA TCT GAG TCA ACA GAT TTC
Gonorrhea	TTT CAA AGA AGC GCC TAT GCT GGT GCG CTC TTA CGC TGC CGC CAT CAA ACG TCG CTA CAT CCA AGT CAA TCC GTC GCA TC	/5Cy3/TTT CAA AGA AGC GCC TAT GCT GGT	/5IABkFQ/GAT GCG ACG GAT TGA CTT GGA TGT
Syphilis	GAA GGG AAG CAG GTG TAG TCA TGG CGA CGG GAA ATA CTG TCT AAG GTT AGG TTG CAA GAG ACC GTA CCG CAA ACC GAC AC	/5Cy3/GAA GGG AAG CAG GTG TAG TCA TGG	/5IABkFQ/GTG TCG GTT TGC GGT ACG G

HIV gag	TTA ATC CTG GCC TGT TAG AAA CAT CAG AAG GCT GTA GAC AAA TAC TGG GAC AGC TAC AAC CAT CCC TTC AGA CAG GAT CA	/5Cy3/GCC TTC TGA TGT TTC TAA CAG GCC AGG ATT AA	/5IABkFQ/TGA TCC TGT CTG AAG GGA TGG TTG
Herpes Virus 2	TTC CGG CCG ACA CCC AGG AAA CAA CGA CGC GCC GGG CCC TTT ATA AAG AGA TAC GCG ATG CGT TGG GCA GTC GAA AAC AG	/5Cy3/TTC CGG CCG ACA CCC A	/5IABkFQ/CTG TTT TCG ACT GCC CAA CGC

Table 6.1. Sequence and Primers of STI Initial Test Panel for Quenichplexing Assay Development.

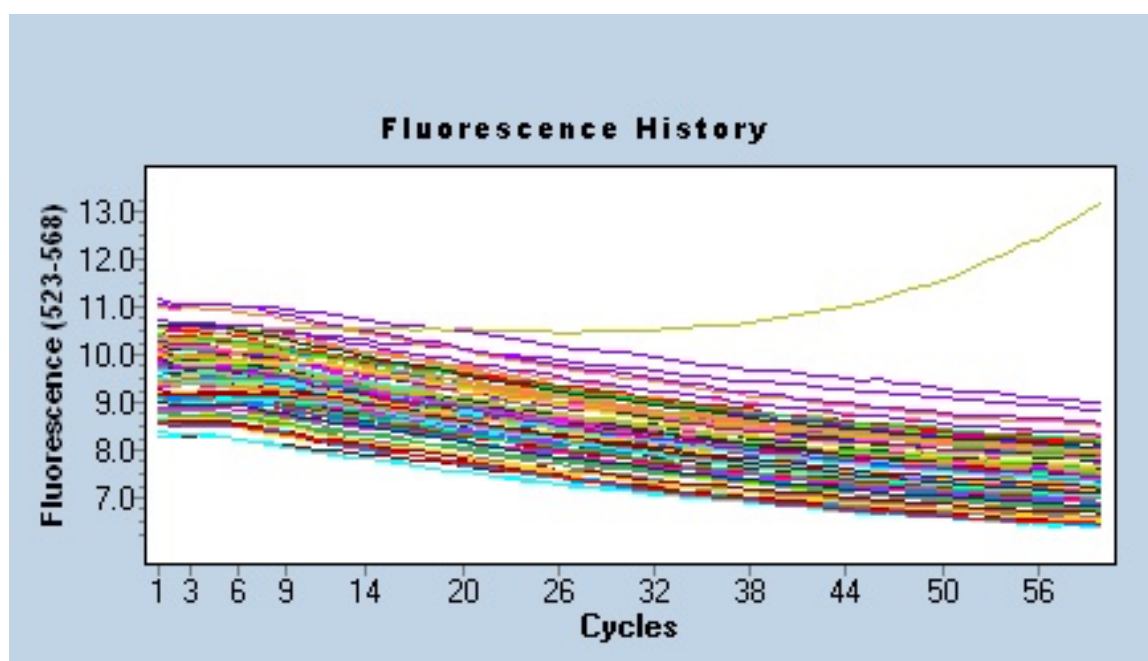


Figure 6.5. Initial PCR Machine Readout for the STI Test Experiment.

STI's	Sequence 10uM	Forward Primer 10uM	Reverse Primer 10um	Taq Master Mix 5x	H ₂ O
Volume	20uL	4uL	4uL	40uL	132uL

Table 6.2. Experimental Volumes and Concentrations used for the STI Initial Experimental Test.

Using the literature on the most common point mutations found in K-RAS related cancer and the NIH BLAST program, I designed specific forward primers for the top six most common point mutations (Tables 6.3 and 6.4), and used a generic reverse primer for all mutations, and wild type and mutant sequences for the first 99bp of the K-RAS gene. After several experiments to determine the lowest visible primer concentration (data not included) it was concluded that the lowest concentration visible was too low for reliable pipetting; as a result, the lowest primer volume used was 2uL, and because this is the 1x concentration, the 2x concentration is 4uL, 4x becomes 8uL, and so on till the system becomes saturated.

WT/Mutants	Sequence
WT	5'- ATG ACT GAA TAT AAA CTT GTG GTA GTT GGA GCT <u>GGT</u> GGC GTA GGC AAG AGT GCC TTG ACG ATA CAG CTA ATT CAG AAT CAT TTT GTG GAC -3'
216A	5'- ATG ACT GAA TAT AAA CTT GTG GTA GTT GGA GCT <u>GAT</u> GGC GTA GGC AAG AGT GCC TTG ACG ATA CAG CTA ATT CAG AAT CAT TTT GTG GAC -3'
216T	5'- ATG ACT GAA TAT AAA CTT GTG GTA GTT GGA GCT <u>GTT</u>

WT/Mutants	Sequence
	GGC GTA GGC AAG AGT GCC TTG ACG ATA CAG CTA ATT CAG AAT CAT TTT GTG GAC -3'
216C	5'- ATG ACT GAA TAT AAA CTT GTG GTA GTT GGA GCT <u>G</u> CT GGC GTA GGC AAG AGT GCC TTG ACG ATA CAG CTA ATT CAG AAT CAT TTT GTG GAC -3'
219A	5'- ATG ACT GAA TAT AAA CTT GTG GTA GTT GGA GCT GCT <u>G</u> AC GTA GGC AAG AGT GCC TTG ACG ATA CAG CTA ATT CAG AAT CAT TTT GTG GAC -3'
215A	5'- ATG ACT GAA TAT AAA CTT GTG GTA GTT GGA GCT <u>A</u> CT GGC GTA GGC AAG AGT GCC TTG ACG ATA CAG CTA ATT CAG AAT CAT TTT GTG GAC -3'
215T	5'- ATG ACT GAA TAT AAA CTT GTG GTA GTT GGA GCT <u>T</u> CT GGC GTA GGC AAG AGT GCC TTG ACG ATA CAG CTA ATT CAG AAT CAT TTT GTG GAC -3'

Table 6.3. Sequences Used for KRAS Mutation Experiments

KRAS mutation	Forward Primer	Reverse primer generic for all mutations	Reverse Primers 2 nd generation
216T	/ 5Cy3 /GAATATAAACTTGT GGTAGTTGGAGCTGT	/5IABkFQ/GTC CAC AAA ATG AAT CTG AAT TAG CTG	/ 5IABkFQ/ GTCCACAAAAT GAATCTGAAT
216C	/ 5Cy3 /GAATATAAACTTGT GGTAGTTGGAGCTG C		/ 5IABkFQ /GTCCACAAAAT GAATCTGAAT

KRAS mutation	Forward Primer	Reverse primer generic for all mutations	Reverse Primers 2nd generation
219A	/ 5Cy3 /GAATATAAACTTGT GGTAGTTGGAGCTG GTGA		/ 5IABkFQ /GTCCACAAAAT GAATCTGAAT
216A	/5Cy3/GAATATAAAC TTGTGGTAGTTGGAG CTGA		/5IABkFQ/GCA CTC TTG CCT ACG CCA T
215T	/5Cy3/GAATATAAAC TTGTGGTAGTTGGAG CTT		/5IABkFQ/CAC TCT TGC CTA CGC CAC A
215A	/5Cy3/GAATATAAAC TTGTGGTAGTTGGAG CTA		/5IABkFQ/CAC TCT TGC CTA CGC CAC T

Table 6.4. Sequence and Primers of KRAS Test Panel for Quenichiplexing Assay

Development.

Using the sequence information in Table 6.3 and the primer information from Table 6.4, K-RAS experiments were designed to test the ability of quenchiplexing to identify specific point mutations in the PCR machine. With the experimental design found in Table 6.5, each STI concentration was run independently with 24 replicates. The data from these experiments is found in Figure 6.6-6.11. Although the intensity scales in all the figures, which is expected in a intensity multiplexing assay, the quenchiplexing assay as currently designed was unsuccessful. The initial problem was the experimental and reverse primer design; by design a generic reverse primer that can hybridize with

both the mutant and wild type sequence was problematic. Even though the forward primer was specific and could only amplify at mutant sequence, the reverse primer was amplifying both the mutant and wild type sequences. This would most likely contribute to the linear quenching observed in Figures 6.6-6.11. Using the data from these experiments the reverse primer was redesigned to the 2nd generation reverse primer found in table 6.4.

STI Concentration	Mutant Sequence	Forward Primer	Reverse Primer	Taq 5x Master Mix	H ₂ O	Wild Type Sequence
1x	10uL	2uL	2uL	20uL	66uL	10uL
2x	10uL	4uL	4uL	20uL	62uL	10uL
4x	10uL	8uL	8uL	20uL	54uL	10uL
8x	10uL	16uL	16uL	20uL	38uL	10uL

Table 6.5. Experimental Protocol for KRAS Quenchiplxing Experiment.

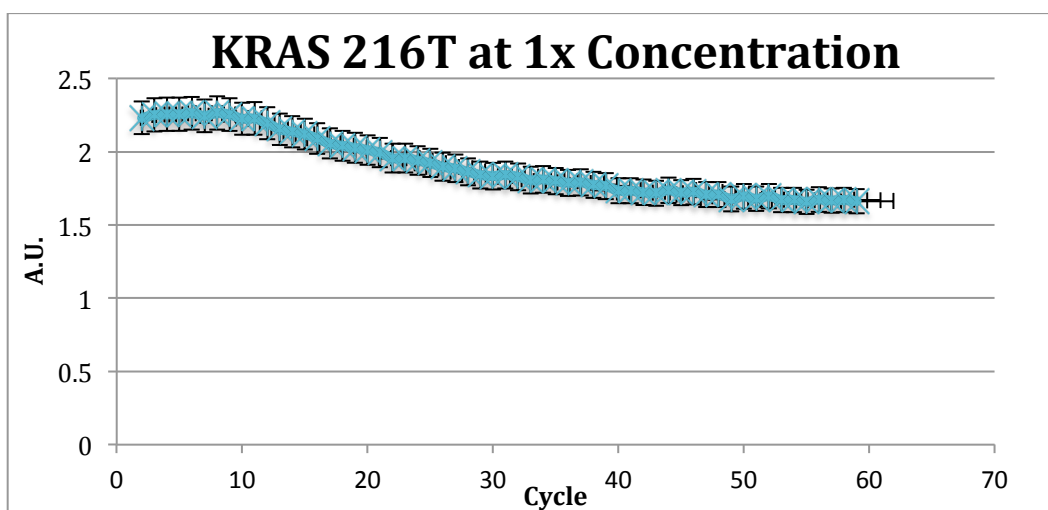


Figure 6.6. Quenchiplxing KRAS 216T at 1x Concentration. The chart shows averaged fluorescence emission signal of 18 qPCR replica experiments (at y-axis) plotted as a function of PCR cycles with a standard deviation of 1σ.

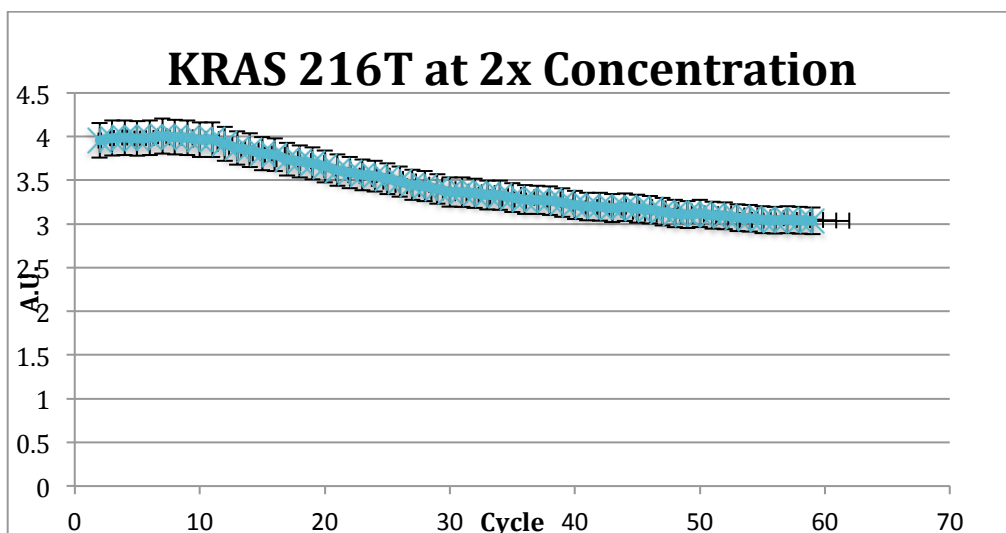


Figure 6.7. Quenchiplexing KRAS 216T at 2x Concentration. The chart shows averaged fluorescence emission signal of 18 qPCR replica experiments (at y-axis) plotted as a function of PCR cycles with a standard deviation of 1σ .

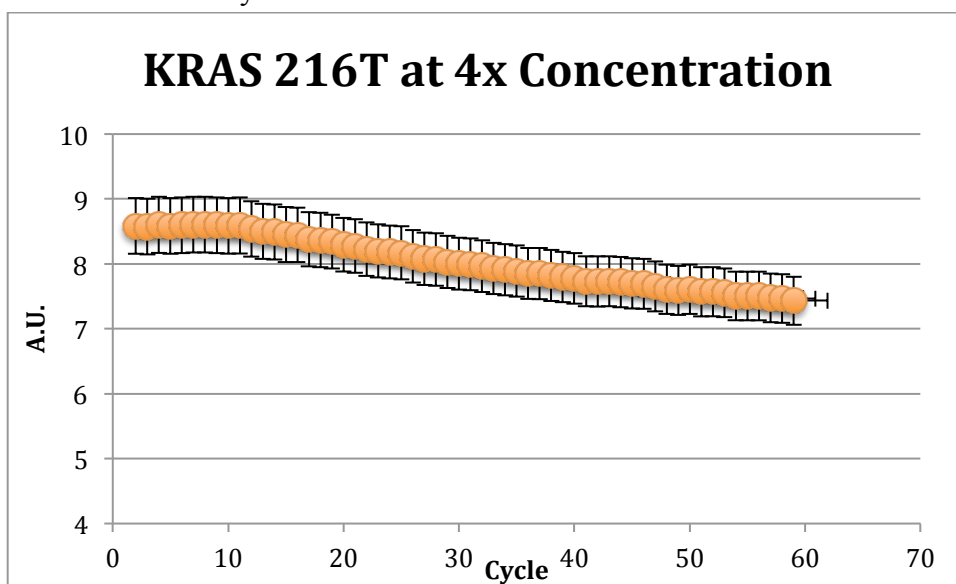


Figure 6.8. Quenchiplexing KRAS 216T at 4x Concentration. The chart shows averaged fluorescence emission signal of 18 qPCR replica experiments (at y-axis) plotted as a function of PCR cycles with a standard deviation of 1σ .

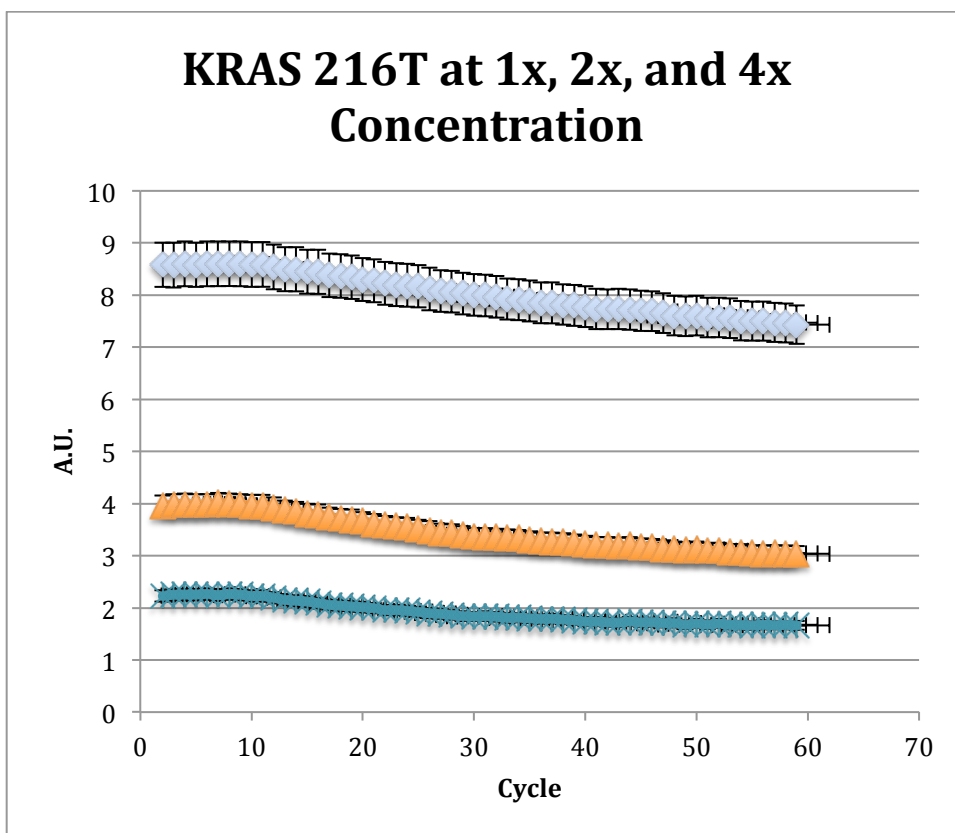


Figure 6.9. Quenchiplexing KRAS 216T at 1x, 2x, and 4x Concentration. The chart shows averaged fluorescence emission signal of 18 qPCR replica experiments (at y-axis) plotted as a function of PCR cycles with a standard deviation of 1σ .

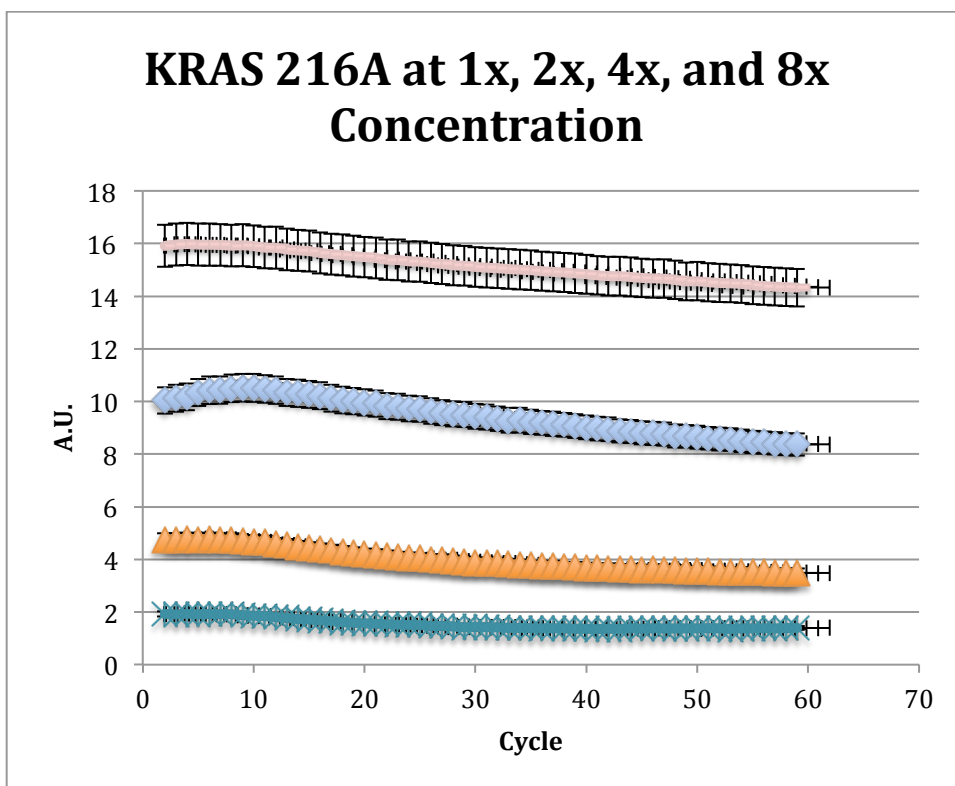


Figure 6.10. Quenchiplxing KRAS 216A at 1x, 2x, 4x, and 8x Concentration. The chart shows averaged fluorescence emission signal of 18 qPCR replica experiments (at y-axis) plotted as a function of PCR cycles with a standard deviation of 1σ .

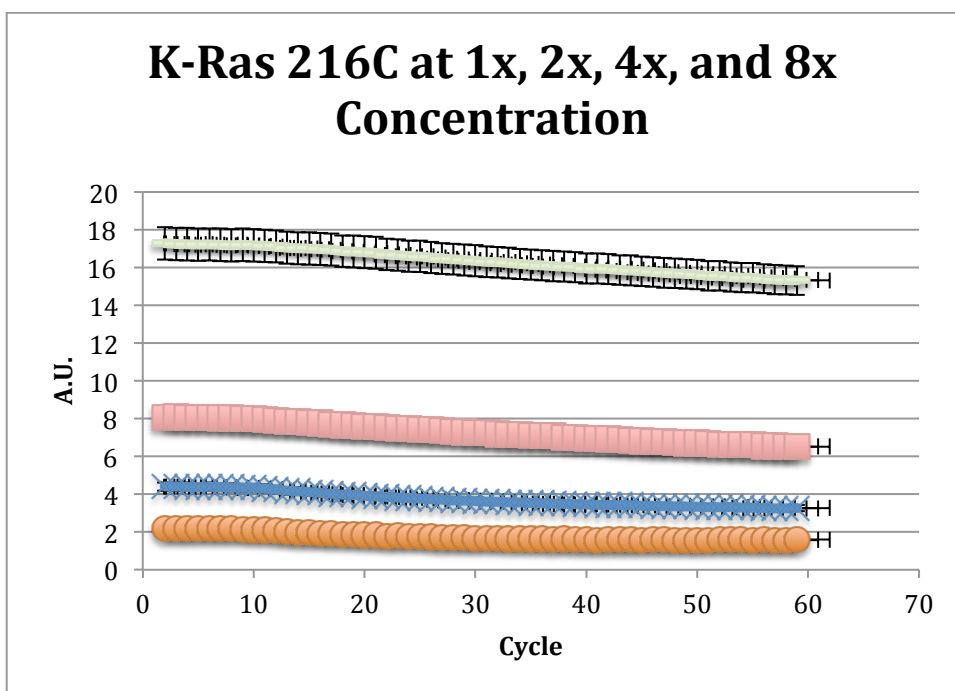


Figure 6.11. Quenchiploting KRAS 216C at 1x, 2x, 4x, and 8x Concentration. The chart shows averaged fluorescence emission signal of 18 qPCR replica experiments (at y-axis) plotted as a function of PCR cycles with a standard deviation of 1σ .

Using the information acquired from the failed quechiploting experiment new experiments were designed, as seen in Tables 6.6-6.8. The same PCR and replicates were used as the prior experiment, and the only change is the reverse primer. The resulting data was used to generate Figures 6.13-6.14. Unlike the earlier experiments there is more of an iconic inverse PCR graph generated, which is the desired result. When examining the deltas of each graph, values of 0.4A.U for 1x concentration, 0.8A.U. for 2x concentration and around 1.6A.U for 4x concentration are generated. This proves that the quenchiploting assay works and it is possible to use intensity coding with quenchiploting for multiplexing assays. With the assay validated to perform as designed, experiments were performed to test the combination of mutation concentrations to generate the 3x, 5x, 6x, and 7x concentrations, which should result by adding the different primer combinations together.

Components	Volume (uL)/Concentration(uM)
Reagents	20uL of 100 uM Taq 5x maternix
WT	10uL of 100uM
216C	10uL of 10uM
216C primer 1x	2 uL of 10uM forward and reverse primer

Table 6.6. Experiment Cocktail for Quenchiploting Detection of a Single 216C Mutation.

Components	Volume (uL)/Concentration(uM)
Reagents	20uL of 100 uM Taq 5x maternix
WT	10uL of 100uM

Components	Volume (uL)/Concentration(uM)
216T	10uL of 10uM
216T primer 2×	4 uL of 10uM forward and reverse primer

Table 6.7. Experiment Cocktail for Quenchiplexing Detection of a Single 216T Mutation.

Components	Volume (uL)/Concentration(uM)
Reagents	20uL of 100 uM Taq 5x maternix
WT	10uL of 100uM
216A	10uL of 10uM
216A primer 4×	48uL of 10uM forward and reverse primer

Table 6.8. Experiment Cocktail for Quenchiplexing Detection of a Single 216A Mutation.

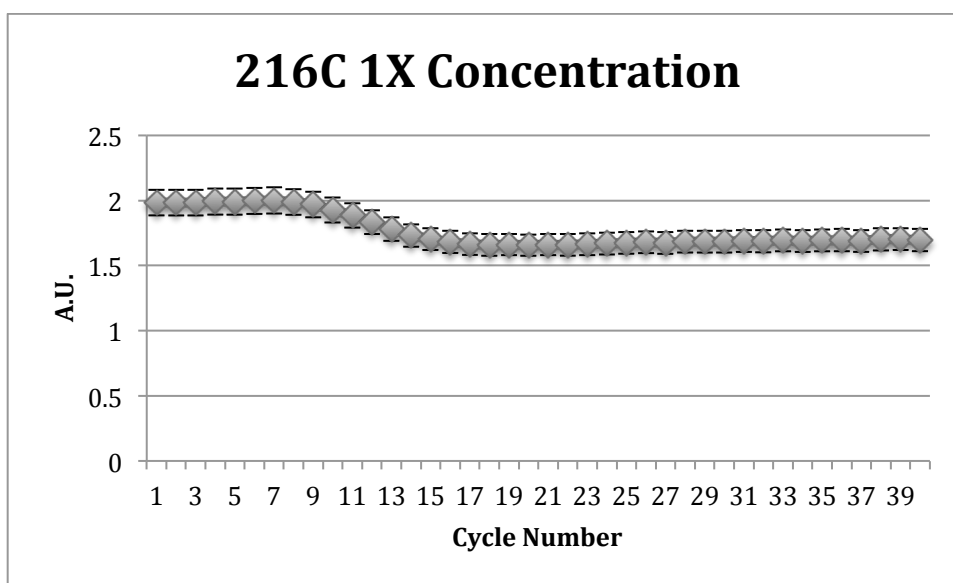


Figure 6.12. Improved Quenchiplexing Assay for 216C at 1x Concentration. Chart reporting detection of 216C mutant sequence from the KRAS gene using quenchiplexing with qPCR. The multiplexed assay contains 0.5uL of 10uM forward and reverse primer concentration, 20uL of Taq 5x maternix, and 10uL of 10uM mutant 216C. The forward primer is labeled with Cy3 as a fluorophore and the reverse primer is labeled with IABkFQ as a quencher. The chart shows averaged fluorescence emission signal of 12 qPCR replica experiments (at y-axis) plotted as a function of PCR cycles with a standard deviation of 1σ . The amplification phase starts at cycle 8 and the saturation phase at cycle 18.

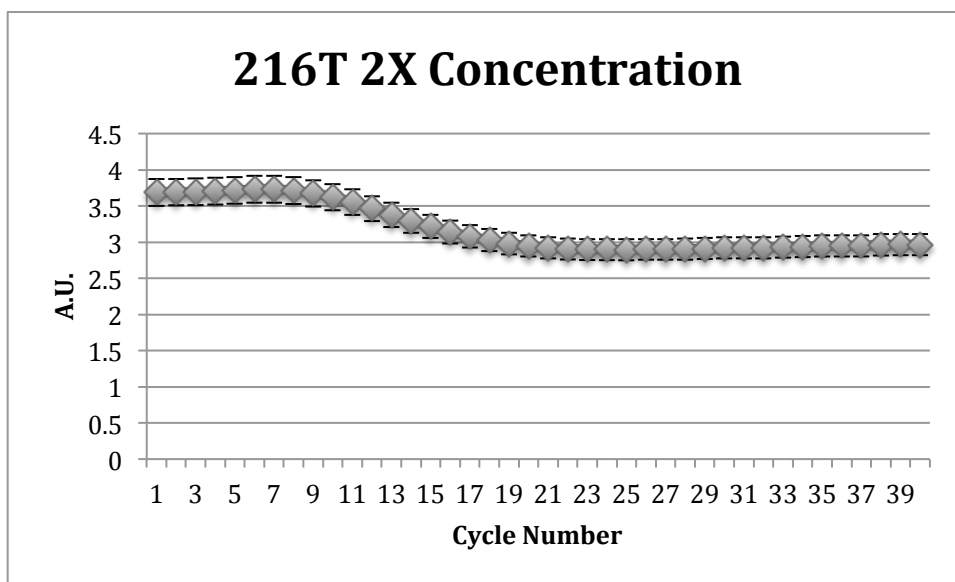


Figure 6.13. Improved Quenchiploting Assay for 216T at 2x Concentration. Chart reporting detection of 216T mutant sequence from the KRAS gene using quenchiploting with qPCR. The multiplexed assay contains 1uL of 10uM forward and reverse primer concentration, 20uL of Taq 5x maternix, and 10uL of 10uM mutant 216T. The forward primer is labeled with Cy3 as a fluorophore and the reverse primer is labeled with lABkFQ as a quencher. The chart shows averaged fluorescence emission signal of 12 qPCR replica experiments (at y-axis) plotted as a function of PCR cycles with a standard deviation of 1σ .

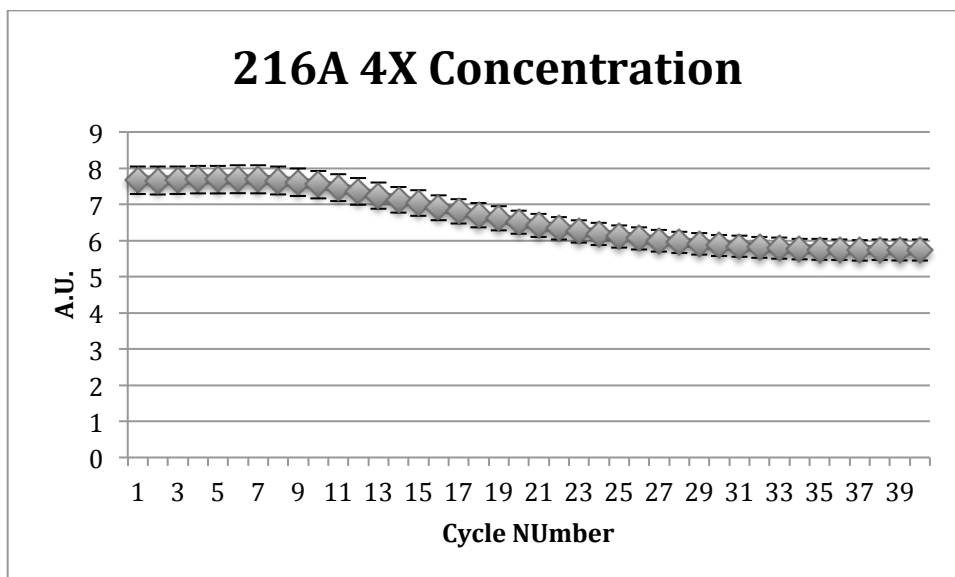


Figure 6.14. Improved Quenchiploting Assay for 216A at 4x Concentration. Chart reporting detection of 216A mutant sequence from the KRAS gene using quenchiploting with qPCR. The multiplexed assay contains 2uL of 10uM forward and reverse primer concentration, 20uL of Taq 5x maternix, and 10uL of 10uM mutant 216A. The forward

primer is labeled with Cy3 as a fluorophore and the reverse primer is labeled with lABkFQ as a quencher. The chart shows averaged fluorescence emission signal of 12 qPCR replica experiments (at y-axis) plotted as a function of PCR cycles with a standard deviation of 1σ .

By slightly modifying the experimental reagents I combined multiple mutations in a single reaction to observe the multiplexing behavior of the assay. The experimental protocols are displayed in Tables 6.9-6.12 and the resulting data is graphed in figures 6.15-6.18. Similar to the first failed experiments, there is a loss of the iconic inverse PCR graph (Figures 6.15-6.18). The theory behind why the experiment failed is a unique case for this system; all the sequences and primers share a high degree of similarity, with just one or two base pair difference, and as a result it is difficult for primers to hybridize with the correct target due to the high degree of similarity. As the PCR experiment proceeds this problem only increases, since there are more sequences to hybridize and the probability of finding the correct target gets further reduced. In addition to the statistical problem, the high degree of similarity will not encourage the incorrect sequence to decouple with the incorrect target. This would not be a problem with the STI sequences tested earlier, since their sequences have a low level of similarity, yet for KRAS mutations and the sequences similarity, this is problematic. Even with these problems the assays high degree of specificity, when amplifying a target sequences, provided a useful diagnostic application for this assay.

Components	Concentration	Volume
Reagents	100uM	20uL
WT	100uM	10uL
216C	10uM	10uL

216T	10uM	10uL
216T Primer	10uM	4uL
216C Primer	10uM	2uL

Table 6.9. Experiment Cocktail for Quenchiplexing Detection of a Double Mutation 216T at 2× and 216C at 1× Primer Concentrations.

Components	Concentration	Volume
Reagents	100uM	20uL
WT	100uM	10uL
216T	10uM	10uL
216A	10uM	10uL
216T Primer	10uM	4uL
216A Primer	10uM	8uL

Table 6.10. Experiment Cocktail for Quenchiplexing Detection of a Double Mutation 216T at 2× and 216A at 4× Primer Concentrations.

Components	Concentration	Volume
Reagents	100uM	40uL
WT	100uM	10uL
216C	10uM	10uL
216A	10uM	10uL
216C Primer	10uM	2uL
216A Primer	10uM	8uL

Table 6.11. Experiment Cocktail for Quenchiplexing Detection of a Double Mutation 216C at 1× and 216A at 4× Primer Concentrations.

Components	Concentration	Volume
Reagents	100uM	40uL
WT	100uM	10uL
216C	10uM	10uL
216T	10uM	10uL
216A	10uM	10uL
216T Primer	10uM	4uL
216C Primer	10uM	2uL
216A Primer	10uM	8uL

Table 6.12. Experiment Cocktail for Quenchiplexing Detection of a Triple Mutation 216T at 2 \times and 216C at 1 \times and 216A at 4 \times Primer Concentrations.

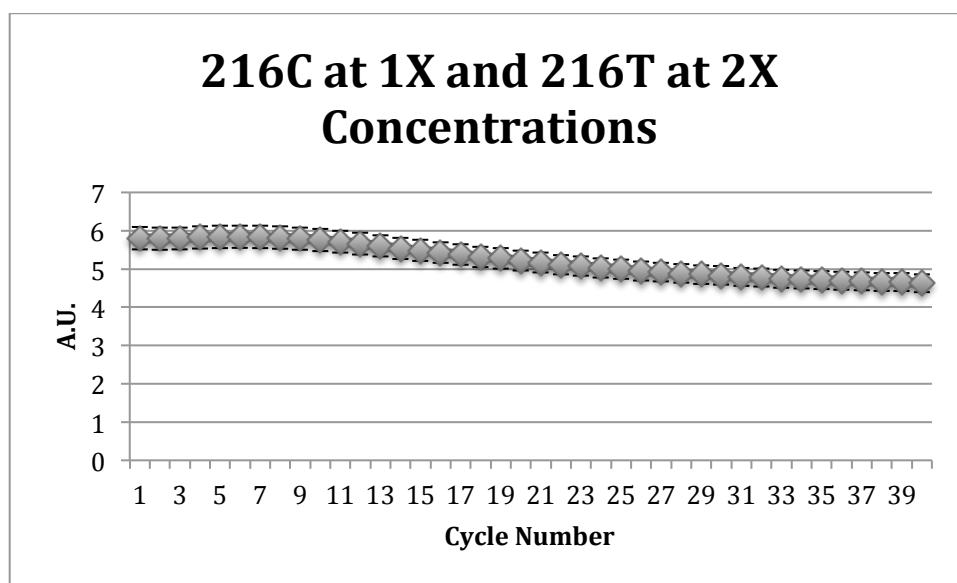


Figure 6.15. Improved Quenchiplexing Assay for 216C at 1x and 216T at 2x Concentration. Chart reporting detection of 216C and 216T mutant sequence from the K-RAS gene using quenchiplexing with qPCR. The multiplexed assay contains 0.5uL of 10uM forward and reverse primer concentration for 216C, 1uL of 10uM forward and reverse primer concentration for 216T, 20uL of Taq 5x mastermix, 10uL of 10uM mutant 216C, and 10uL of 10uM 216T. The forward primer is labeled with Cy3 as a fluorophore

and the reverse primer is labeled with LABkFQ as a quencher. The chart shows the averaged fluorescence emission signal of 12 qPCR replica experiments (at y-axis) plotted as a function of PCR cycles with a standard deviation of 1σ .

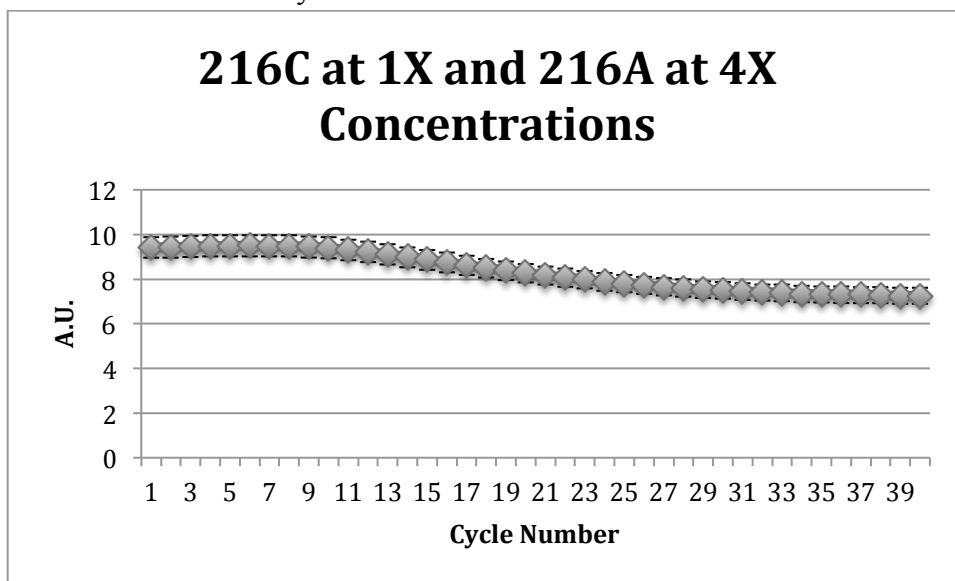


Figure 6.16. Improved Quenchiplexing Assay for 216C at 1x and 216A at 4x Concentration. Chart reporting detection of 216C and 216A mutant sequence from the K-RAS gene using quenchiplexing with qPCR. The multiplexed assay contains 0.5uL of 10uM forward and reverse primer concentration for 216A, 2uL of 10uM forward and reverse primer concentration for 216T, 20uL of Taq 5x matremix, 10uL of 10uM mutant 216C, and 10uL of 10uM 216A. The forward primer is labeled with Cy3 as a fluorophore and the reverse primer is labeled with LABkFQ as a quencher. The chart shows the averaged fluorescence emission signal of 12 qPCR replica experiments (at y-axis) plotted as a function of PCR cycles with a standard deviation of 1σ .

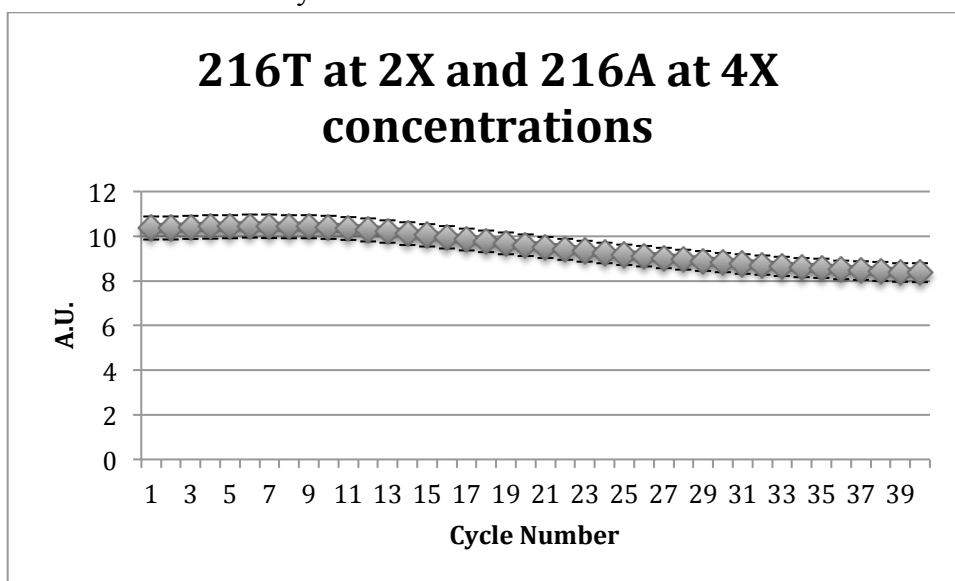


Figure 6.17. Improved Quenchiplexing Assay for 216T at 2x and 216A at 4x Concentration. Chart reporting detection of 216T and 216A mutant sequence from the K-RAS gene using quenchiplexing with qPCR. The multiplexed assay contains 1uL of 10uM forward and reverse primer concentration for 216T, 2uL of 10uM forward and reverse primer concentration for 216A, 20uL of Taq 5x mastermix and 10uL of 10uM mutant 216T, and 10uL of 10uM 216A. The forward primer is labeled with Cy3 as a fluorophore and the reverse primer is labeled with LABkFQ as a quencher. The chart shows the averaged fluorescence emission signal of 12 qPCR replica experiments (at y-axis) plotted as a function of PCR cycles with a standard deviation of 1σ .

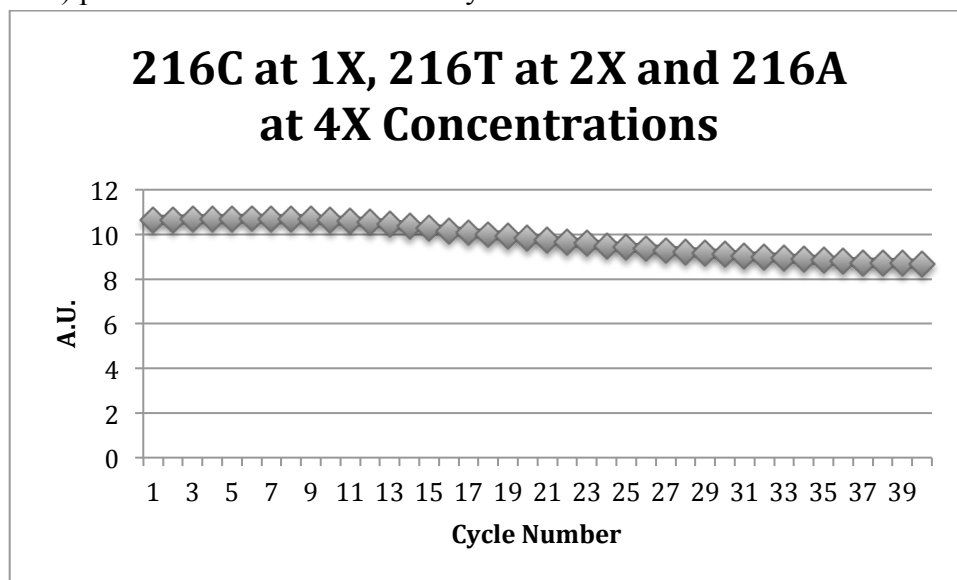


Figure 6.18.Improved Quenchiplexing Assay for 216C at 1x, 216T at 2x, and 216A at 4x Concentration. Chart reporting detection of 216C, 216T, and 216A mutant sequence from the KRAS gene using quenchiplexing with qPCR. The multiplexed assay contains 0.5uL of 10uM forward and reverse primer concentration for 216C, 1uL of 10uM forward and reverse primer concentration for 216T, 2uL of 10uM forward and reverse primer concentration for 216A, 20uL of Taq 5x maternmix, and 10uL of 10uM for each mutant 216C, 216T, and 216A. The forward primer is labeled with Cy3 as a fluorophore and the reverse primer is labeled with LABkFQ as a quencher. The chart shows the averaged fluorescence emission signal of 12 qPCR replica experiments (at y-axis) plotted as a function of PCR cycles with a standard deviation of 1σ .

KRAS mutation	Forward Primer	Reverse Primers 1 st generation	Reverse Primers 2 nd generation	Reverse Primers 3 rd generation
216A	/5Cy3/GAATATAA ACTTGTGGTAGTT GGAGCTGA	/5Cy5/GCACT CTTGCCTAC GCCAT	/56-FAM/AAT ATA AAC TTG TGG TAG TTG GAG CTG A	/5LtC640N/GCA CTC TTG CCT ACG CCA T
216T	/5Cy3/GAATATAA ACTTGTGGTAGTT GGAGCTGT	/5Cy5/GCACT CTTGCCTAC GCCAA	/56-FAM/AAT ATA AAC TTG TGG TAG TTG GAG CTG T	/5LtC640N/GCA CTC TTG CCT ACG CCA A
216C	/5Cy3/GAATATAA ACTTGTGGTAGTT GGAGCTGC	/5Cy5/GCACT CTTGCCTAC GCCAG	/56-FAM/AAT ATA AAC TTG TGG TAG TTG GAG CTG C	/5LtC640N/GCA CTC TTG CCT ACG CCA G
219A	/5Cy3/GAATATAA ACTTGTGGTAGTT GGAGCTGGTGA	/5Cy5/TCAAG GCACTCTTG CCTACGT	/56-FAM/AAT ATA AAC TTG TGG TAG TTG GAG CTG GTG A	/5LTC640N/GCA CTC TTG CCT ACG T
215A	/5Cy3/GAATATAA ACTTGTGGTAGTT GGAGCTA	/5Cy5/CACTC TTGCCTACG CCACT	/56-FAM/AAT ATA AAC TTG TGG TAG TTG GAG CTA	/5LTC640N/GCA CTC TTG CCT ACG CCA CT
215T	/5Cy3/GAATATAA ACTTGTGGTAGTT GGAGCTT	/5Cy5/CACTC TTGCCTACG CCACA	/56-FAM/AAT ATA AAC TTG TGG TAG TTG GAG CTT	/5LTC640N/GCA CTC TTG CCT ACG CCA CA

Table 6.13. Sequences of Primers for KRAS FRETplexing Assay Development.

FRETplexing

There are three significant problems with quechipllexing that are corrected by utilizing the FRETplexing assay. The first problem is generating a negative assay. Most experiments generate a positive response, so generating a negative response might be problematic to some. The second significant problem with quechipllexing is measuring a decrease in signal, assuming that it is the result of quenching, but that might not be the case; there are several things that absorb light, both biological and material, that can result in false quenching. The third problem is sensitivity. Many tools are used to detect trace amount of light, down to a single photon, yet it is significantly more difficult to detect the difference between a large starting number of photons and a slight reduction of photons. To help remedy these problems FRETplexing was developed. With FRETplexing you generate a positive response that is nearly identical to an iconic PCR response and with FRETplexing you eliminate the false positive generated for unexpected quenching. It is also unlikely that something in the system will cause the fluoraphore to activate with the optical filters in place to block specific spectral ranges. With FRET detection dependent on measuring fluorescence the systems in place are already designed for this kind of detection, increasing the sensitivity compared to quenchiplxing.

The primers used for the FRET system are displayed in Table 6.13; the multiple generations of primers were optimizing the primers for the commercial system. To ensure that FRETplexing works the same as quechipllexing the experiments were duplicated (table 6.14-6.15). The same PCR and replicates was used as the experiment before, the only change is the reverse primer having a fluoraphore. The resulting data was used to

generate Figures 6.19-6.20. As expected an iconic PCR graph was generated, which is the desired result. When examining the deltas of each graph we get values of 0.3A.U for 1x concentration. This proves that like quenchplexing, FRETplexing assay works and it is possible to use intensity coding with quenchplexing for multiplexing assays. Since the was validated and confirmed, it was time to test the combination of mutation concentrations to generate the 3x, 5x, 6x, and 7x concentrations that should result by adding the different primer combinations together.

Components	Volume (uL)/Concentration(uM)
Reagents	20uL of 100 uM Taq 5x maternix
WT	10uL of 100uM
216T	10uL of 10uM
216T primer 1×	2 uL of 10uM forward and reverse primer

Table 6.14. Experiment Cocktail for Detection of a Single 216T Mutation Using FRETplexing.

Components	Volume (uL)/Concentration(uM)
Reagents	20uL of 100 uM Taq 5x maternix
WT	10uL of 100uM
216C	10uL of 10uM
216C primer 2×	4 uL of 10uM forward and reverse primer

Table 6.15. Experiment Cocktail for Detection of a Single 216C Mutation Using FRETplexing.

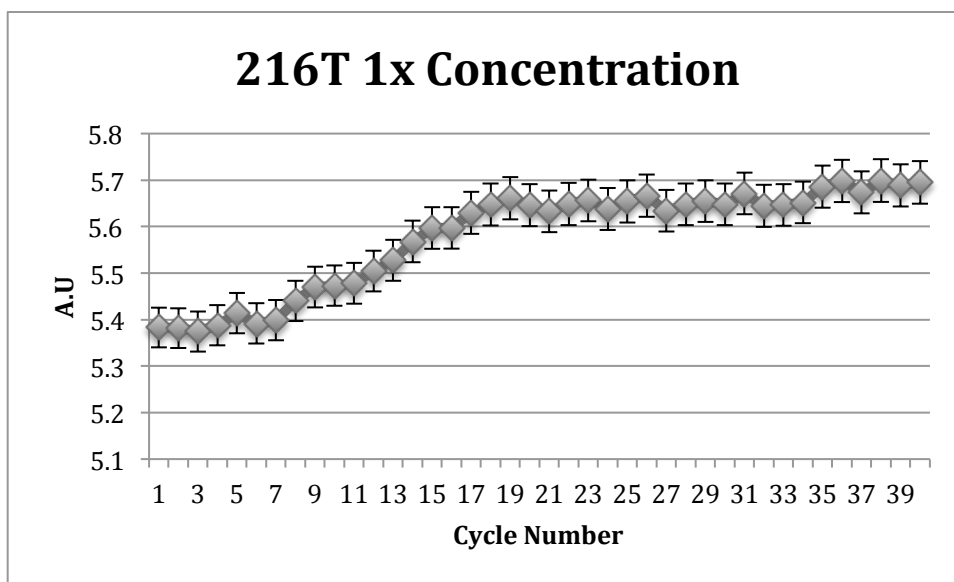


Figure 6.19. FRETplexing Assay for 216T 1x Concentration. Chart reporting detection of 216T mutant sequence from KRAS gene using FRET-chromophore-labeled primers with quantitative PCR (qPCR). The assay contains 2uL of 10uM forward and reverse primer concentration, 20uL of Taq 5x mastermix, 10uL of 10uM 216T mutant sequence, and 10uL of 100uM wild type sequence. The forward primer is labeled with Cy3 as a FRET donor chromophore and the reverse primer is labeled with Cy5 as a FRET acceptor chromophore. The chart shows an averaged FRET emission signal intensity of 10 qPCR experiments (y-axis) plotted as a function of PCR cycles (x-axis) with a standard deviation of 1σ . The FRET emission signal intensity is generated by Cy5 (y-axis) and detected after each annealing step. The delta value calculated by subtracting the maximum FRET signal recorded during the PCR saturation period and the minimum FRET signal recorded at the beginning of the PCR cycles is 0.27 A.U. The PCR reaction system reaches saturation at cycle 19 and the exponential growth begins at cycle 8.

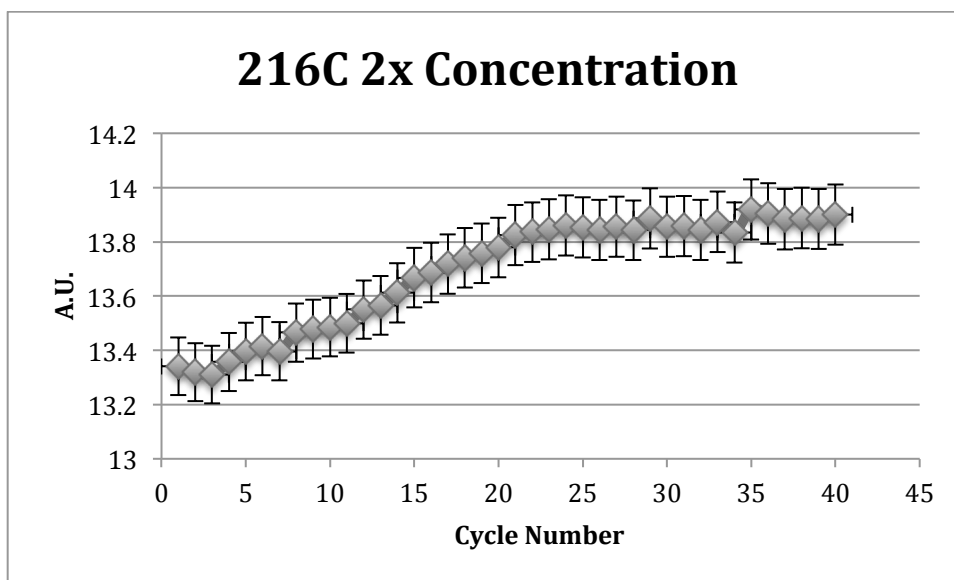


Figure 6.20. FRETplexing Assay for 216T 2x Concentration. Chart reporting detection of 216C mutant sequence from KRAS gene using FRET-chromophore-labeled primers with quantitative PCR (qPCR). The assay contains 4uL of 10uM forward and reverse primer concentration, 20uL of Taq 5x mastermix, 10uL of 10uM 216C mutant sequence and 10uL of 100uM wild type sequence. The forward primer is labeled with Cy3 as a FRET donor chromophore and the reverse primer is labeled with Cy5 as a FRET acceptor chromophore. The chart shows an averaged FRET emission signal intensity of 10 qPCR replica experiments (y-axis) plotted as a function of PCR cycles (x-axis) with a standard deviation of 1σ . The FRET emission signal intensity is generated by Cy5 (y-axis) and detected after each annealing step.

Repeating the experiment from the quenchplexing assay reagents I combined multiple mutations in a single reaction to observe the multiplexing behavior of the assay. The experimental protocols are displayed in Tables 6.16-6.19 and the resulting data is graphed in Figures 6.21-6.24. Using the data from the graphs 6.21-6.24 and using the single mutation experiments (Figure 6.19 and 6.20) deltas were determined and graphed in Figure 6.25. Using the generated delta, a graph can visualize the ability of the FRETplex assay to multiplex K-RAS mutations. The delta graph should in theory be linear and Figure 6.25 does tend to be linear, but once the concentration reaches the 6x level the system start to loose linearity. This is not surprising since, as expressed before, the sequence and primers have a high degree of similarity, creating a statistical problem.

Components	Concentration	Volume
Reagents	100uM	20uL
WT	100uM	10uL
216C	10uM	10uL
216T	10uM	10uL
216C Primer	10uM	4uL
216T Primer	10uM	2uL

Table 6.16. Experiment Cocktail for Detection of a Double Mutation 216C at 2x and 216T at 1x Primer Concentrations Using FRETplexing.

Components	Concentration	Volume
Reagents	100uM	20uL
WT	100uM	10uL
216C	10uM	10uL
216A	10uM	10uL
216C Primer	10uM	4uL
216A Primer	10uM	8uL

Table 6.17. Experiment Cocktail for Detection of a Double Mutation 216C at 2× and 216A at 4× Primer Concentrations Using FRETplexing.

Components	Concentration	Volume
Reagents	100uM	40uL
WT	100uM	10uL
216T	10uM	10uL
216A	10uM	10uL
216T Primer	10uM	2uL
216A Primer	10uM	8uL

Table 6.18. Experiment Cocktail for Detection of a Double Mutation 216T at 1× and 216A at 4× Primer Concentrations Using FRETplexing.

Components	Concentration	Volume
Reagents	100uM	40uL
WT	100uM	10uL
216C	10uM	10uL
216T	10uM	10uL

216A	10uM	10uL
216C Primer	10uM	4uL
216T Primer	10uM	2uL
216A Primer	10uM	8uL

Table 6.19. Experiment Cocktail for Detection of a Triple Mutation 216C at 2× and 216T at 1× and 216A at 4× Primer Concentrations Using FRETplexing.

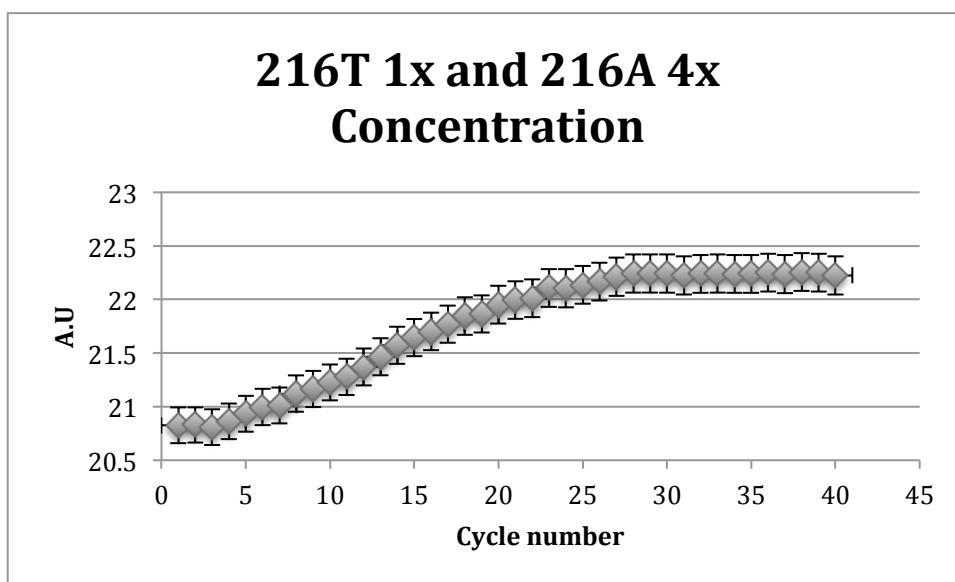


Figure 6.21. FRETplexing Assay for 216T at 1x and 216A at 4x Concentration. Chart reporting detection of double mutation 216T and 216A from KRAS gene using FRET-chromophore-labeled primers with quantitative PCR (qPCR). The assay contains 8uL of 10uM forward and reverse primer concentration for 216A, 2uL of 10uM forward and reverse primer concentration for 216T, 20uL of Taq 5x mastermix, 10uL of 10uM for each 216A and 216T mutant, and 10uL of 100uM wild type sequence. The forward primer is labeled with Cy3 as a FRET donor chromophore and the reverse primer is labeled with Cy5 as a FRET acceptor chromophore. The chart shows an averaged FRET emission signal intensity of 10 qPCR replica experiments (y-axis) plotted as a function of PCR cycles (x-axis) with a standard deviation of 1σ. The FRET emission signal intensity is generated by Cy5 (y-axis) and detected after each annealing step.

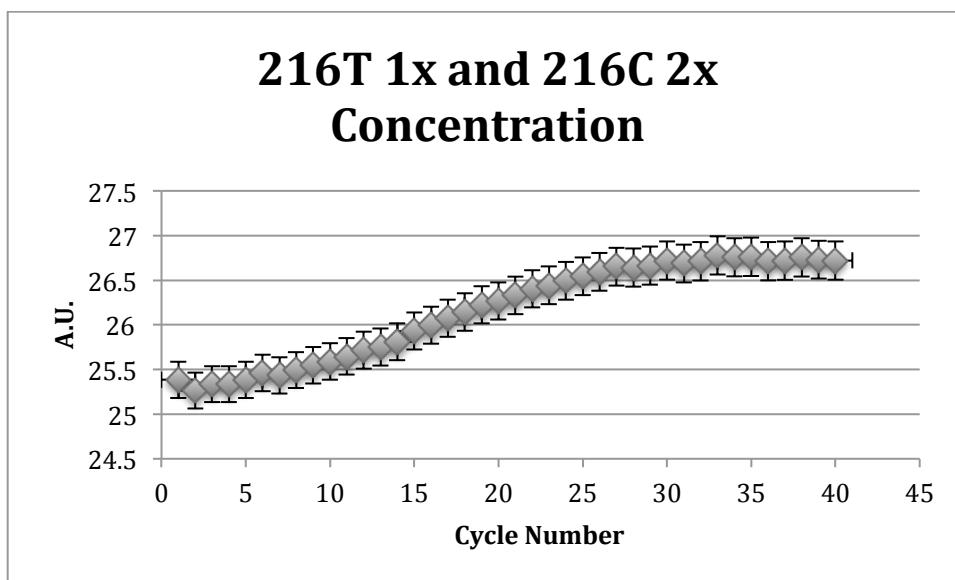


Figure 6.22. FRETplexing Assay for 216T at 1x and 216C at 2x Concentration. Chart reporting detection of double mutation 216T and 216C from KRAS gene using FRET-chromophore-labeled primers with quantitative PCR (qPCR). The assay contains 4uL of 10uM forward and reverse primer concentration for 216C, 2uL of 10uM forward and reverse primer concentration for 216T, 20uL of Taq 5x mastermix, 10uL of 10uM for each 216C and 216T mutant, and 10uL of 100uM wild type sequence. The forward primer is labeled with Cy3 as a FRET donor chromophore and the reverse primer is labeled with Cy5 as a FRET acceptor chromophore. The chart shows an averaged FRET emission signal intensity of 10 qPCR replica experiments (y-axis) plotted as a function of PCR cycles (x-axis) with a standard deviation of 1σ . The FRET emission signal intensity is generated by Cy5 (y-axis) and detected after each annealing step.

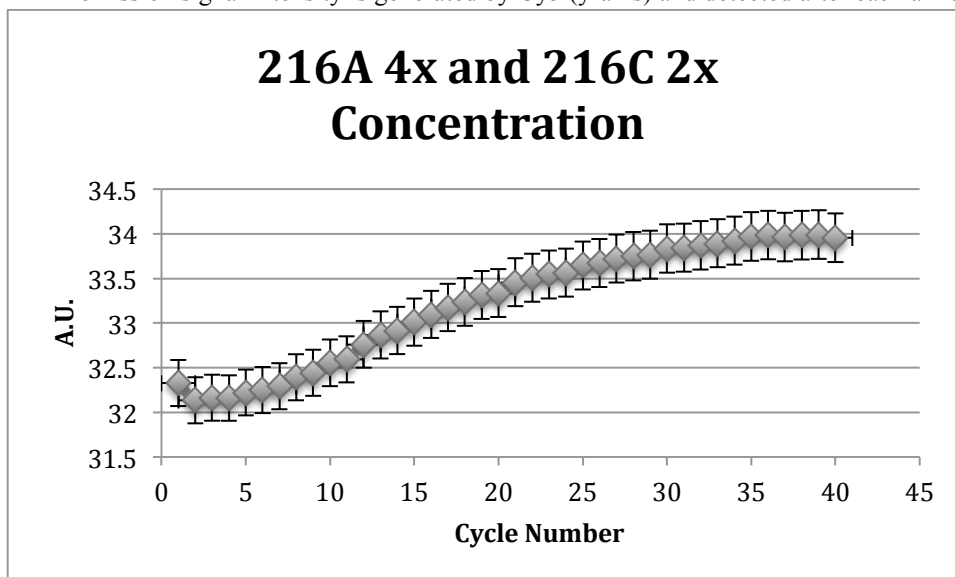


Figure 6.23. FRETplexing Assay for 216A at 4x and 216C at 2x Concentration. Chart reporting detection of double mutation 216A and 216C from KRAS gene using FRET-chromophore-labeled primers with quantitative PCR (qPCR). The assay contains 4uL of 10uM forward and reverse primer concentration for 216C, 8uL of 10uM forward and reverse primer concentration for 216A, 20uL of Taq 5x mastermix, 10uL of 10uM for each 216A and 216C mutant, and 10uL of 100uM wild type sequence. The forward primer is labeled with Cy3 as a FRET donor chromophore and the reverse primer is labeled with Cy5 as a FRET

acceptor chromophore. The chart shows an averaged FRET emission signal intensity of 10 qPCR replica experiments (y-axis) plotted as a function of PCR cycles (x-axis) with a standard deviation of 1σ . The FRET emission signal intensity is generated by Cy5 (y-axis) and detected after each annealing step.

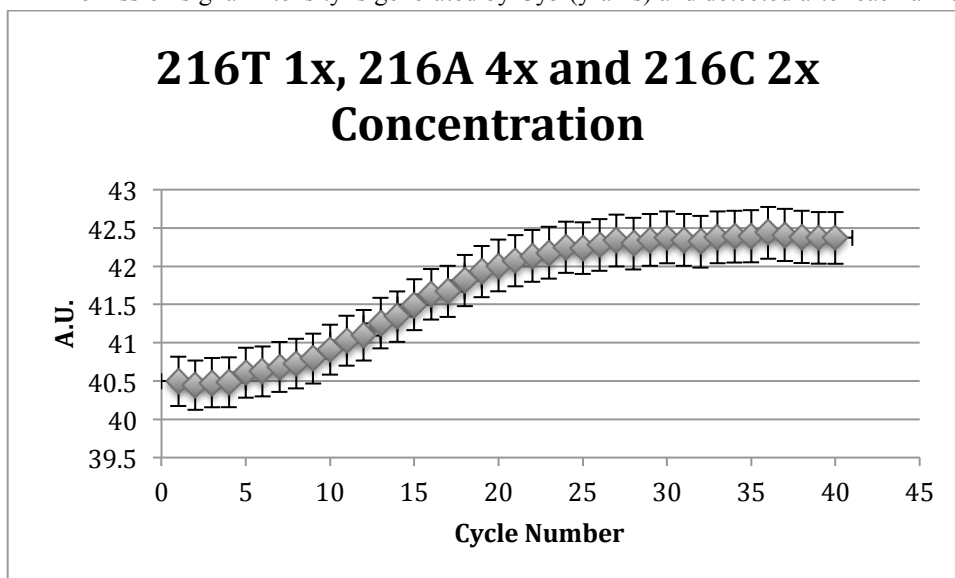


Figure 6.24 FRETplexing Assay for 216T at 1x, 216A at 4x and 216C at 2x Concentration. Chart reporting detection of triple mutation 216A, 216T and 216C from KRAS gene using FRET-chromophore-labeled primers with quantitative PCR (qPCR). The assay contains 4uL of 10uM forward and reverse primer concentration for 216C, 8uL of 10uM forward and reverse primer concentration for 216A, 2uL of 10uM forward and reverse primer concentration for 216T, 20uL of Taq 5x mastermix, 10uL of 10uM for each 216A, 216T and 216C mutant, and 10uL of 100uM wild type sequence. The forward primer is labeled with Cy3 as a FRET donor chromophore and the reverse primer is labeled with Cy5 as a FRET acceptor chromophore. The chart shows an averaged FRET emission signal intensity of 10 qPCR replica experiments (y-axis) plotted as a function of PCR cycles (x-axis) with a standard deviation of 1σ . The FRET emission signal intensity is generated by Cy5 (y-axis) and detected after each annealing step.

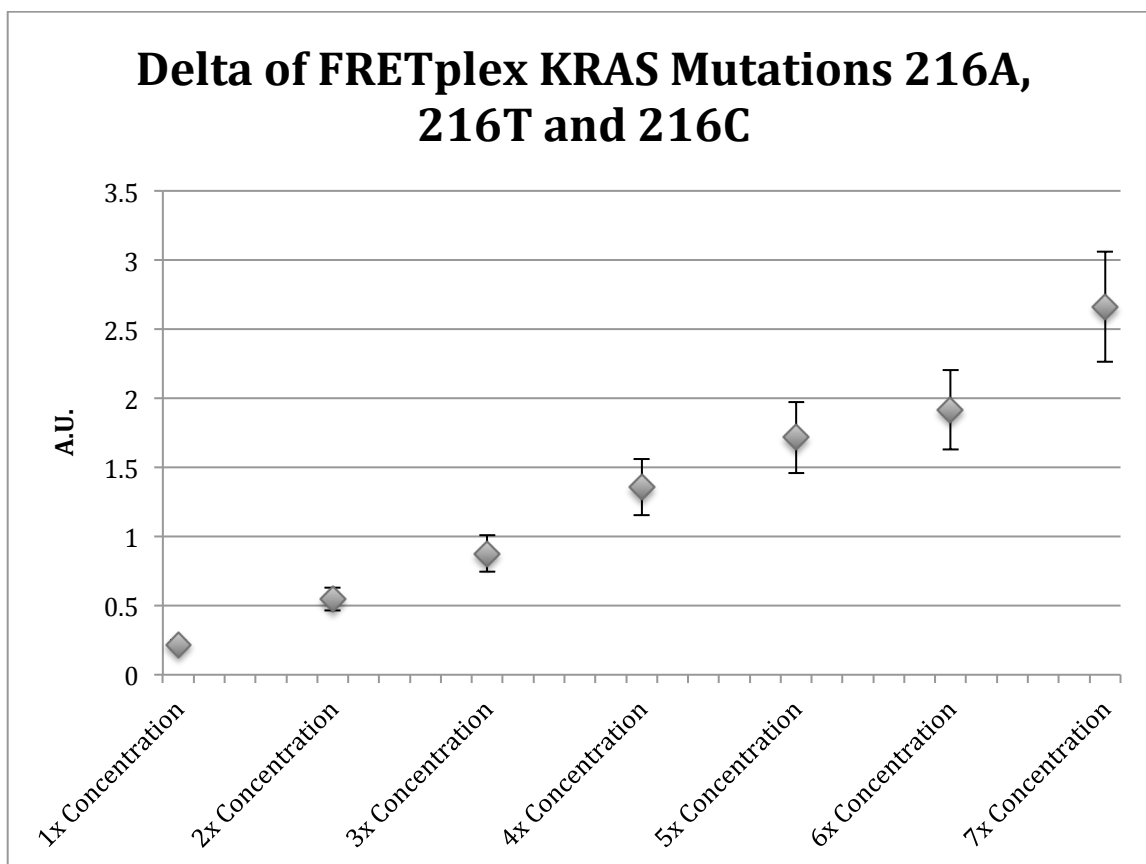


Figure 6.25. FRETplex emission intensities (delta values) obtained from FIGs. 6.19-6.24. Plotted as a function of the accumulated primer concentration ratio (x-axis) with a standard deviation of 1σ .

Unfortunately, the data present in figure 6.25 reveals that multiplexing beyond two mutations in a single reaction is a problem for this specific K-RAS assay, but would more than likely not be a problem for sequence that does not have a high amount of sequence similarity, but what about the systems sensitivity? Does the FRETplex system have a high degree of sensitivity? Using 8uL each of 216A, T, and C forward and reverse primers (table 6.20), I spiked different concentration of wild type sequence to try and generate a false signal. The assay needs the mutation present in order to amplify the DNA, yet the system is not perfect, as mistakes happen and DNA will get amplified even if it is not the correct target. In Figure 6.26, the FRETplex system dose very well and limits the number of false positives generated, and only then does the wild type

concentration reach 100,000uM and the signal reaches half of the signal we observed in the 1x concentration displayed in Figure 6.19. This is a nice result for a cancer diagnostic assay, since mutation can be quite rare and if the system cannot distinguish between a low mutant concentrations to a high wild type concentrations it would be useless, yet having a assay with a high sensitivity can be beneficial in its own right.

Components	Concentration
Reagents	20uL of Taq 5x mastermix
Wild Type Sequence	10uL of 10uM, 100uM, 1000uM 10,000uM or 100,000uM
216T Primers	8uL of 10uM
216A Primers	8uL of 10uM
216C Primers	8uL of 10uM

Table 20. FRETplexing Experiment Cocktail for Control Experiments Using Wild Type Sequences.

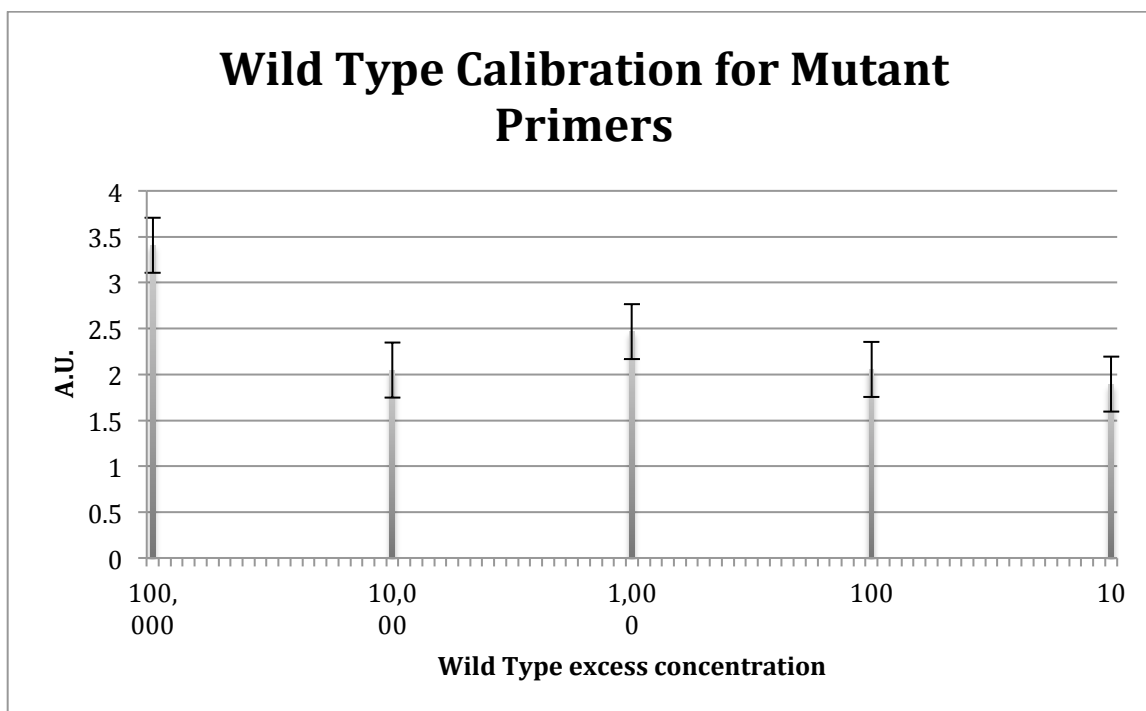


Figure 6.26. Wild Type Concentration Calibration Experiments Using FRET-Chromophore-Labeled Primers with qPCR. Each multiplexed assay contains 20uL of Taq 5x mastermix, 8 uL of 10uM for each primer 216C, 216A, and 216T, and the WT sequence at different volumes (10uL, 100uL, 1000uL, 10,000uL, and 100,000uL). The y-axis shows averaged relative FRET emission intensities obtained from 22 qPCR replica experiments. For each qPCR experiment, the relative FRET emission intensity (delta value) is calculated by subtracting the maximum FRET emission intensity with the minimum FRET emission intensity.

Using the same experiment design from Table 6.20, I added 2uL of 216C, 216T, or 216A individually, and this will generate a simple test to determine if a mutation is present or not. The resulting experimental data is graphed in Figure 6.27. From the graph we can observe that the mutation fluorescent signal is higher than just the wild type alone. This information can be used to develop a simple yes/no assay to determine if any K-RAS mutation is present. This information would be very useful during a surgery where the surgeon only cares if a tissue is carcinogenic and not what specific mutations are causing the cancer.

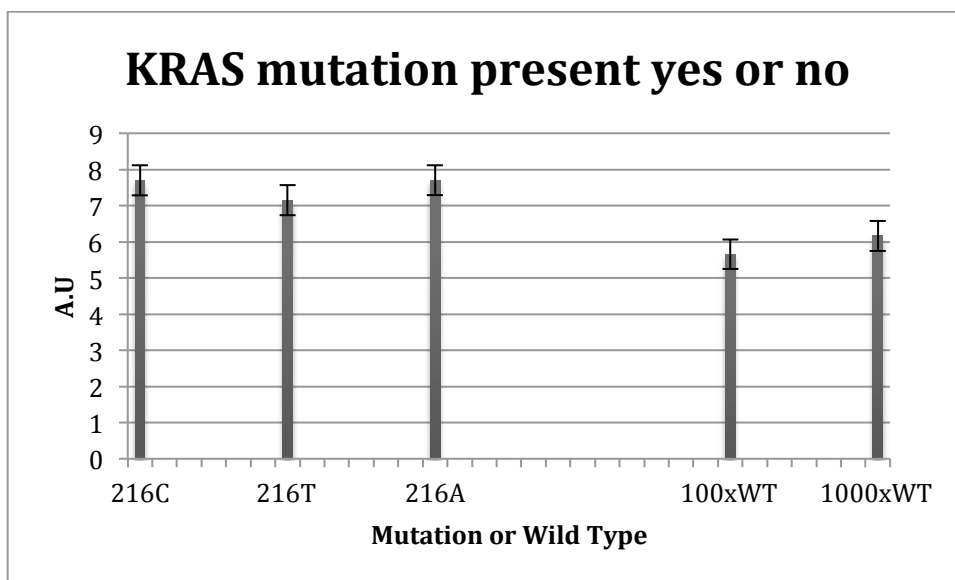


Figure 6.27. KRAS Yes No Diagnostic Assay. Chart reporting the detection of the presence or absence of a KRAS mutation 216A, 216T, and 216C using FRETplexing with qPCR. Each multiplexed assay contains 20uL of Taq 5x mastermix, 10uL of 10uM for a given mutant sequence, and 8uL of 10uM primer concentration for each of three primer pairs. The forward primer is labeled with Cy3 as a FRET donor chromophore and the reverse primer is labeled with Cy5 as a FRET acceptor chromophore. The chart shows averaged relative FRET emission intensities (delta values at y-axis) of 12 qPCR replica experiments plotted for each mutation also in comparison with wild type assay at two different concentrations: 10uL of 100uM wild type in one experiment and 10uL of 1000uM wild type in the other experiment.

Conclusion

Personalized medicine is the future of the medical industry, but this will come at a significant increase in diagnostic cost. The specific knowledge of an individual's genetic makeup can determine if a specific drug will be beneficial in that person's treatment. In the specific case of cancer, it was shown that colorectal cancer patients will have different success rates on different drugs, depending on what specific mutations they have in the KRAS gene.⁹⁸⁻¹⁰⁰ Yet unless you have familial genetic history for a specific cancer, and will have a unique set of mutations that caused that cancer to develop. There is a need to obtain genetic data for every person undergoing treatment, and unfortunately this will apply increased pressure on already limited resources and increase the initial cost of treatment, so there is a great need for cheaper and faster diagnostics.

Quenchi-plexing and FRET-plexing are both potential solutions to this problem of faster and cheaper diagnostics. Both technologies are advantageous, and since both generate genetic data during PCR amplification of the material, a step normally needed when doing genetic analysis; they also have the potential of eliminating the sequencing or gel step needed for mutation identification. This will have a two-fold impact. The first is reducing the cost of diagnostics, since only a few tests and reagents need to be used with decreases in the amount of labor required for performing the diagnostic test. The second impact occurs by decreasing the time between obtaining the sample and generating an answer. With the technology described in this thesis, PCR can now be accomplished in a matter of minutes, significantly reducing diagnostic time.

In an age of rising medical costs, innovations are needed to combat these increases. Quenchi-plexing and FRET-plexing can accomplish this by increasing the diagnostic capabilities of instruments we already use and provide more information than what would be traditionally obtained. Although they are limited in ability, the small improvement in time and cost can have a significant impact. Using a surgical example, it is possible to do diagnostic tests on tissue during surgery with these two methods. This could allow the surgeon to more accurately remove cancerous tissue, potentially preventing another surgery, which would be a significant improvement in care.

Chapter 7

Summation

There is a significant need to generate new diagnostic medical devices to advance and improve our understanding of biological concepts, but to devise new methods and techniques to advance medical diagnostics into the realm of gene therapy and personalized medicine. There is a problem with growing medical costs coupled with cost effective therapy that requires medical facilities increase the efficiency and effectiveness of therapeutic modalities. Microfluidics was developed to help develop expensive laboratory equipment towards cheap low cost devices that could be implemented at the point of care. This thesis displays the potential to incorporate the technologies of diverse educational disciplines (chemistry, physics, engineering, and material science) in order to solve complex biological problems and applications.

Referances

- 1 Hevehan, D.L. et al. *Biotechnology and Bioengineering* **1997**, 54, 221-230.
- 2 Unger, M.A. et al. *Science* **2000**, 288, 113-166.
- 3 Nyholm, L. *Analyst*. **2005**, 130, 599-605.
- 4 Wetley, J.R.; Wicks, C.E.; Wilson, R.E.; Rorrer, G. *Fundamentals of Momentum, Heat and Mass Transfer* **2001**, 4, 151-152.
- 5 Liu, R.H.; Yang, J.; Lenigk, R.; Bonanno, J; Grodzinski, P. *Anal. Chem.* **2004**, 76, 1824-1831.
- 6 Beebe, D.J.; Mensing, G.A.; Walker, G.M. *Annu. Review of Biomed Eng.* **2004**, 4, 261-286.
- 7 Beebe, D.J.; Wheeler, M.; Zeringue, H.; Walters, E.; Raty, S. *Theriogenology* **2002**, 57, 125-135.
- 8 Whitesides, G.M.; Rogers, J.A.; Meier, M.; Dodabalapur, A. *Appl. Opt.* **1999**, 38, 5799-5802.
- 9 Deng, T.; Tien, J.; Xu, B.; Whitesides, G.M. *Langmuir* **1999**, 15, 6575-6581.
- 10 Schuecker, O.J.A.; Brittain, S.T.; Whitesides, G.M. *Sensors and Actuators*. **1999**, 72, 125-139.
- 11 Beebe, D.J.; Atencia, J. *Nature* **2005**, 437, 648-655.
- 12 Becker, H.; Locascio, L. *Talanta* **2002**, 56, 267-287.
- 13 Khoury, C.; Mensing, G.A.; Beebe, D.J. *Lab Chip* **2002**, 2, 50-55.
- 14 Duffy, D.C.; McDonald, J.C.; Schueller, O.J.A.; Whitesides, G.M. *Anal. Chem.* **1998**, 70, 4974-4984.
- 15 Calvert, P. *Chem Master* **2001**, 13, 3299-3305.

- 16 Unger, M.A.; Chou, H.; Thorsen, T.; Schere, A.; Quake, S.R. *Science* **2000**, 288, 113-116.
- 17 Melin, J.; Quake, S.R. *Annu. Rev. Biophys. Biomol. Struct.* **2007**, 36, 213-231.
- 18 Jeon, N.L.; et al. *Langmuir* **2000**, 16, 8311-8316.
- 19 Wu, H.; et al. *J. Am. Chem. Soc.* **2001**, 122, 12691-12699.
- 20 Lichtman, J.W.; Conchello, J.A. *Nature Reviews* **2005**, 2, 910-919.
- 21 Yager, P.; et al. *Nature* **2006**, 442, 412-418.
- 22 Janasek, D.; Franzke, J.; anz, A. *Nature* **2006**, 422, 374-380.
- 23 El-Ali, J.; Sorger, P.K.; Jensen, K.F. *Nature* **2006**, 442, 403-411.
- 24 Unger, M.A.; et al. *Science* **2000**, 287, 113-116.
- 25 www.rsc.org/Publishing/Journals/Ic/index.asp (accessed September 15, 2008).
- 26 www.askoki.co.uk (accessed March 15, 2008).
- 27 Bayburt, T.H.; Sligar, S.G. *Protein Science* **2003**, 12, 2476.
- 28 Shaw, A.W.; McLean, M. A.; Sligar, S.G. *FEBS Lett.* **2004**, 556, 260
- 29 Civjan, N.R.; Bayburt, T.H.; Schuler, M.A.; Sligar, S.G. *BioTechniques* **2003**, 35, 556.
- 30 Pata, V.; Dan, N. *Biophys. J.* **2003**, 85, 2111.
- 31 Lazar, I. M.; Ramsey, R. S.; Ramsey, J. M. *Anal. Chem.* **2001**, 73, 1733.
- 32 Fintschenko, Y.; Choi, W.-Y.; Ngola, S. M.; Shepodd, T. J. *Anal. Chem.* **2001**, 73, 849.
- 33 MacDonald, M. P.; Spalding, G. C.; Dholakia, K. *Nature* **2003**, 426, 421.
- 34 Herr, A.E.; Molho, J.I.; Drouvalakis, K.A.; Mikkelsen, J.C.; Utz, P.J.; Santiago, J.G.; Kenny, T.W. *Anal. Chem.* **2003**, 75, 1180.

- 35 Seong, G. H.; Heo, J.; Crooks, R. M. *Anal. Chem.* **2003**, 75, 3161.
- 36 Mao, H. B.; Yang, T. L.; Cremer, P. S. *J. Am. Chem. Soc.* **2002**, 124, 4432.
- 37 Hadd, A. G.; Jacobson, S. C.; Ramsey, J. M. *Anal. Chem.* **1999**, 71, 5206.
- 38 Leach, A. M.; Wheeler, A. R.; Zare, R. N. *Anal. Chem.* **2003**, 75, 967.
- 39 Chiem, N. H.; Harrison, D. *J. Clin. Chem.* **1998**, 44, 591.
- 40 Bromberg, A.; Mathies, R. *Anal. Chem.* **2003**, 75, 1188.
- 41 Wang, J.; Ibanez, A.; Chatrathi, M. P. *Electrophoresis* **2002**, 23, 3744.
- 42 Lagally, E. T.; Mednitz, I.; Mathies, R. A. *Anal. Chem.* **2001**, 73, 565.
- 43 Khandurina, J.; McKnight, T. E.; Jacobson, S. C.; Waters, L. C.; Foote, R. S.; Ramsey, J. M. *Anal. Chem.* **2000**, 72, 2995.
- 44 Kopp, M. T.; deMello, A. J.; Manz, A. *Science* **1998**, 280, 1046.
- 45 Dan, N.; Pincus, P.; Safran, S. A. *Langmuir* **1993**, 9, 2768.
- 46 Bayburt, T. H.; Sligar, S. G. *PNAS*. **2002**, 99, 6725-6730.
- 47 Sligar, S.G. *Biochemical and Biophysical Research Communications* **2003**, 312, 115-119.
- 48 Denisov, I. G.; Grinkova, Y.V.; Lazarides, A. A.; Sligar, S. G. *J. Am. Chem. Soc.* **2004**, 126, 3477-3487.
- 49 Chen, F. Y.; Lee, M. T.; Huang, H. W. *Biophys. J.* **2002**, 82, 908-914
- 50 Meier, P. J.; Sztul, E. S.; Reuben, A.; Boyer, J. L. *The Journal of Cell Biology* **1984**, 98, 991-1000.
- 51 Bayburt, T.H.; Grinkova, Y.V.; Sligar, S.G. *Nano Lett.* **2002**, 2, 853-856.
- 52 Shih, A. Y.; et al. *Biophysical Journal* **2005**, 88, 548-556.
- 53 Giometti, C.S. et al. *Proteomics* **2003**, 3, 777-785.

- 54 Girgenti, A.J.; Szakacs, J.E. *Ann. Clin. Lab. Sci.* **2003**, 33, 123-124.
- 55 Ghindilis, A.L.; Atanasov, P.; Wilkins, M.; Wilkins, E. *Biosensors & Bioelectron.* **1998**, 13, 113-131.
- 56 Chu, X.; Lin, Z.N.; Shen, G.L.; Yu, R.Q. *M. Analyst.* **1995**, 120, 2829-2832.
- 57 Pless, P.; Futschik, K.; Schopf, E. *J. Food Prot.* **1994**, 57, 369-376.
- 58 Boisdé, G.; Harmer, A. *Chemical and Biological Sensing with Optical Fibers and Waveguides*, Artech House: Boston, **1996**.
- 59 Byfield, M.P.; Abuknesha, R.A. *Biosensor & Bioelectron.* **1994**, 9, 373-400.
- 60 Parikha, C.R.; et al. *Am. Jour. Transplantation* **2006**, 1639-1645.
- 61 Yamauchi, J.; Akimoto, Y.; Nibe, M.; Nakano, H. *IEEE Photonics Tech. Lett.* **1996**, 8, 236-238.
- 62 Wijesuriya, D.; Breslin, G.; Anderson, G.; Shriver-Lake, L.; Ligler, F.S. *Biosensor & Bioelectron* **1994**, 9, 585-592.
- 63 Tedeschi, L.; Domenici, C.; Ahluwalia, A.; Baldini, F.; Mencaglia, A. *Biosensors & Bioelectron* **2003**, 19, 85-93.
- 64 DeLisa, M.P.; Zhang, Z.; Shiloach, M.; Pilavar, S.; Davis, C.C.; Sirkis, J.S.; Bentley, W.E. *Ana Chem.* **2000**, 72, 2895-2900.
- 65 Claudon, P.; Donner, M.; Stoltz, J.F. *Journal of Mat Science: Materials in Medicine* **1991**, 2, 197-201.
- 66 Fekete, Z.; Pongracz, A.; Furjes, P.; Battistig, G. *Microsyst Technol.* **2012**, 18:353-358.
- 67 Edell, D. J.; Toi, V. V.; McNeil, V. M.; Clark, L. D. *IEEE Transaction on Biomedical Engineering* **1992** 39, 635-643.

- 68 Suehiro, J.; Pethig, R. *J. Phys. D: Appl. Phys.* **1998** 31, 3298-3305.
- 69 Wnag, X.; Huang, Y.; Gascoyne, P. R. C.; Becker, F. F. *IEEE Transaction on Industry Application* **1997** 33, 660-670.
- 70 Kai, G.; WeiHua, P.; XiaoQian, L.; Qiang, G.; RongYu, T.; Jian, L.; HongDa, C. *Technological Sciences* **2012** 55, 1-5.
- 71 Cheung, K. C.; Djupsund, K.; Dan, Y.; Lee, L. P. *Journal of Micoelectromechanical Systems* **2003** 12, 179-185.
- 72 King C.R.' Kraus MH, Aaronson SA, King CR, Kraus MH, *Science*. **1985**;229:974-976.
- 73 Slamon DJ, Clark GM, Wong SG, et al. *Science*. **1987**;235:177-182
- 74 Romond EH, Perez EA, Bryant J, et al. *New England Journal of Medicine*. **2005**;353:1673-1684.
- 75 Smith I, Procter M, Gelber RD, et al. *Lancet*. **2007**;369:29-36.
- 76 Mittendorf EA, Wu Y, Scaltriti M, et al. *Clinical Cancer Research*. **2009**;15:7381-7388.
- 77 Meng S, Tripathy D, Shete S, et al. *Proceedings of the National Academy of Sciences of the United States of America*. **2004**;101:9393-9398.
- 78 Cristofanilli M, Budd GT, Ellis MJ, et al. *New England Journal of Medicine*. **2004**;351:781-791.
- 79 Gilbey AM, Burnett D, Coleman RE, et al. *Journal of Clinical Pathology*. **2004**;57:903-911.
- 80 Allard WJ, Matera J, Miller MC, et al. *Clinical Cancer Research*. **2004**;10:6897-6904.

- 81 Nagrath S, Sequist LV, Maheswaran S, et al. *Nature*. **2007**;450:1235- 1239.
- 82 Maheswaran S, Haber DA, Maheswaran S, Haber DA. *Current Opinion in Genetics & Development*. **2010**;20:96-99.
- 83 Zheng S, Lin H, Liu JQ, et al. *Journal of Chromatography A*. **2007**;1162:154-161.
- 84 He W, Wang H, Hartmann LC, et al. *Proceedings of the National Academy of Sciences of the United States of America*. **2007**;104:11760-11765.
- 85 Danila DC, Heller G, Gignac GA, et al. *Clinical Cancer Research*. **2007**;13:7053-7058.
- 86 . Xu X, Zhong JF, Xu X, Zhong JF. *Journal of Investigative Dermatology*. **2010**;130:2349-2351.
- 87 Nelson NJ, Nelson NJ. *Journal of the National Cancer Institute*. **2010**;102:146-148.
- 88 Maheswaran S, Sequist LV, Nagrath S, et al. *New England Journal of Medicine*. **2008**;359:366-377.
- 89 Mohamed, H, Murray, M, Turner, J.N, et al. *Journal of Chromatography A*. **2009**;1216:8289-8295.
- 90 Stott, S.L, Hsu, C.H, Tsukrov D.I, et al. *Proceedings of the National Academy of Sciences of the United States of America*. **2010**;107:18392-18397.
- 91 Tan, S.J, Yobas, L, Lee, G.Y, et al. *Biomedical Microdevices*. **2009**;11:883- 892.
- 92 Zhong, J.F, Chen, Y, Marcus, J.S, et al. *Lab on a Chip*. **2008**;8:68-74.
- 93 Allan, A.L, Vantuyghem, S.A, Tuck, A.B, et al. *Cytometry Part A: The Journal of the International Society for Analytical Cytology*. **2005**;65:4-14.
- 94 Cruz, I, Ciudad, J, Cruz, J.J, et al.. *American Journal of Clinical Pathology*. **2005**;123:66-74.

- 95 Simpson, S.J, Vachula, M, Kennedy, M.J, et al. *Experimental Hematology*.**1995**; 23:1062-1068.
- 96 Rajagopal, A Scherer, A., Homyk, A., Kartalov, E.P. *Anal.Chem.*, **2013** 85 (16), 7629-7636.
- 97 E. Kartalov, D. Shibata, C. Taylor, L. Wade (2011) “Methods and Devices for Micro- Isolation, Extraction, and/or Analysis of Microscale Components”, USPTO Application #13/010761, Pub # US 2011/0177518 A1.
- 98 A. Lievre et al. *Cancer Research*, **2006** 66(8), 3992–3995.
- 99 Bokemeyer C et al. *J. Clin. Oncol.* **2009** 27 (5): 663–71.
- 100 Van Cutsem E et al. *N. Engl. J. Med.* **2009** 360 (14): 1408–17.
- 101 Samowitz WS, Curtin K, Schaffer D, Robertson M, Leppert M, et al. *Cancer Epidemiol Biomarkers Prev* **2000** 9: 1193–7.
- 102 J. Morlan, J. Baker, D. Sinicropi *PLoS ONE*, **2009** 4(2), e4584.
- 103 Speicher, M. R.; Ballard, S. G.; Ward, D. C. *Nature Genetics* **1996**, 12, 368-376.
- 104 Huang, Q.; Hu, Q.; Li, Q. *Clinical Chemistry* **2007**, 53(10), 1741-8.
- 105 Huang, Q.; Zheng, L.; Zhu, Y.; Zhang, J.; Wen, H.; Huang, J.; Niu, J., et al. *PloS one* **2011**, 6(1), e16033.
- 106 J. Zebala “Instrumentation and Method for Maskless Photolithography.” USPTO Application # 12/325,126 (published 2010). Pub. #: US 2010/0020299 A1.
- 107 M. Armani, J. Rodriguez-Canales, J. Gillespie, M. Tangrea, H. Erickson, M. R. Emmert- Buck, B. Shapiro, and E. Smela *Lab Chip*, **2009** 9(24), 3526 - 3534.
- 108 Lin, D.H., Taylor, C.R., Anderson, W.F., Scherer, A., Kartalov, E.P. *J Chromatogr B*, **2009** 878, 258-263.

- 109 Kartalov, E.P., Lin, D.H., Lee, D.T., Anderson, W.F., Taylor, C.R., and Scherer, A.
Electrophoresis, **2008** 29, 5010- 5016.
- 110 Kartalov, E.P., Zhong, J., Scherer, A., Quake, S., Taylor, C. and Anderson, W. F.
BioTechniques **2006** 40:1, 85-90.
- 111 Kartalov, E.P. and Quake, S. *Nucleic Acids Research* **2004** 32: 2873-2879.
Braslavsky, I., Hebert, B.,
- 112 Kartalov, E. and Quake, S.R. *Proc. Nat'l Acad. Sci. USA* **2003** 100: 3960-3964.
- 113 Chiu, C.-S., Kartalov, E., Unger, M., Quake, S., and Lester, H. *J of Neurosci Meth*
2001 185:55-63.